Dr. Mercante 420

UCRL-50572

THE LRL ELECTRON AND PROTON SPECTROMETER ON NASA'S ORBITING GEOPHYSICAL OBSERVATORY V(E) (INSTRUMENTATION AND CALIBRATION)

H. I. West, Jr.
J. H. Wujeck
J. H. Mc Quaid
N. C. Jensen
R. G. D'Arcy, Jr.
R. W. Hill
R. M. Bogdanowicz

June 2, 1969

Lawrence Radiation Laboratory
UNIVERSITY OF CALIFORNIA
LIVERMORE

Lawrence Radiation Laboratory
UNIVERSITY OF CALIFORNIA
LIVERMORE

UCRL-50572

THE LRL ELECTRON AND PROTON SPECTROMETER ON NASA'S ORBITING GEOPHYSICAL OBSERVATORY V(E) (INSTRUMENTATION AND CALIBRATION)

H.I. West, Jr.
J.H. Wujeck
J.H. Mc Quaid
N.C. Jensen
R.G. D'Arcy, Jr.
R.W. Hill
R.M. Bogdanowicz

Contract No: NASA P.O. No. S-70014-G.

Contents

List of Illustrations

List of Tables

THE LRL ELECTRON AND PROTON SPECTROMETER ON NASA'S ORBITING GEOPHYSICAL OBSERVATORY V(E) (INSTRUMENTATION AND CALIBRATION)

Abstract

The design, construction, and calibration of the LRL electron and proton experiment on the OGO-V satellite are described. A brief account of post-launch results is included. The electron spectrometer consists of two small permanent magnets used for energy analysis with electron detection provided by solid-state detectors. Background detectors are also provided. The energy range covered is approximately 60 to 2950 keV in 7 differential energy channels. Geometrical factors vary from 0.18 to 8.6 cm^2-keV-sr.

The proton spectrometer consists of a single solid-state detector and a range-energy telescope of four solid-state detectors situated in line with the entrance aperture of the larger of the electron spectrometer magnets. The energy range is 0.1 to 94 MeV in 7 differential energy channels. The geometrical factor for the lowest energy channel (0.1 to 0.15 MeV) is 2.06×10^{-3} cm^2-sr and for the rest of the proton channels 1.3 to 1.9×10^{-2} cm^2-sr. Data handling in the experiment is primarily digital using a binary floating-point compressional scheme. The experiment apertures are scanned relative to the stabilized spacecraft for obtaining pitch-angle distributions.

1. Introduction

1.1 SCOPE AND DESCRIPTION

This report describes an electron and proton spectrometer in use aboard NASA's OGO-V(E) satellite. (The instrument was developed and built under NASA Order No. S-70014-G.) The electron sensor consists of two permanent magnet electron spectrometers (Figs. 1-1 and 1-2). Buried inside the larger of the two magnets in line with the entrance aperture is a proton telescope. A small detector adjacent to the telescope provides a low-energy proton channel. The instrument is designed to measure the spectra, fluxes, and directional properties of electrons, protons, and alpha particles. Table 1-1 lists the information channels provided. The measurement of the direction of the charged particles is obtained by scanning the entrance apertures of the spectrometers relative to the spacecraft.

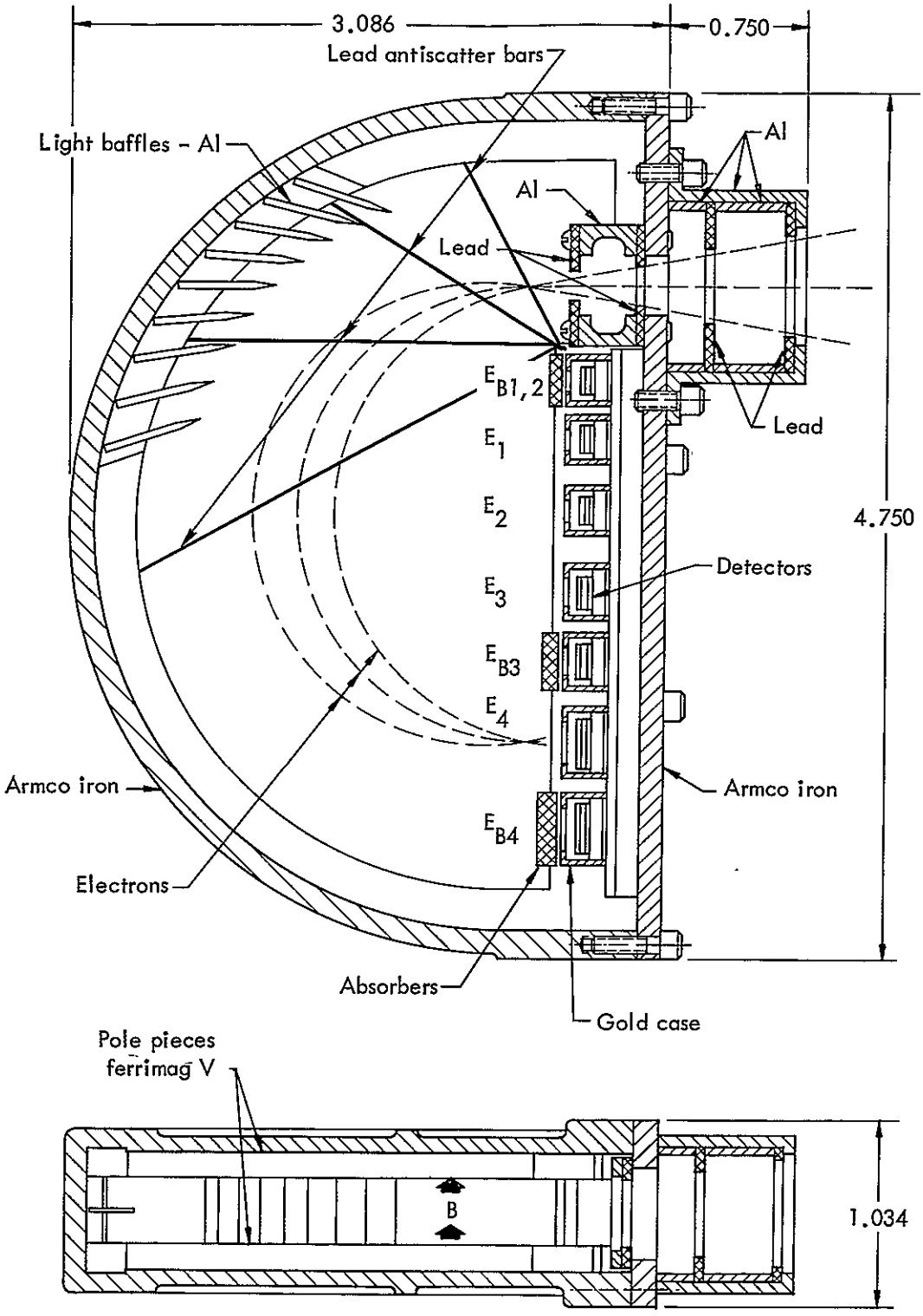

Fig. 1-1. Low-field electron spectrometer.

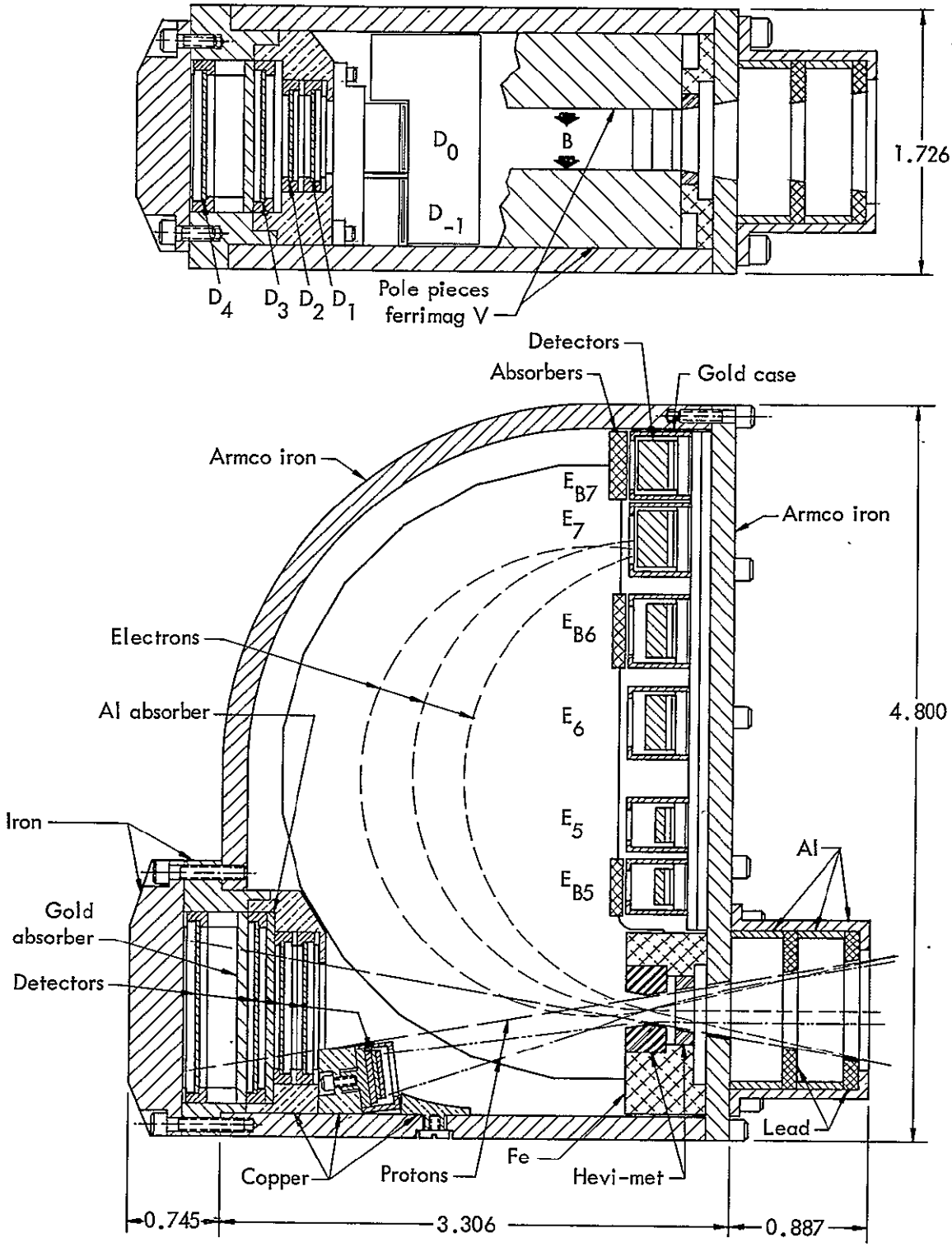

Fig. 1-2. High-field electron spectrometer and proton detection system.

Table 1-1. Characteristics of detection system.

Particles	Instrument	Energy	Symbol designating measurement
Electrons	Magnetic electron spectrometer	79 ± 23 keV	E_1
		158 ± 27	E_2
		266 ± 36	E_3
		479 ± 52	E_4
		822 ± 185	E_5
		1530 ± 260	E_6
		2820 ± 270	E_7
	Proton telescope	> ~4 MeV	E_8
Protons	Single detector	0.10 to 0.15 MeV	P_1
	Proton telescope	0.23 to 0.57	P_2
		0.57 to 1.35	P_3
		1.35 to 5.40	P_4
		5.60 to 13.3	P_5
		14.0 to 46	P_6
		43 to ~94	P_7
Alpha	Proton telescope	5.9 to 21.6	α_1
		22.7 to 55.2	α_2
		56.4 to 104	α_3
Omnidirectional measurement of bremsstrahlung and penetrating protons	Shielded solid-state detector, bremsstrahlung threshold 300 keV, and proton threshold ~80 MeV	Pulses > 0.30 MeV	O_1
Omnidirectional measurement of penetrating protons		Pulses > 7.20 MeV equivalent to protons > ~80 MeV	O_2

1.2 SCIENTIFIC CONSIDERATIONS

At 13:06:01.5 GMT of March 4, 1968 the OGO-V satellite was launched into an orbit with an inclination of 31.265°, an apogee of 146,757 km, and a perigee of 291 km. The orbital period was 62 hr 26.3 min. During the first year of operation, apogee has been on both the day and night side of the earth. Also, by virtue of its delayed launch, its operation is covering the peak of the solar cycle. OGO-V contains many highly sophisticated experiments designed to measure particles from plasma to cosmic energies and to provide measurements of magnetic fields and low frequency waves.

This experiment, designated E-06, was designed to take over where the low energy charged particle experiments stop (a few tens of keV) and to extend the range to several MeV.

Because of the satellite orbit, wide ranges in flux are encountered. Consistent with the constraints inherent in the instrument design, as wide a dynamic range of operation as possible has been provided. The instruments are designed to function in the heart of the radiation belts and still have enough sensitivity and adequate background rejection to obtain useful data in the region outside the geomagnetic cavity. In this latter respect, the onset of solar maxima has proved interesting.

The spectrometers have a moderately small acceptance angle. To properly use such instruments, the aperture of the instruments should be oscillated in a controlled manner in order to obtain the directional distributions of the measured radiations. This scan is provided by a special mechanism on OPEP-2. (See a diagram of the spacecraft in Fig. 1-3.) Scan in the neighborhood of the earth is about the earth's radius vector with the instrument's aperture looking perpendicular to this direction. This scan does not provide the complete angular coverage desired; however, a second scan perpendicular to this direction was considered overly complex for this mission. Pitch angle information comes from correlating the aperture scan direction with the magnetic field data obtained from the UCLA Fluxgate Magnetometer Experiment.

Broadly speaking, the objectives of the measurements are to obtain the energy, fluxes, and directional properties of the measured radiations along with their time history. Major emphasis is being given to the region inside the magnetosphere. Data from other experiments on OGO-V is available to provide many of the required correlations during data analysis.

1.3 TECHNICAL OUTLINE

This report documents the design details of the instrument and the calibrations. This includes the design of the sensors, electrical circuits associated with the sensors, data handling circuits, and the mechanical design. Three instruments have been built; the prototype, and first and second flight models. The prototype should be considered an advanced breadboard. Major design changes were made between it and the flight models. Flight units were essentially identical except for the usual variations in detector characteristics, spectrometer magnetic fields, and amplifier gains. This report is primarily the documentation of Flight Unit No. 1, the instrument in orbit on OGO-V.

The experiment consists of a sensor package located on OPEP-2 (- Z-axis) of the spacecraft (Fig. 1-3) which is connected to an electronics package located in the main body of the spacecraft. Data handling is digital, with considerable data sharing between the 20 scalers (accumulators) in the experiment and the 5 digital words available for reading the experiment data into telemetry. One analog word is used to provide experiment synchronization and to read out status data.

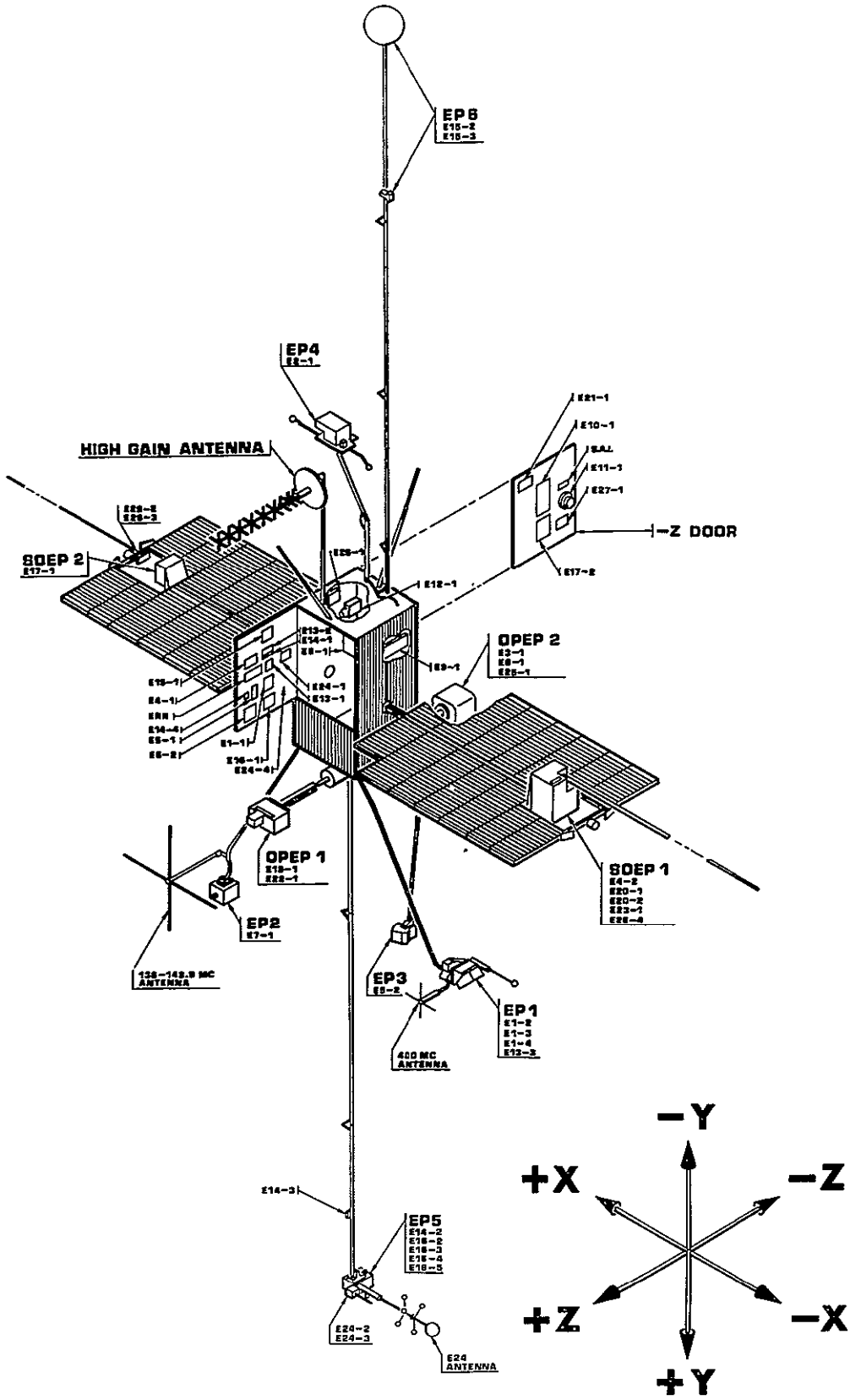

Fig. 1-3. OGO-V spacecraft showing experiment locations.

2. The Electron Spectrometer

2.1 INTRODUCTION

The problem is to uniquely determine the energy spectra and fluxes of electrons over a large dynamic range (that is in the range of flux changes of $<1/cm^2$-sec to $>10^8/cm^2$-sec) in the presence of proton fluxes varying over a similar range and over a wide range of energies. One is quickly led to the use of a magnetic broom to sweep away the protons from the detector. One might consider several detection systems. The detector could be a single scintillation detector which however, suffers from problems of long-term pulse-height stability, change in pulse height with counting rate and severe spectral distortion at high counting rates, and non-unique energy response. A single solid-state detector with pulse-height analyzers would have been effective over much of the orbit (>5 earth radii) but has the problem of spectral distortion due to pulse pile-up, non-unique energy response and lacks redundancy. We chose as our spectrometer[1] to use the principle of first-order semicircular focusing in a uniform magnetic field as had been in common use in beta ray spectroscopy. Solid state detectors in the focal plane are used to count the analyzed particles. Pulse height analysis is used to select only the full energy pulses, thus reducing the effects of bremsstrahlung and penetrating protons, and reducing the detection of degraded electrons that have scattered off the spectrometer walls. In order to clearly define the entrance aperture, a disk-loaded collimator is used at the entrance to the spectrometer.

One has the choice of using a single size detector for each energy channel in the spectrometer with a single shielded detector to determine background. In this case the detector functions much as a Geiger-Mueller counter except that there is a widely varying range of pulse heights. The window of the pulse height analyzers would have to be set wide to accept the pulses. A serious problem occurs for high energy particles at minimum ionization since it is almost impossible to discriminate against them. In the interest of background rejection, we chose the somewhat complex approach of providing tailored detectors for each energy channel plus a corresponding background detector. The detector depletion depths are approximately an electron range (for the upper channels) and only the pulses in the peak of the energy distribution of pulses are used.

Two magnetic spectrometers are provided: the high-field spectrometer and the low-field spectrometer. This choice was dictated by several reasons. It was essential to keep the high-field spectrometer small in order to maximize the geometrical factor of the proton telescope and to maximize the geometry for the detection of energetic electrons. Crowding low-energy electron channels into this magnet would result in poor energy resolution,

[1] For an account of work using a similar instrument see, H. I. West, L. G. Mann, and S. D. Bloom, in Space Research (Intern. Space Science Symp., 5th, Florence, 1964; North Holland, Amsterdam, 1965), vol. 5, p. 423. H. I. West, Radiation Trapped in the Earth's Field, B. M. McCormac, Ed. (D. Reidel, Dordrecht, Holland, 1965), p. 634.

poor angular resolution, and mechanically unfeasibly small detectors for the lower channels. Utilizing the second magnet also allows aligning the magnets for external dipole cancellation. Surprisingly, the use of two magnets is lighter than any of the single magnet configurations which came close to meeting requirements.

2.2 MAGNET DESIGN

The primary consideration for our purposes is to choose the permanent magnetic material with the highest magnetic energy per unit weight when producing the magnetic field required (2 to 4 kG). Our choice was the ferroceramic Ferrimag V (same as Indox V or Arnox V) with peak energy product B_dH_d of 3.2×10^6 G × Oe at a mass density of ~5 g/cm^3. The thickness of the magnetic material is dictated by the field required in the air gap and by the requirement that B_dH_d (refer to the manufacturer's demagnetization curve) be near a maximum. These considerations produced the lightest magnet possible and the highest geometrical factors. The return path of the magnets is of annealed Armco iron. Careful annealing is necessary to reduce the external stray field, since the flux in the return path is ~10 to 12 kG. In an effort to minimize the external field, where possible the return path has been welded into one continuous path to reduce the fringing field at air gaps.

The ferroceramics have the unfortunate property of being temperature sensitive. The change of field with temperature is -0.19%/°C. Below some critical temperature, depending upon where in the demagnetization curve the magnetic material is working, the material is irreversible and some flux will be lost in returning to a higher temperature. The high-field magnet (2690 G at 20°C) was designed to be reversible down to ~ -45°C without flux loss. The low-field magnet, however, was designed for an initial field of ~1500 G. Temperature cycling down to -45°C resulted in a room temperature field of 863 G (the design goal) after which it was stable to -45°C upon repetition of the temperature cycle. Both magnets were temperature cycled three times to insure reversibility.

2.3 MAGNETIC SHIELDING

To minimize the magnetic flux to be attenuated, the two magnets are aligned so that the external dipoles are in opposition (see Fig. 7-1). The resultant field has a maximum value at 1 ft of about 2000 γ. Originally, we had anticipated the need for a rather elaborate shield. It was found, however, that a shell of 4 mil Conetic* shielding material placed ~1/2 in. or greater (see Fig. 7-1), completely shields the field of the magnets. There is one precaution. The Conetic must be very carefully annealed and not "work hardened" afterwards. The residual field from the OPEP package at 12 in. was ~300 γ. After exposure to a 25-G field (a saturation field for the Conetic shield) the so called "permed" field was ~1400 γ. The package "depermed" (degaussed) to a field of ~120 γ. The perturbation to an ambient field of 25,000 γ was ~1300 γ. The above results were for Flight Unit 1 but were typical for both the prototype and Flight Unit 2.

*Product of the Magnetic Shield Division, Perfection Mica Company.

2.4 DETECTORS

Mechanically speaking, the choice of detectors for the spectrometer is the silicon solid-state detector. The choice of detector for the low energy channels is the diffused junction detector (D. J.) because of its greater resistance to radiation damage than the lithium drift detector (LiD).

Because of the thick depletion depths required, LiD detectors must be used for the higher energy channels. Fortunately the radiation damage sites in the detectors tend to "anneal out" during the long period of time OGO-V is outside the radiation belts, and hence radiation damage is not expected to be a serious problem. Radiation damage shows up as a loss in detector resolution and as an increase in leakage current. A marked increase in leakage current will cause a loss of detector bias due to the voltage drop in the bias resistor. The voltage drop can cause a degradation in the detector pulse rise time which can cause loss of pulse height and detection efficiency. For the detector used in channels 1 through 5, a factor of two reduction in detector bias is tolerable. For channels 6 and 7, effects show at approximately 30% and 20% reduction in bias respectively. There is also a similar problem with the proton detectors as detectors D_3 and D_4 are overbiased by only about 30%. The leakage of a solid-state detector doubles every 8 to 10°C; hence to minimize the leakage problem, the OPEP package is operated at 0 ± 10°C.

Unfortunately the detectors are not uniquely sensitive to electrons but will detect both bremsstrahlung (by Compton and photo-electric interactions) and penetrating protons. This was part of the reason for housing the detectors in cases of the high-density high-Z material, gold, as this allows a large amount of shielding close to the detectors. Also, the use of gold provides a defining slit in front of the detector and prevents sideways scattering of electrons between detectors. An important aspect of the gold case is the high elastic scattering cross section of gold for electrons, which results in the reflection back into the detector of many electrons which penetrate the detectors. This increases the proportion of high-energy pulses in the pulse height distribution and allows a higher threshold discrimination to be used for a given detector efficiency, thus reducing the bremsstrahlung detection ($\sim 1/E$ distribution of pulse height in the detectors in the hearts of the radiation belts). Typical response curves of the detectors to monoenergetic electrons are shown in Figs. 2-1, 2-2, and 2-3.

The depletion depth of the detectors used for the higher-energy channels is chosen to be approximately a range for the electron energies to be detected. This is of some importance for the LiD detectors as the lithium will continue to drift ($\sim 1/2$ mm per year at 20°C for fields of 100 V/mm) during the satellite mission, hence raising the sensitive volume of the detector. The thickness of the detectors for the two lowest energy channels is dictated by noise requirements. With the low noise (FET type) preamplifiers available, a depletion depth of $\sim 200\ \mu$ is a good compromise from the view point of low capacity and the problems inherent in making thicker D. J. detectors. Unfortunately, pulses from minimum ionizing protons will be detected in the lowest energy channel, but

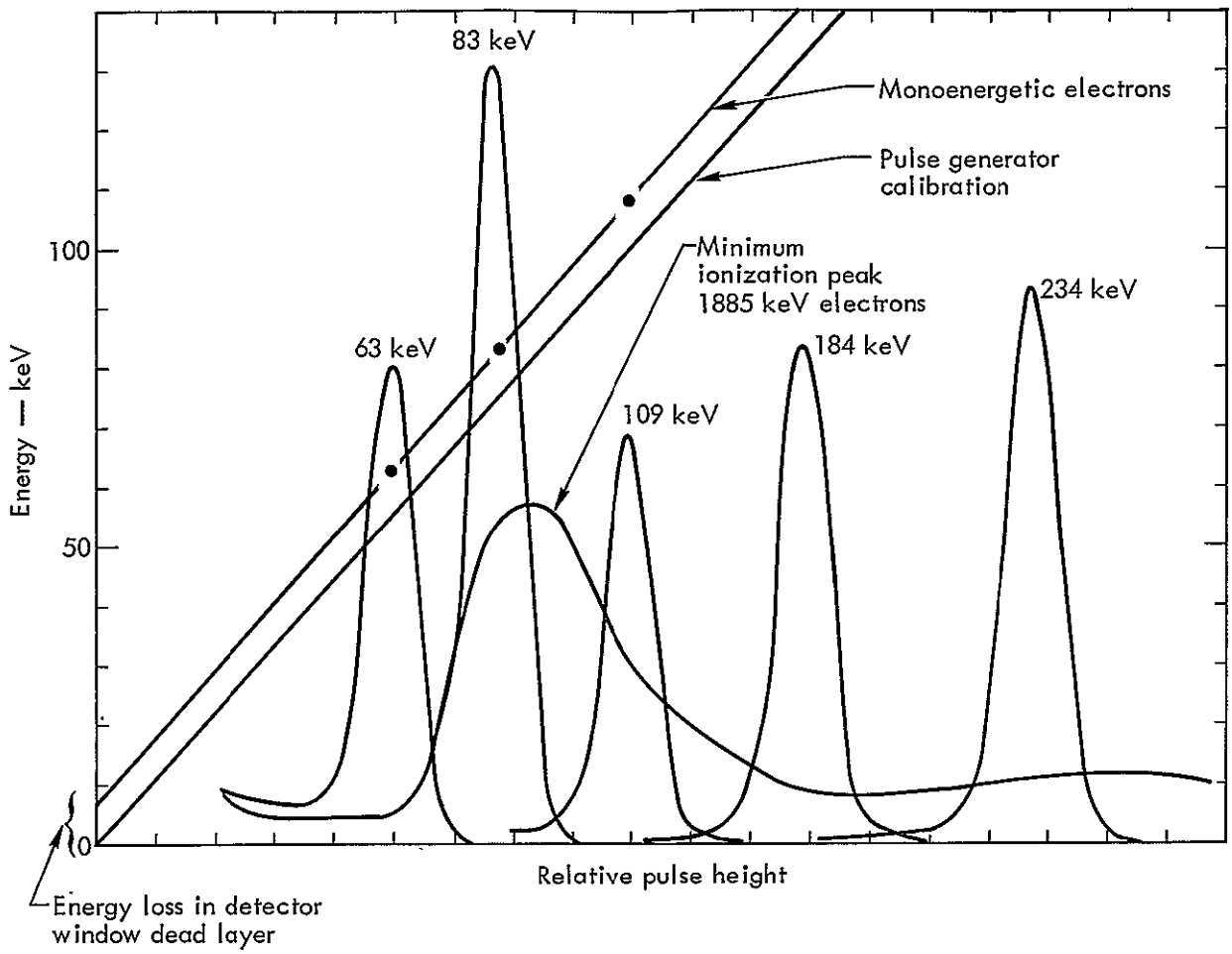

Fig. 2-1. Response of detectors used in channels E_1 and E_2 to monoenergetic electrons.

since the signal-to-background ratio is high (>50/1), this is not a problem. The characteristics of the detectors are shown in Table 2-1. The detectors were manufactured by the Solid State Radiations Inc., Los Angeles, California, under the direction of Dr. F. Ziemba.

2.5 PROPERTIES OF THE ENERGY CHANNELS

We are interested in the energy of the channel, the channel width, angular acceptance, and in its geometrical factor. For our purposes we express the geometrical factor in terms of the units A Ω ΔE. For computational convenience we may consider A as the effective area of the entrance aperture, Ω the solid angle with which a point in the aperture views the detector, and ΔE the effective energy bite. To complete the geometry we need the probability of detecting the electron once it has hit the detector which is in the range of 0.5 to 0.8. To a rather good first order (neglecting fringing fields and obliquity effects) we find

$$A\,\Omega\,\Delta E \cong \ell_a W_a \times \left(\frac{W_s}{b}\right)\left(\frac{\ell_d}{b + \pi\rho}\right) \times \left(\frac{W_d}{2\rho}\right)\left(\frac{2 + E/\mu}{1 + E/\mu}\right) E \quad \text{cm}^2 - \text{sr} - \text{keV}$$

where

ℓ_a = length of aperture
W_a = width of aperture
ℓ_d = length of detector
W_d = width of detector
W_s = width of slit
b = aperture to slit distance
E = electron energy in keV
μ = electron rest mass = 511 keV
ρ = radius of curvature of electrons path in the magnetic field.

This equation is given primarily for instructive value. The maximum range of energies detected is

$$\Delta E_{Base} = \left(\frac{W_s + W_d + \rho\phi^2}{2\rho}\right)\left(\frac{2 + E/\mu}{1 + E/\mu}\right)$$

where

$$\phi = \tan^{-1}\left(\frac{W_s + W_a}{2b}\right).$$

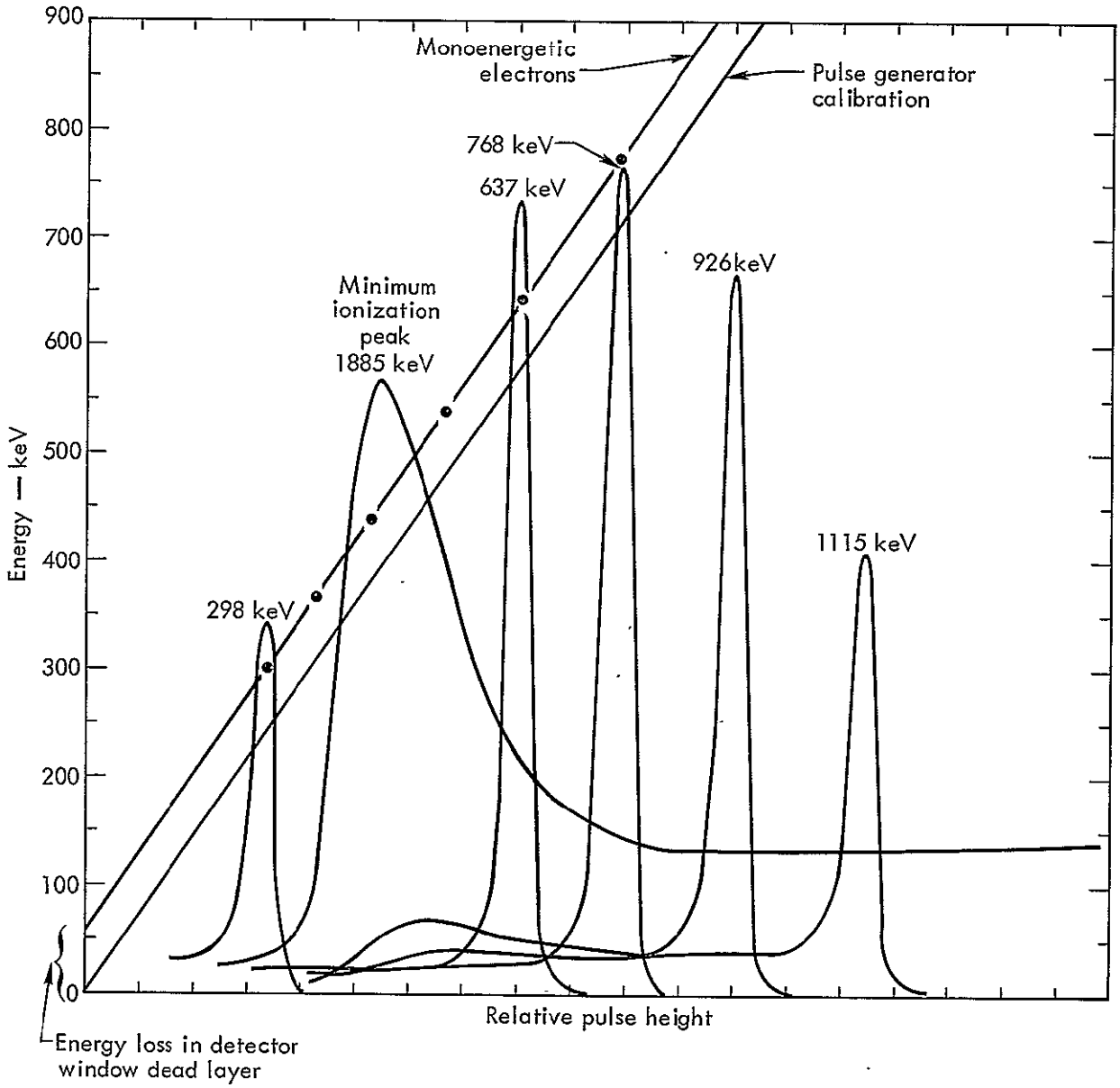

Fig. 2-2. Response of detector used in channel E_5 to monoenergetic electrons.

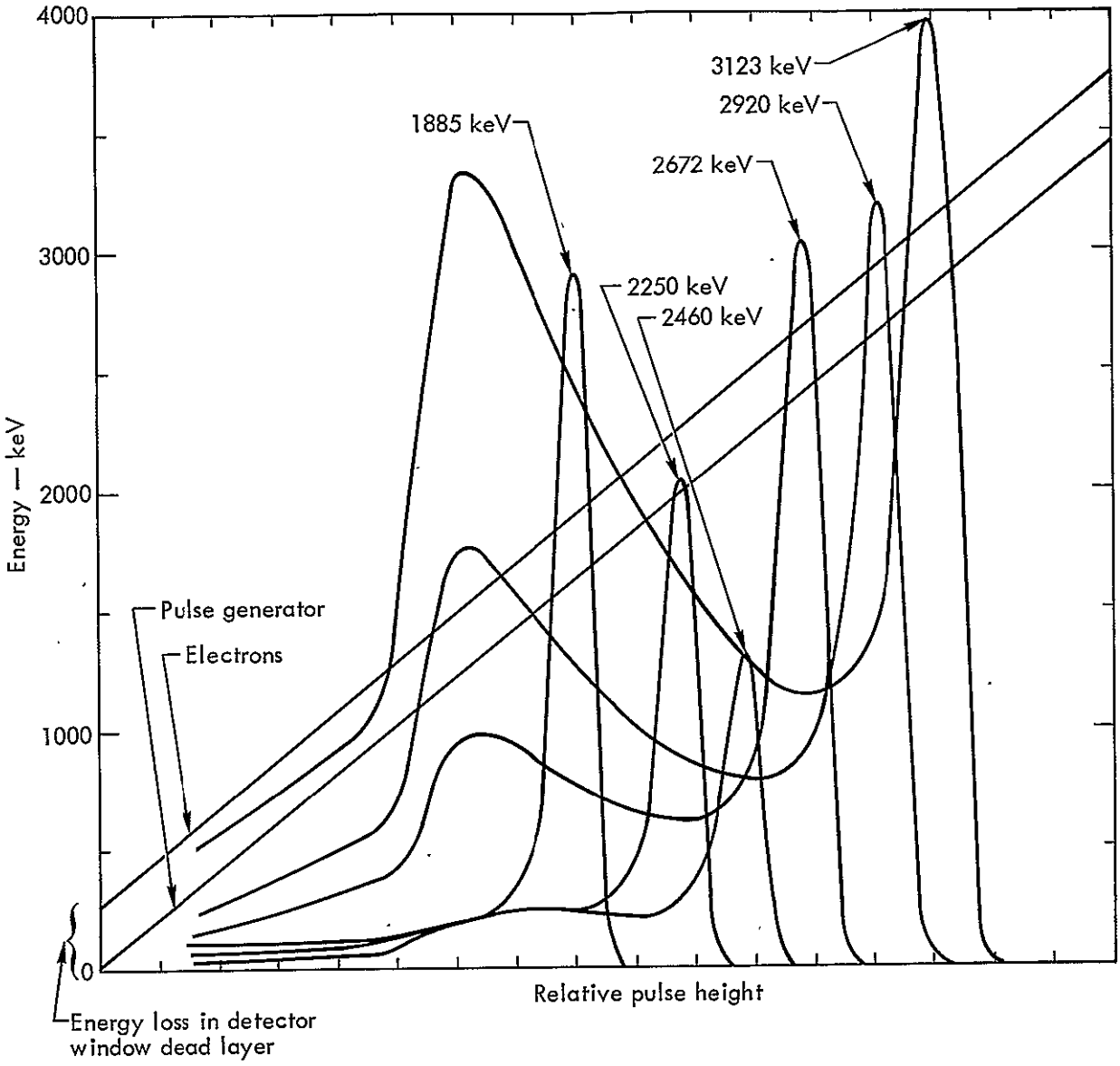

Fig. 2-3. Response of detector used in channel E_7 to monoenergetic electrons.

Note that ΔE in the geometry equation and ΔE_{Base} differ. The resolution, FWHM is ~ $\Delta E_{Base}/2$.

The energies of the channels were determined by calibrating solid-state detectors in a laboratory beta ray spectrometer and then using the detectors in the flight spectrometer focal planes. The geometrical factors were determined by first calibrating extended uniform sources of beta ray emitters. The sources were then placed over the spectrometer apertures to yield the geometrical factors directly. The results including temperature dependences are given in Table 2-2. The accuracy of the geometry calibrations is expected to be within ±10% for channels 2-7 and ±15% for channel 1. The relative error should be well within half these values.

Table 2-1. Characteristics of electron spectrometer detectrons.

	Channel No.	Detector type	Depletion depth	Bias[a] voltage (V)	Approximate[b] leakage current (μA)	Detector dimensions length × width (mm)	Detector slit dimensions length × width (mm)	Reflector[c] over slit	Detector encapsulation "paralene"
Low-field magnet									
	E_1	DJ	270 μ	-50	0.22	10 × 4	9 × 3	0.1 mil rubber hydrochloride	none.
	E_2	DJ	270 μ	-50	0.38	10 × 4	9 × 3	0.1 mil rubber hydrochloride	none
	B_{12}		270 μ		~0.1				
	E_3	DJ	246 μ	-100	~0.1	10 × 5	9 × 4	0.25 mil mylar	0.5-1.0 mil
	B_3		266 μ		~0.1				
	E_4	DJ	460 μ	-300	~0.1	10 × 7	9 × 6	0.25 mil mylar	1.0 mil
	B_4		490 μ		~0.1				
High-field magnet									
	E_5	LiD	1.45 mm	-150	1.4	10 × 6	9 × 5	0.5 mil mylar	1.0 mil
	B_5		1.45 mm		0.7				
	E_6	LiD	2.9 mm	-300	2	10 × 9	9 × 8	1 mil mylar	1-2 mils
	B_6		2.9 mm		~1.0				
	E_7	LiD	4.6 mm	-500	7	10 × 9	9 × 8	1 mil mylar	1-2 mils
	B_7		4.75 mm		7				

[a]The detectors will function properly at least twice this voltage.

[b]At 20°C.

[c]Coated with aluminum.

Table 2-2. Characteristics of electron channels.

Channel No.	Center energy in keV at +21°/0°/-20°C	Channel[a] width FWHM at 0°C	Base[b] width at 0°C	Pulse-height discrimination levels in keV	Acceptance[d] angle	Geometrical factor cm^2 keV sr at 21°/0°/-20°C
1	74/79/83	22	45	51-91	7.6°	0.177/0.180/0.159
2	147/158/168	27	54	101-183	5.9°	0.272/0.277/0.281
3	250/266/282	41	71	194-346	4.7°	0.362/0.390/0.466
4	456/479/500	66	101	329-587	3.5°	0.583/0.605/0.625
5	776/822/866	250	370	453-1051	5.3°	4.18/4.43/4.64
6	1455/1530/1600	352	520	850-1877	4.1°	8.10/8.57/9.05
7	2680/2820/2970[c]		540	1720-3230	2.5°	3.66/3.88/4.10[c]

[a]Measured from pulse height distribution with contribution of detector noise removed.

[b]Full range of energy detected, calculated. Resolution FWHM ~ 1/2 base width.

[c]From temperature dependance of channels 5 and 6 for data at 0° and -20°C.

[d]Perpendicular to direction of focusing in the magnets, calculated effective width (50% less and 50% greater). The response is approximately triangular so that zero response comes at about 3.4 times this value. The acceptance angle in the plane of focusing is only slightly channel dependant calculating to 29° for channels 1-4 and 31° for channels 5-7. This response is approximately rectangular.

2.6 ELECTRON SPECTROMETER ELECTRONICS

A block diagram of the electronics is shown in the electrical drawing Fig. 2-4. The pertinent circuit diagrams are indicated by the LE*-numbers attached to the various blocks. These circuit diagrams are as follows:

- preamplifiers, Figs. 2-5 and 2-6;
- amplifiers, Fig. 2-7;
- discriminator driver, Fig. 2-8;
- pulse separation network, Fig. 2-9;
- differential discriminator, Fig. 2-10;
- discriminator and logic, Fig. 2-11; and
- amplifier and integral discriminator, Fig. 2-12.

Further relation to the rest of the system is given in the OPEP interconnect diagram, Fig. 2-13.

The preamplifiers for the detector pulses are of the low-noise charge-sensitive type. The charge-sensitive preamplifier has the virtue of being insensitive to variations in detector capacity. The preamplifier used for channels 1 and 2 are designed to provide especially low noise. The noise expressed in terms of pulse-height resolution in units of full width at half maximum is 4 keV + 0.1 keV/pF in which the last term takes into effect the capacitive contribution. Lower powered preamplifiers were used for the higher energy channels. The noise for these units is 11 keV + 0.22 keV/pF.

*The LE-numbers refer to the identification numbers used in the Lawrence Radiation Laboratory Electrical Engineering Department at Livermore. The number 12854 is common to all the drawings related to this project.

FOLDOUT FRAME 1

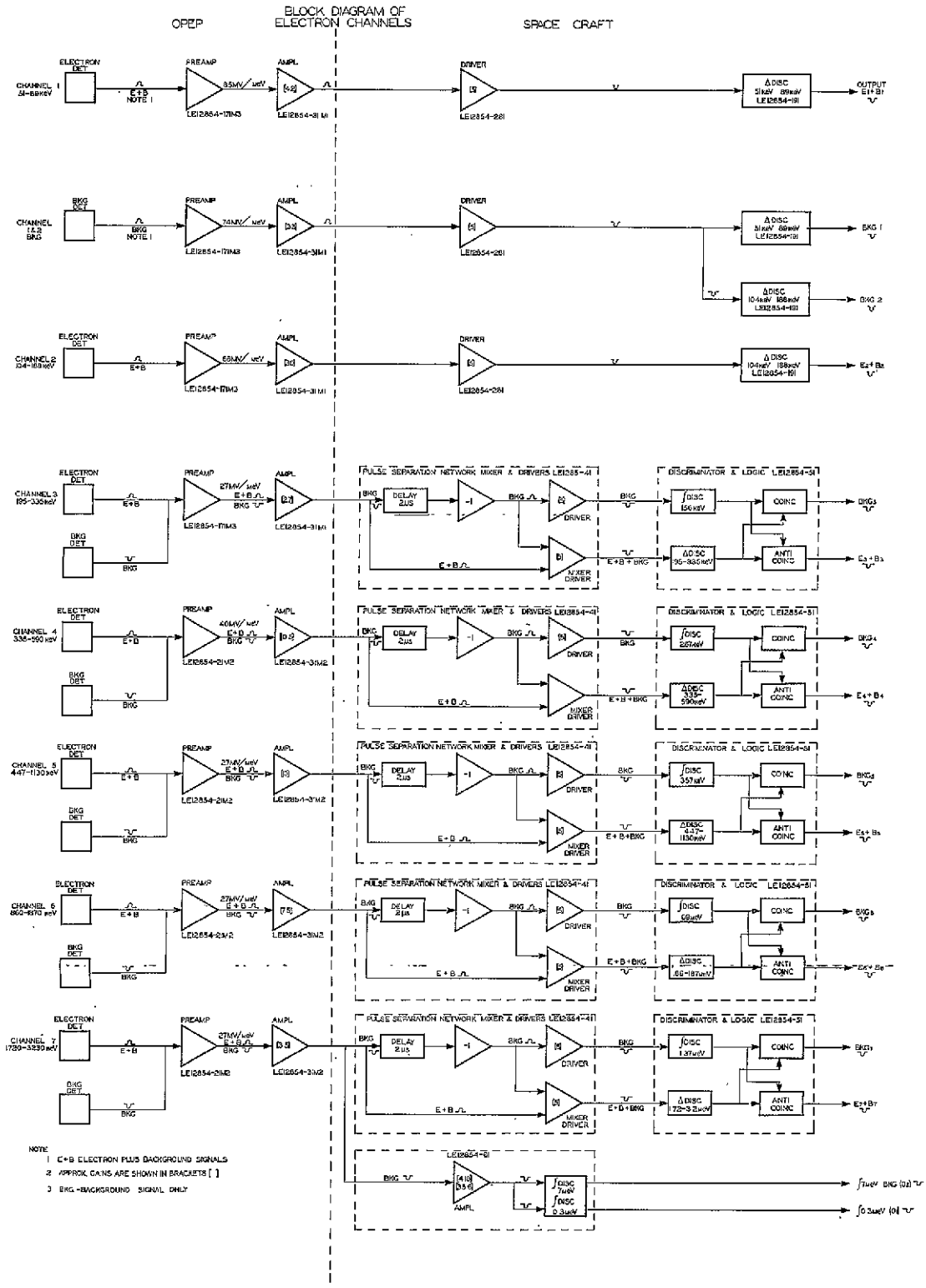

Fig. 2-4. Block diagram of electron channels (LE 12854-1 sheet 1).

FOLDOUT FRAME 2

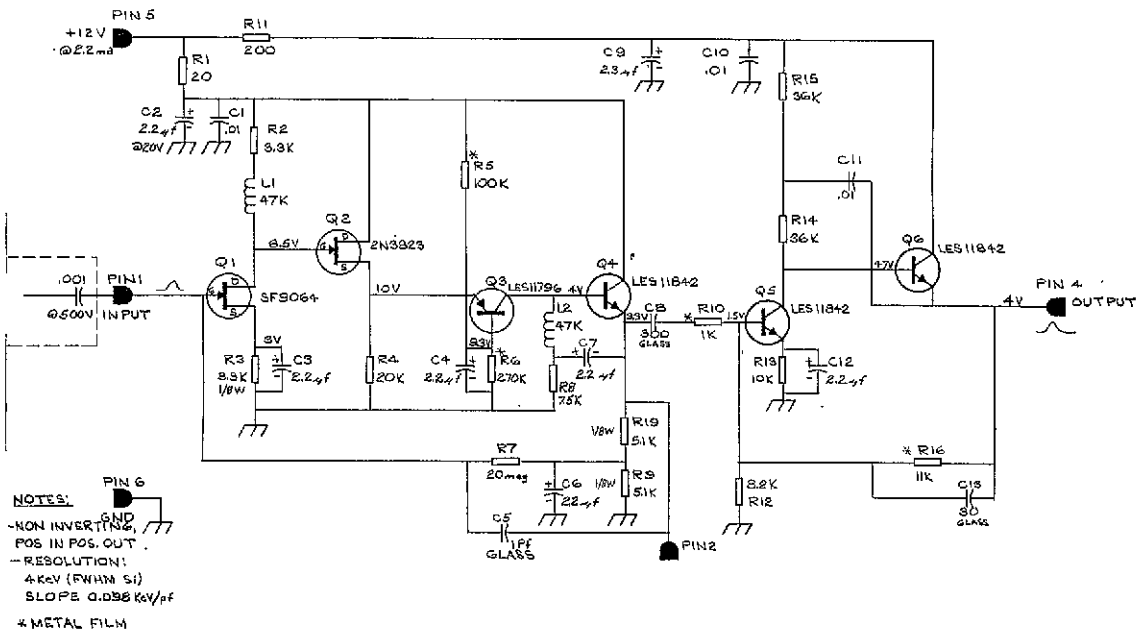

Fig. 2-5. Charge sensitive FET preamplifier for channels E_1, B_1, B_2, E_2, P_1, P_{B1} (LE 12854-171M3).

MODULE NO. 2

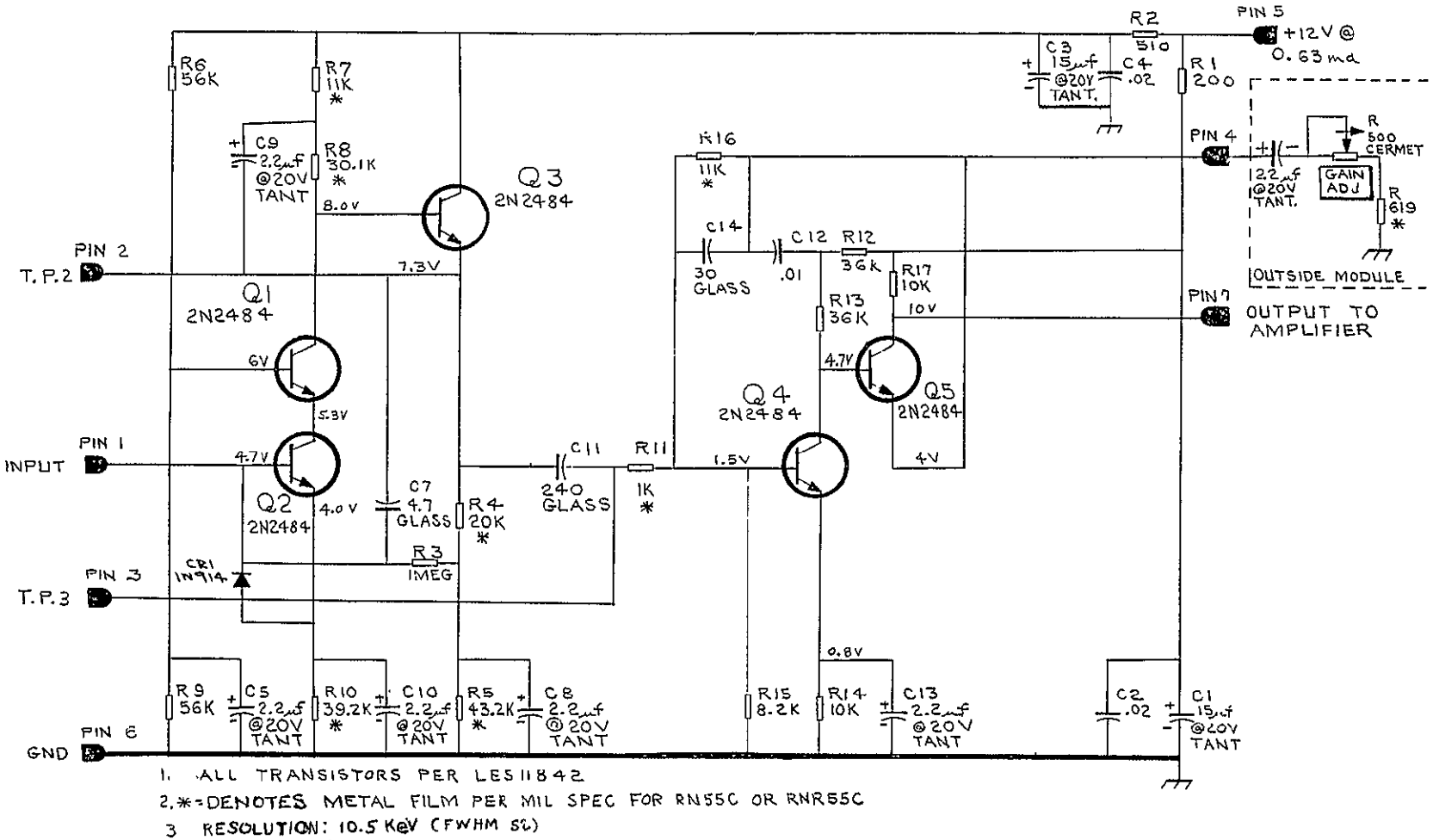

1. ALL TRANSISTORS PER LES11842
2. *=DENOTES METAL FILM PER MIL SPEC FOR RN55C OR RNR55C
3 RESOLUTION: 10.5 KeV (FWHM 5%)

Fig. 2-6. Charge sensitive preamplifier (LE 12854-21M2).

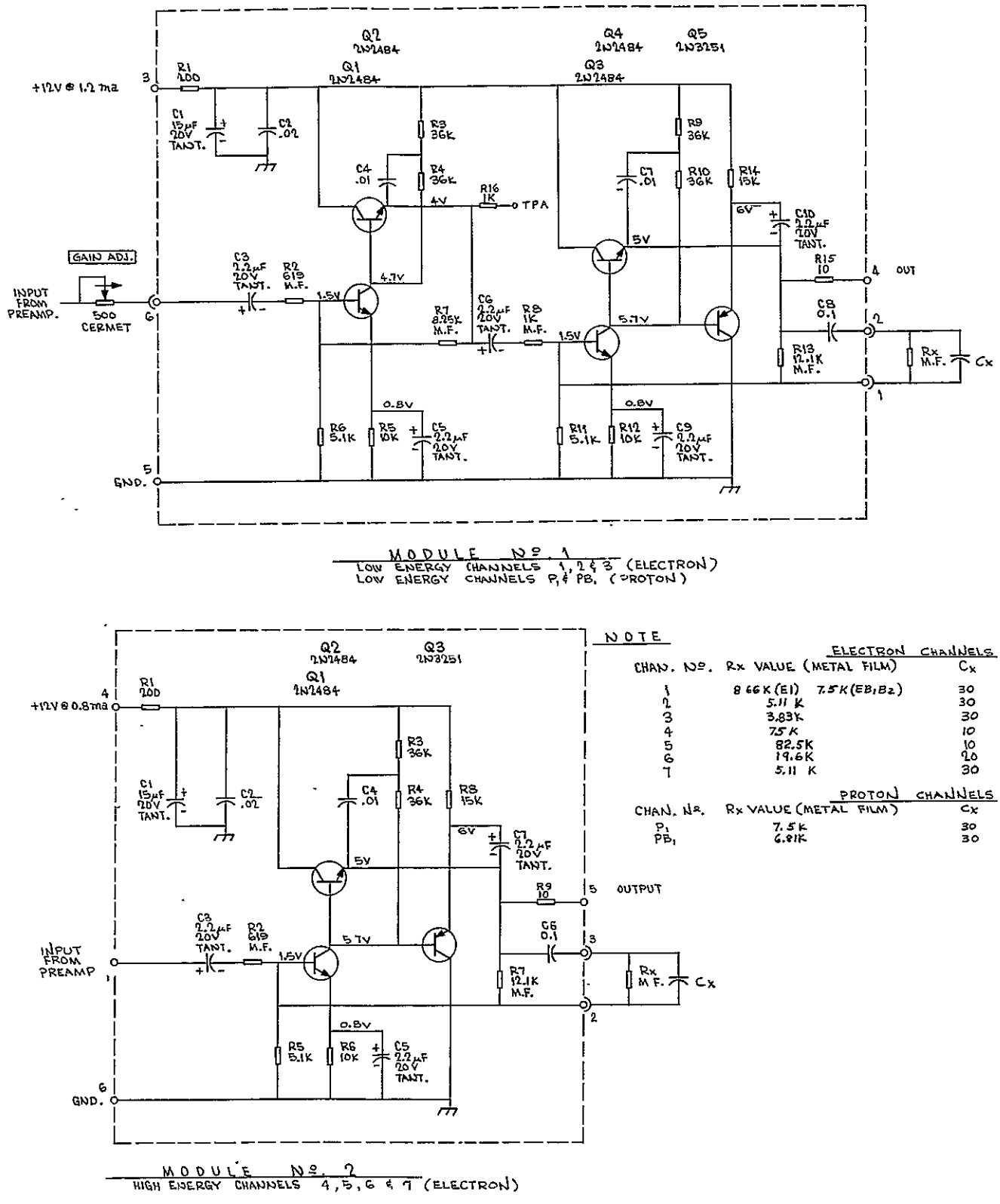

Fig. 2-7. Bipolar amplifier (LE 12854-31).

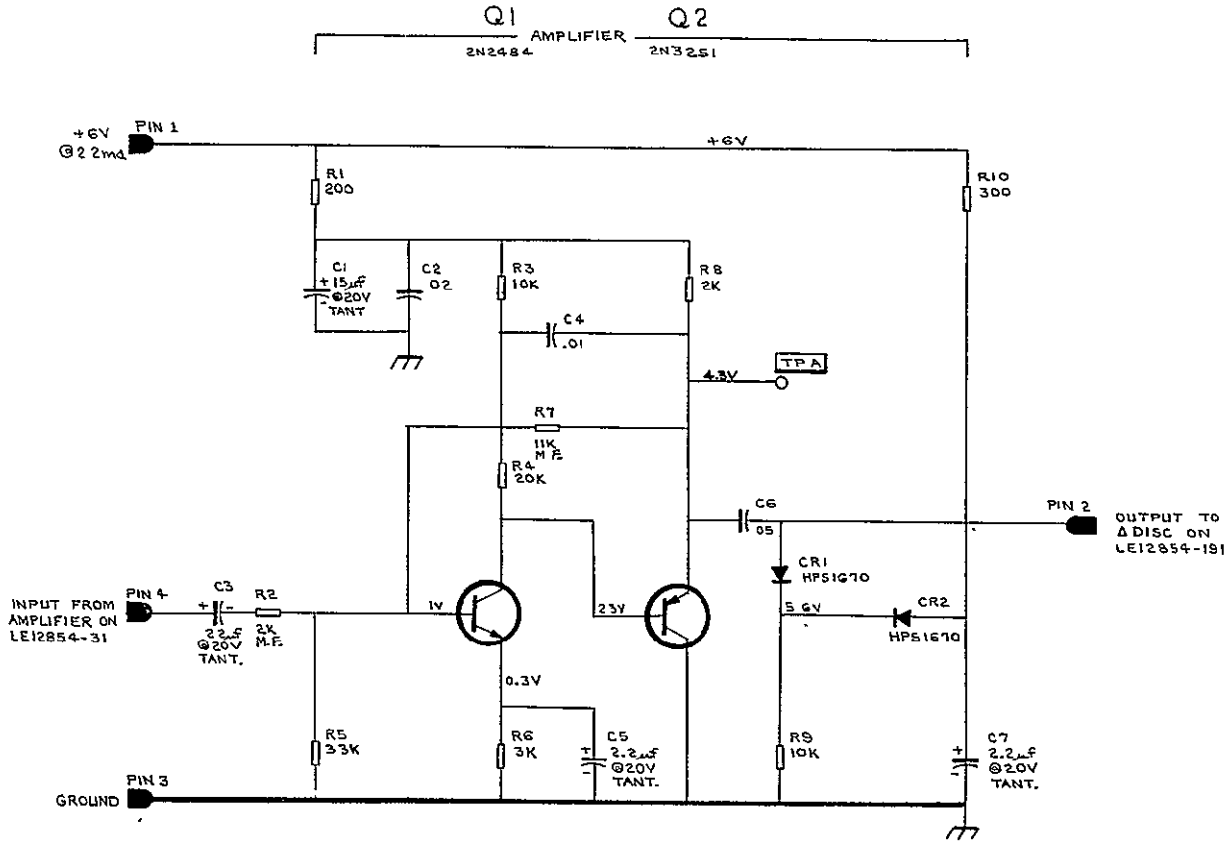

Fig. 2-8. Low-energy amplifier discriminator driver (LE 12854-281).

Two schemes are used to handle the pulses from the detectors. For the higher energy channels, 3 through 7, the pulses from the background detectors are mixed at the preamplifier (being differentiated by polarity) and then handled by the same linear electronics. The ability to use the same differential discriminator is provided by delay-line clipping the incoming pulses (Fig. 2-9) so as to provide in both cases the negative pulse required for the differential discriminator. The pulses from the output of the discriminator (Fig. 2-11) are logically routed (on the basis of which comes first, the negative or positive excursion of the pulse) to give the electron plus background and the background outputs. The use of this procedure insures that the background pulses are handled in the same manner as the electron pulses. In addition, the delay-line clipper provides excellent base-line restoration for the pulses, which is of importance at high counting rates (including overload pulses from protons) and for minimizing the effects of radiation damage. The differential discriminator[2] is unique. It has a two-pulse resolution of ~2 μsec, operates at zero standby power with a temperature coefficient of 0.025%/°C and cannot be tripped by overload pulses.

[2]D. Peters, Lawrence Radiation Laboratory, private communication (March 19, 1963).

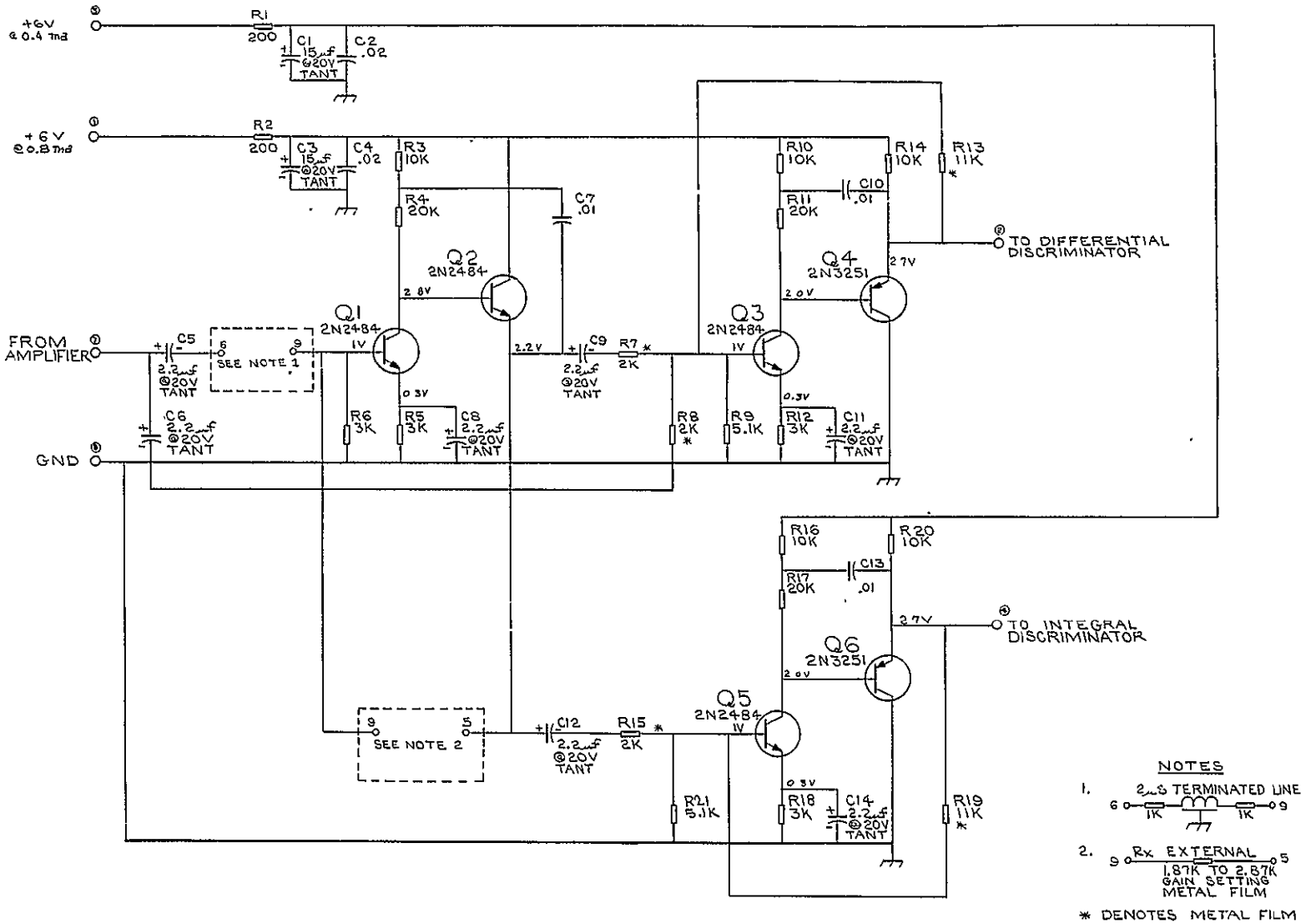

Fig. 2-9. Mixer and driver amplifiers pulse separation network (LE 12854-41).

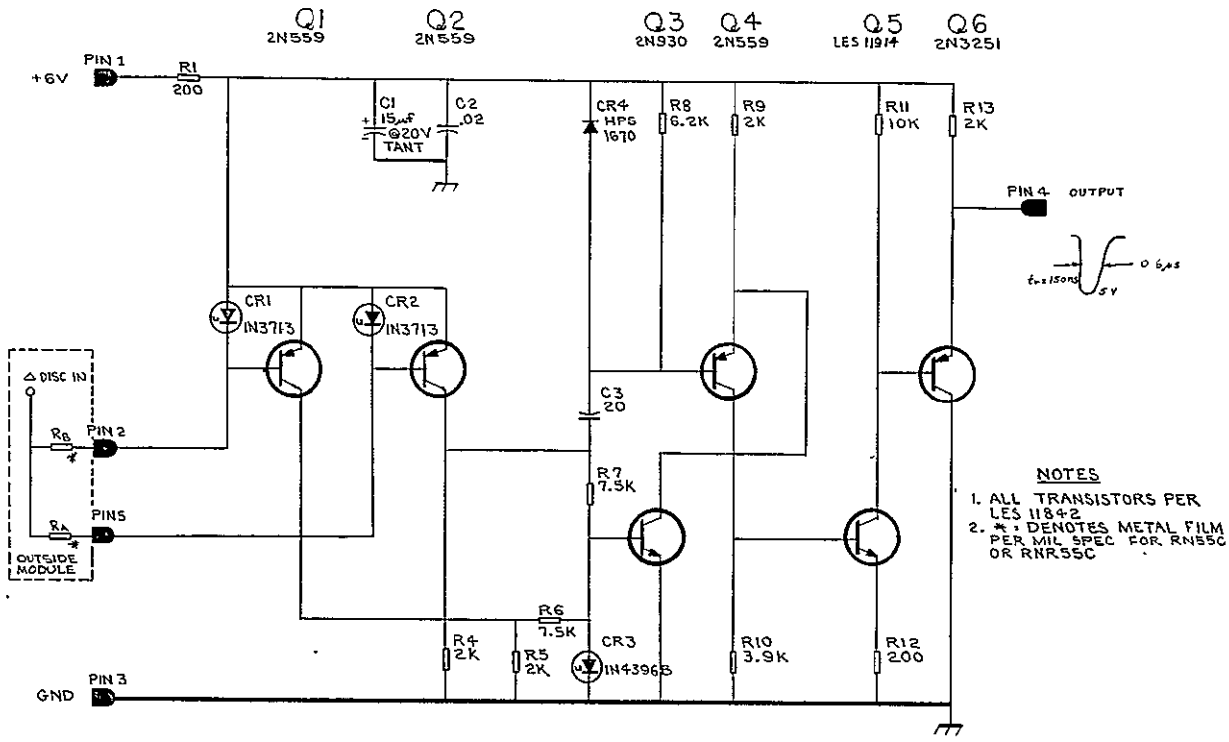

Fig. 2-10. Differential discriminator (LE 12854-191).

For the following discussion of the circuit, refer to Fig. 2-10. Operation is via negative pulses. If only tunnel diode CR2 trips, the pulse will couple through to the output, the output occurring when CR2 resets, thus providing a negative differentiated pulse at the base of Q4. If, however, CR1 trips, the combined current flow via R6 and R7 will trip CR3. During the fall of the input signal to the differential discriminator, the current via R7 is enough to keep CR3 tripped. Also Q3 is in hard saturation and the memory (~0.7 μsec, temperature compensated by CR3) is adequate to anticoincidence the output pulse. This anticoincidence procedure is further used in the proton logic circuits.

For energy channels 1 and 2, paralleling the detectors into the preamplifier is not feasible because of the high capacity and resultant increased noise. For these cases, detectors 1 and 2 are identical and a common background detector is provided. The logic is shown in Fig. 2-4.

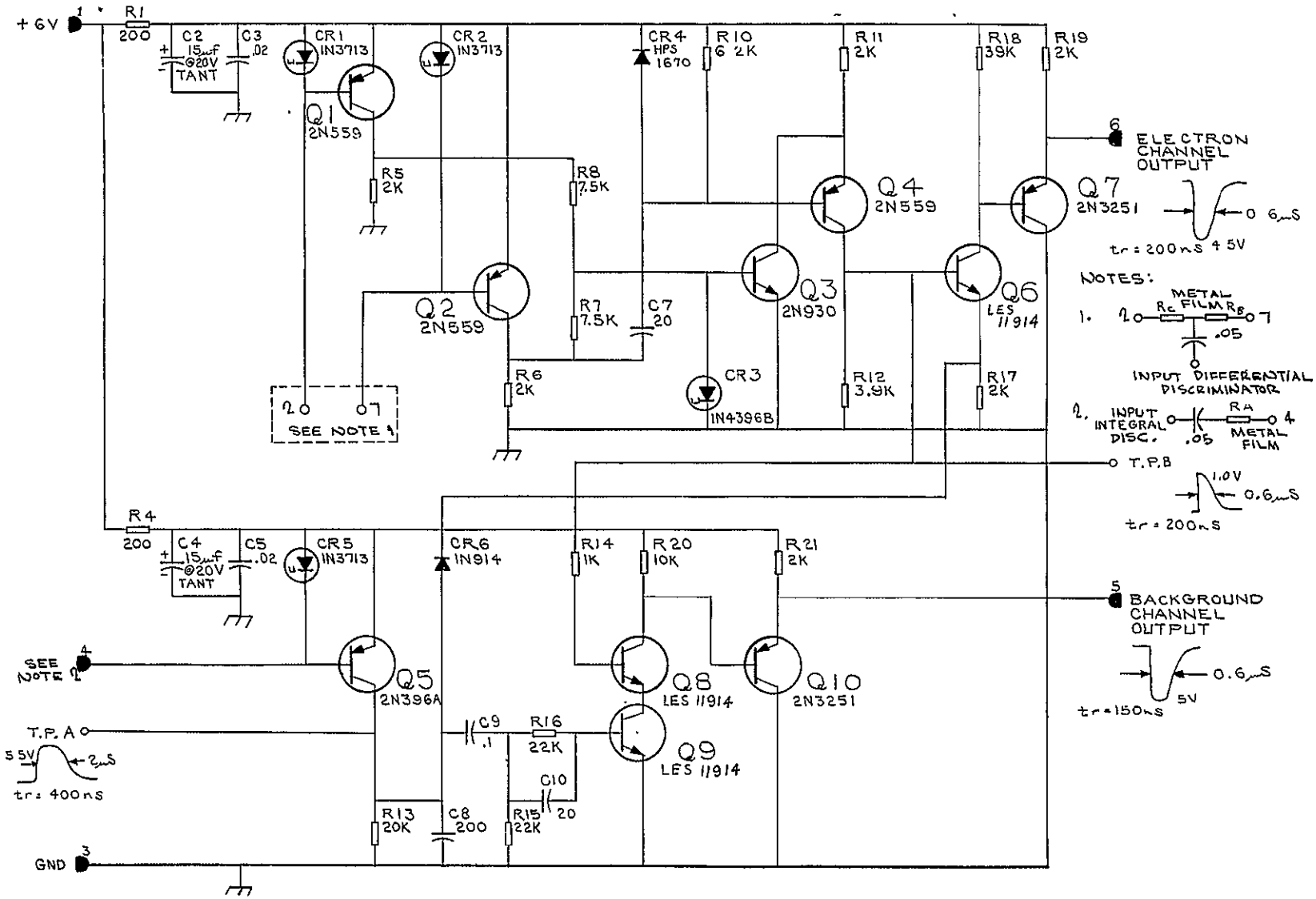

Fig. 2-11. Differential and integral plus electron channel logic discriminators (LE 12854-51).

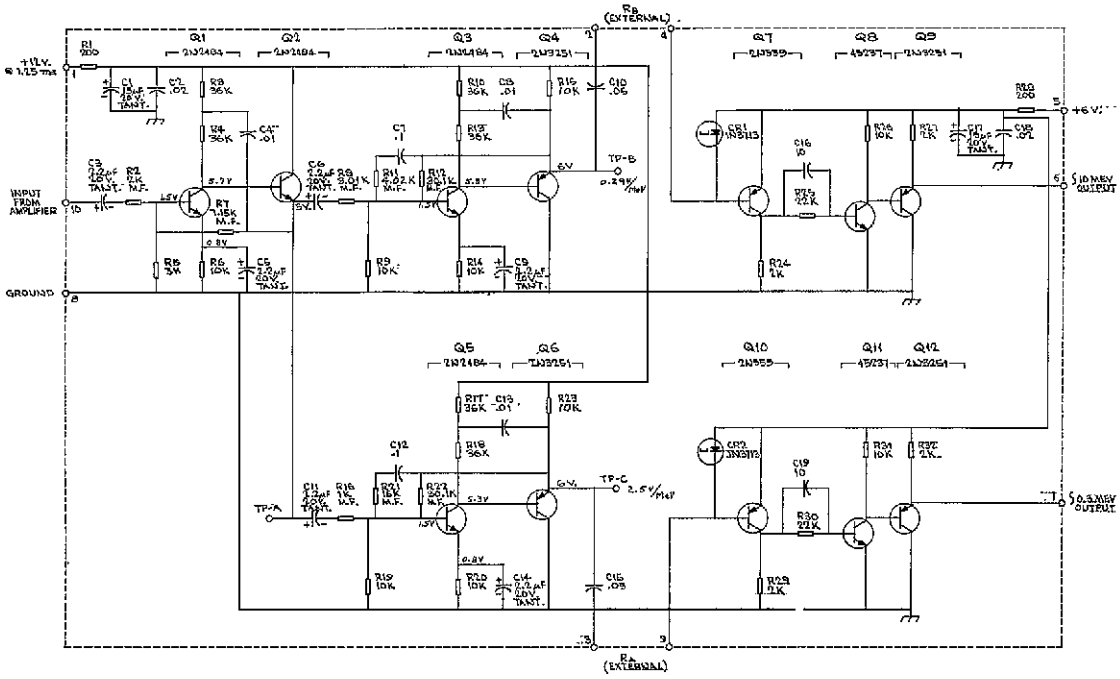

Fig. 2-12. Integral O_1 and O_2 background channel amplifier-discriminator (LE 12854-61).

FOLDOUT FRAME 1

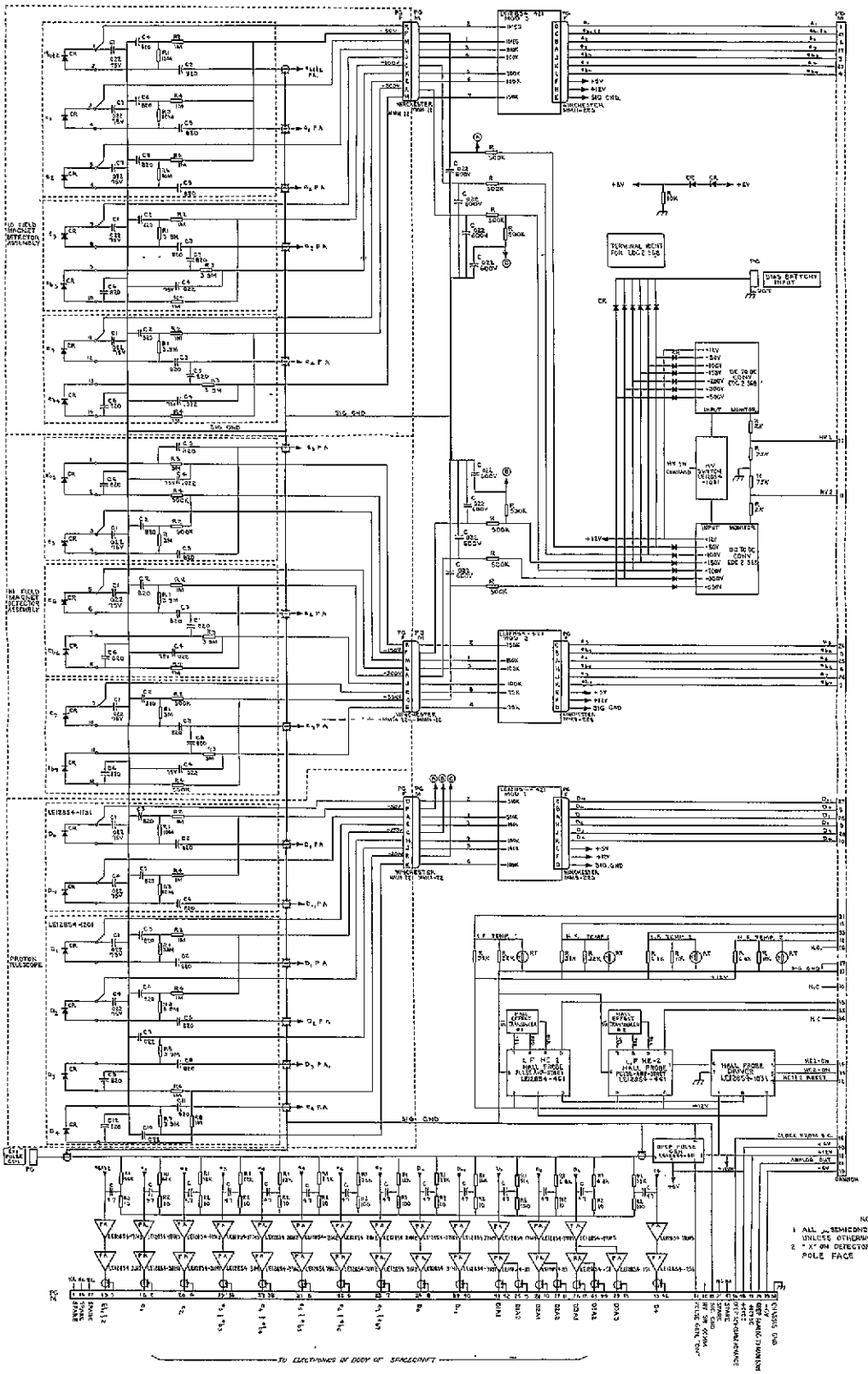

FOLDOUT FRAME 2

Fig. 2-13. OPEP interconnection diagram (LE 12854-1211).

3. Proton and Alpha Particle Detection System

3.1 INTRODUCTION

The proton telescope measures the proton and alpha particle fluxes and energy spectra over as much of the energy range covered by the space craft orbit as possible. A large dynamic range was provided so that the spectrometer could provide some useful data in the region outside the earth's magnetic field and still be able to handle the high counting rates expected in the trapping regions.

The design of the proton spectrometer was strongly influenced by the presence of the electron spectrometer, since the magnet provides a ready made sweeping field to eliminate lower than 4-MeV electrons and also provides shielding for both electrons and protons of higher energies.

The large energy range desired, (approximately 0.1 to >75 MeV), led to the choice of an E, dE/dX type of detection system. The telescope has four detectors and two absorbers in series. The particle type and energy is determined by measuring the energy deposited in each detector penetrated. Diffused-junction solid-state detectors were used because of their small size, good energy resolution, and relatively good resistance to radiation damage compared to other types of detectors.

3.2 THE PROTON TELESCOPE

The arrangement of the detectors in the proton telescope is shown in Fig. 1-2. The physical characteristics are given in Table 3-1. Designating the components of the telescope in order from the entrance aperture they are: detector D_1, detector D_2, an aluminum absorber 0.674 mm thick, detector D_3, a gold absorber 1.57 mm thick and detector D_4. The telescope is located between the pole faces of the high-field magnet of the electron spectrometer, directly in line with the entrance collimator. Two smaller detectors, D_0 centered in the plane of the magnet pole pieces but 12.5° off the main telescope axis, and D_1 located above D_0 and not on a line of sight through the collimator, provide the lowest energy channel. D_1 is covered with 1 mil of aluminized mylar and is used as a background detector for D_0.

The sizes and positions of the detectors in the telescope are arranged so that the acceptance angle of the collimator includes essentially all of the active volume of each detector. Both the D_0 and D_1 detectors are directly exposed to the open collimator, hence are coated with 1000-1500 Å of aluminum as a light shield. Although D_2 is shielded from light by D_1, it is also coated with aluminum for interchangeability reasons. All detectors have 0.3—0.5 micron thick gold back contacts. The edges of the aluminum coating are light sealed to the detector mounts with a black paint which reduces the effective area of D_0, D_1, and D_2 somewhat from the maximum active area.

The detectors in the first flight package were made by Robert Lothrop at the Lawrence Radiation Laboratory, Berkeley, California. Those in the second flight model were made by Nuclear Equipment Corporation and Nuclear Technology

Table 3-1. Characteristics of proton detection system.

Detector No.		D_0	D_{-1}	D_1	D_2	D_3	D_4
Dimensions	∥ pole face	0.30 cm	0.29 cm	1.21 cm	1.26 cm	—	—
inside	⊥ pole face	0.48 cm	0.47 cm	0.874 cm	0.892 cm	—	—
paint	Area	0.143 cm^2	0.136 cm^2	1.06 cm^2	1.12 cm^2	—	—
Sensitive	∥ pole face	0.407 cm	0.407 cm	1.49 cm	1.49 cm	1.60 cm	2.06 cm
area	⊥ pole face	0.615 cm	0.615 cm	0.993 cm	0.993 cm	1.125 cm	1.461 cm
dimensions	Area	0.250 cm^2	0.250 cm^2	1.48 cm^2	1.48 cm^2	1.80 cm^2	3.01 cm^2
Geometric	∥ pole face	0.40 cm	0.40 cm	1.29 cm	1.40 cm	1.55 cm	1.89 cm
collimated	⊥ pole face	0.60 cm	0.60 cm	0.93 cm	1.05 cm	1.19 cm	1.49 cm
dimensions	Area	0.24 cm^2	0.24 cm^2	1.20 cm^2	1.47 cm^2	1.84 cm^2	2.82 cm^2
Serial No.		D-0-14	D-0-12	D-1-12	D-1-17	D-3-13	D-3-14
Silicon thickness		100 μ	100 μ	236 μ	247 μ	470 μ	470 μ
Front surface dead layer including aluminum		0.29 μ	0.24 μ	0.28 μ	0.20 μ	0.14 μ	0.17 μ
Back surface gold thickness		—	—	0.38 μ	0.36 μ	0.40 μ	0.40 μ
Solid angle		1.44×10^{-2} sr	—	1.23×10^{-2} sr	1.12×10^{-2} sr	9.57×10^{-3} sr	7.04×10^{-3} sr
Noise FWHM (20°C)		10 keV	10 keV	16 keV	17 keV	34 keV	25 keV
Punch-through voltage		50 V	50 V	100 V	90 V	170 V	160 V
Leakage current at 20°C		0.14 μA	0.12 μA	1.6 μA	1.7 μA	3.9 μA	2.2 μA

Corporation, both in San Carlos, California, under the direction of Dr. Louis Wang.

The first detector in the telescope, D_1, serves as both an E and dE/dX detector. Protons of less than 5.2 MeV are stopped in this detector, giving a full energy pulse. Above 5.2 MeV, protons penetrate D_1 and can deposit energy in one or more of the succeeding detectors. Threshold discriminators on the outputs of the various detectors, combined with coincidence and anticoincidence circuits divide the entire energy range into seven proton and three alpha particle channels in an approximately logarithmic manner. The channel designations, energy intervals and logic statements are given in Table 3-2.

As can be seen from the logic statement table, four discrimination levels are provided for D_1 and D_2, five for D_3, and three for D_4. Logical combination of these determine the various energy channels. For example, channel P_5 is begun by signals in D_1 greater than 1.32 MeV, and in D_2 greater than 1.31 MeV, and ended by a signal greater than 0.20 MeV in D_3 which is shown as an anticoincidence. A pulse in D_1 greater than 5.84 MeV or in D_2 greater than 5.75 MeV would indicate either an α particle count or background and consequently is used in anticoincidence.

Since the intense low-energy portion of the electron spectrum is prevented from reaching the telescope, the primary sources of background are from protons and bremsstrahlung that have reached the detectors by penetrating the wall of the spectrometer. This background is determined by logically interchanging the roles of the detectors. This can be done effectively for P_2, P_3, and P_4. A reasonable background channel can be provided for P_5 by the same sort of interchange. The background for P_6 comes from measuring those particles that have passed completely through the telescope. The alpha background (α_{B_1}) again comes from interchanging the roles of D_1 and D_2. Channel

Table 3-2. Logic of proton detection system.

Channel designation	Energy range (MeV)	Geometry (cm^2-sr)	Logic statement discriminator settings (MeV)
P_1	0.10 - 0.15	2.06×10^{-3}	$D_0(0.070)[\overline{D_0(0.120)}]$
P_{B1}	0.10 - 0.15	—	$D_{-1}(0.070)[\overline{D_{-1}(0.120)}]$
P_2	0.23 - 0.57	1.30×10^{-2}	$D_1(0.20)[\overline{D_1(0.55)} + \overline{D_2(0.525)}]$
P_3	0.57 - 1.35	1.30×10^{-2}	$D_1(0.55)[\overline{D_1(1.32)} + \overline{D_2(0.525)}]$
P_4	1.35 - 5.40	1.30×10^{-2}	$D_1(1.32)[\overline{D_1(5.84)} + \overline{D_2(0.525)}]$
P_5	5.60 - 13.3	1.25×10^{-2}	$D_1(1.32)D_2(1.31)[\overline{D_1(5.84)} + \overline{D_2(5.75)} + \overline{D_3(0.20)}]$
P_6	14.0 - 46.0	1.72×10^{-2}	$D_2(0.525)D_3(1.24)[\overline{D_2(5.75)} + \overline{D_3(9.05)} + \overline{D_4(0.20)}]$
P_7	43 - 94	1.98×10^{-2}	$D_2(0.20)D_3(0.57)D_4(0.78)[\overline{D_2(1.31)} + \overline{D_3(1.58)}]$
E_8	E > 4		$D_2(0.20)D_3(0.57)[\overline{D_2(0.525)} + \overline{D_3(1.24)} + \overline{D_4(0.20)}]$
α_1	5.92 - 21.2	1.30×10^{-2}	$D_1(5.84)[\overline{D_2(0.525)} + \overline{D_3(0.20)}]$
α_2	22.8 - 53.1	1.25×10^{-2}	$D_1(5.84)D_2(5.75)[\overline{D_3(0.20)}]$
α_3	56.8 - 104	1.72×10^{-2}	$D_1(1.32)D_2(1.31)D_3(9.05)[\overline{D_1(5.84)} + \overline{D_2(5.75)} + \overline{D_4(0.20)}]$
P_{B2}			$D_2(0.20)[\overline{D_1(0.20)} + \overline{D_2(0.525)}]$
P_{B3}			$D_2(0.525)[\overline{D_1(0.55)} + \overline{D_2(1.31)}]$
P_{B4}			$D_2(1.31)[\overline{D_1(0.55)} + \overline{D_2(5.75)}]$
P_{B5}			$D_2(1.31)D_3(0.57)[\overline{D_2(5.75)} + \overline{D_3(1.58)} + \overline{D_4(0.20)}]$
P_{B6}			$D_3(0.20)D_4(0.20)[\overline{D_3(0.57)} + \overline{D_4(0.55)}]$
α_{B1}			$D_2(5.75)[\overline{D_1(0.55)} + \overline{D_3(0.20)}]$
α_{B2}			$D_1(5.84)D_2(5.75)D_3(9.05)D_4(0.78)$
α_{B3}			$D_1(0.20)D_2(0.20)D_3(0.55)D_4(0.55)$

α_{B_2} provides a measure of star production in the telescope and α_{B_3} a measure of relativistic alpha particles.

Figure 3-1 shows the energy deposited in each detector, including the effects of the aluminum coatings, the gold backing, and detector dead layers. The aluminum and gold absorbers extend the energy range of the telescope. The energy intervals of the telescope channels are also shown.

The effect of the paint edging on the first two detectors is shown in Fig. 3-2 and Table 3-3. The effect of the paint is to cause the detection of higher energy protons in a channel than was originally intended. The effect on the counting rates in the respective channels for a flat spectrum is calculated in Table 3-3.

3.3 PROTON CHANNEL P_1

The proton channel P_1 is derived from detector D_0. This detector and its associated background detector D_{-1} were included in the design in order to take advantage of the lower noise level possible with a small detector. After making allowance for the dead layer, aluminum light shield, and average noise level (assuming the worst case temperature), we were able to set channel P_1 at 0.102 to 0.150 MeV.

The low energy protons detected in D_0 are deflected in the magnetic field so as to move the virtual position of the detector 4.8° closer to the center line of the proton telescope than the 12.5° indicated

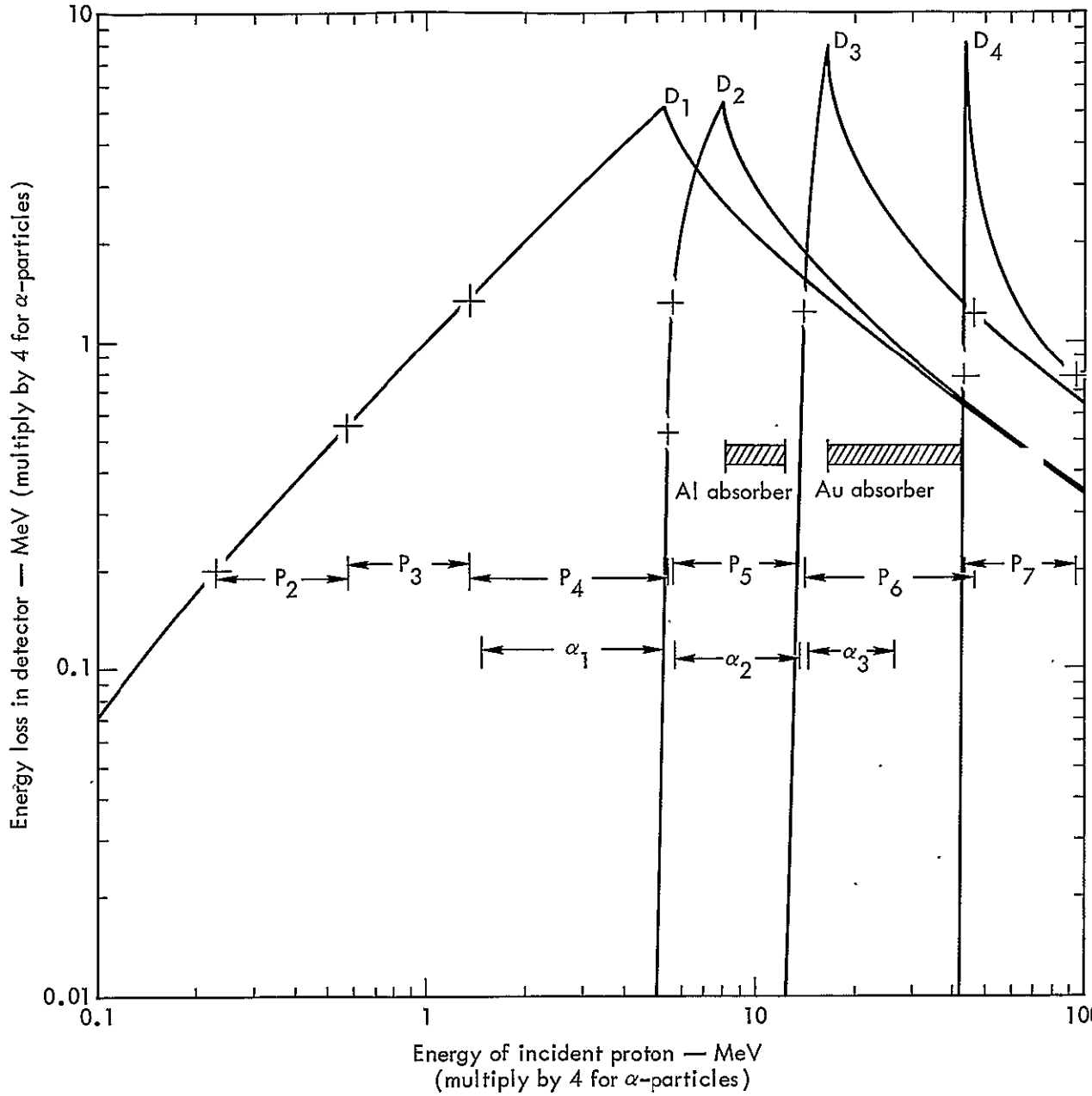

Fig. 3-1. Energy loss characteristics of the proton telescope.

by the physical constraints. This deflection greatly enhances the geometrical factor, otherwise the edge of the external collimator is a factor in defining the acceptance angle rather than the slit of the spectrometer.

3.4 ELECTRON CHANNEL E_8

Electrons with minimum ionizing energy reach the proton telescope. The expected pulse-height distribution from this source in D_1 and D_2 is a minimum of

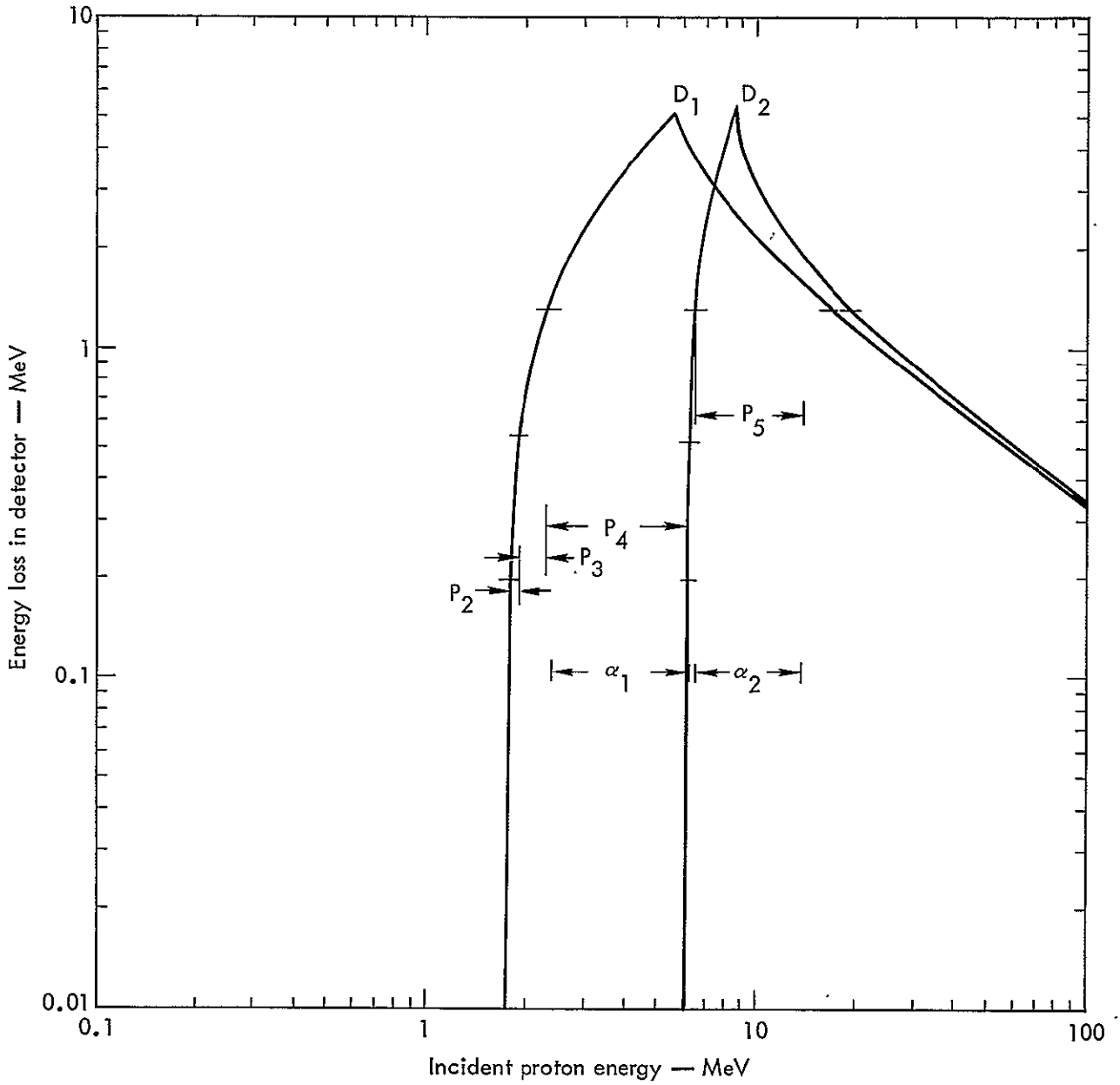

Fig. 3-2. Energy loss characteristics through the painted portion of the detectors.

~100 keV, peaking at ~130 keV and falling off rapidly at higher energies. The distribution in D_3 would be just twice these values except that a gold absorber has been placed directly behind D_3. The gold presents a large elastic scattering cross section to the electrons. The directionality of the scattered electron is roughly isotropic so that the electrons that pass back through D_3 and D_2 do so at an oblique angle. Hence the distribution of total energy left in D_3 peaks at ~600-700 keV and in D_2 peaks at ~300 keV. The efficiency for such a process is ~10% of the incident particles. In providing this energy channel (E_8), the backgrounds for the lower-energy proton channels are raised, but since there is usually such

Table 3-3. Effect of paint on D_1 and D_2.

Channel designation	Energy range (MeV)[a]	Solid angle (sr)	Effective painted area (cm^2)	Geometry of painted area (cm^2-sr)	Percent of unpainted geometry	Percent effect[b] in channel for flat spectrum
P_2	1.8 - 1.9	0.0112	0.244	2.73×10^{-3}	21.0	6.2
P_3	1.9 - 2.3	0.0112	0.244	2.73×10^{-3}	21.0	10.8
P_4	2.3 - 6.2	0.0112	0.244	2.73×10^{-3}	21.0	20.2
P_5	6.4 - 13.3	0.0110	0.0874	9.59×10^{-4}	7.7	6.9
α_1	9.6 - 25.0	0.0112	0.244	2.73×10^{-3}	21.0	21.0
α_2	26.0 - 53.5	0.0110	0.0874	9.59×10^{-4}	7.7	7.0

[a]Protons of this energy range will leave pulses of measurable amplitude in the respective channel. See Fig. 3-2.

[b]The contribution to the counting rate of the respective channel by the protons so indicated.

an abundance of low-energy protons relative to energetic electrons, this source of background is no problem.

As yet no calibration has been done with either flight model telescope using >4-MeV electrons, so the evaluation of the data from this channel will be postponed until such a calibration can be performed.

3.5 DETECTOR PROPERTIES

Table 3-1 lists the pertinent detector properties. All detectors were checked for leakage current and noise over the anticipated temperature range of the spectrometer. In addition, front and back dead layers were measured at a variety of proton energies, and the energy response and collimation geometry were measured with protons from 0.1 to 14.5 MeV.

3.6 GEOMETRICAL FACTORS

The geometrical factors for the various channels were calculated from the measured dimensions of the detectors and telescope by a computer program that averages the solid angle seen by elemental areas of each detector over the area of the detector. The values for $g = A\Omega$ given in Table 3-1 are for the open area (unpainted) of D_1 and D_2 and for the collimated area of D_3 and D_4. The geometrical factor for particles that penetrate the paint is given in Table 3-3. The geometrical factor given for P_1 is expected to be accurate to about 10%, certainly to 15%. The geometrical factors given for the other channels should be good to 5 to 10% when measuring spectra in which proton penetration of the painted edges is not important. When penetration is important,

the uncertainties increase and can be estimated with the help of Table 3-3.

3.7 PROTON SPECTROMETER ELECTRONICS

Figure 3-3 shows the block diagram of the proton detection system. The associated circuits are as follows:

- preamplifiers, Figs. 2-5, 3-4, and 3-5;
- amplifiers, Figs. 2-7, 3-6, 3-7, and 3-8;
- discriminator driver, Fig. 2-8;
- differential discriminator, Fig. 2-10;
- integral discriminator, Fig. 3-9;
- coincidence and anticoincidence circuits, Figs. 3-10, 3-11, 3-12, and 3-13;
- logic amplifier driver, Fig. 3-14.

Further relation to the rest of the system is given in the OPEP interconnection diagram Fig. 2-13. For each detector a low noise preamplifier is provided, followed by one or more output amplifiers. Pulses of a rather large dynamic range (>30/1) are required from several detectors. Hence, to insure transmission to the spacecraft package at a level well above the anticipated spacecraft noise level (100 mV), more than one output driver has had to be provided.

All logical operations are performed in the spacecraft package. Integral discriminators (Fig. 3-9) first quantize the pulses. The pulses then are routed to the proper combination of coincidence and anticoincidence logic. An excellent example of this latter operation is shown in Fig. 3-11. The coincidence operation is the usual series gate using transistors. The anticoincidence operation is the same as used for the electron differential discriminator. In this circuit, current from two sources, a selected coincidence input, and any one of the anticoincidence inputs will trip the "memory" tunnel diode. However, only one current input is required to keep the tunnel diode in conduction. Hence, the anticondition is maintained regardless of varying pulse widths until the entire completion of the logical operations. This is further insured by the memory effect of the transistor, Q8, which is driven into saturation. This memory time is ~700 nsec (independent of temperature as it is compensated by the tunnel diode) and insures negation of the differentiated output (positive portion) of the coincidence system. It is to be emphasized that decisions are made on the trailing edges of the input pulses and that false outputs cannot result, even in the event of long-duration saturation pulses.

FOLDOUT FRAME 1

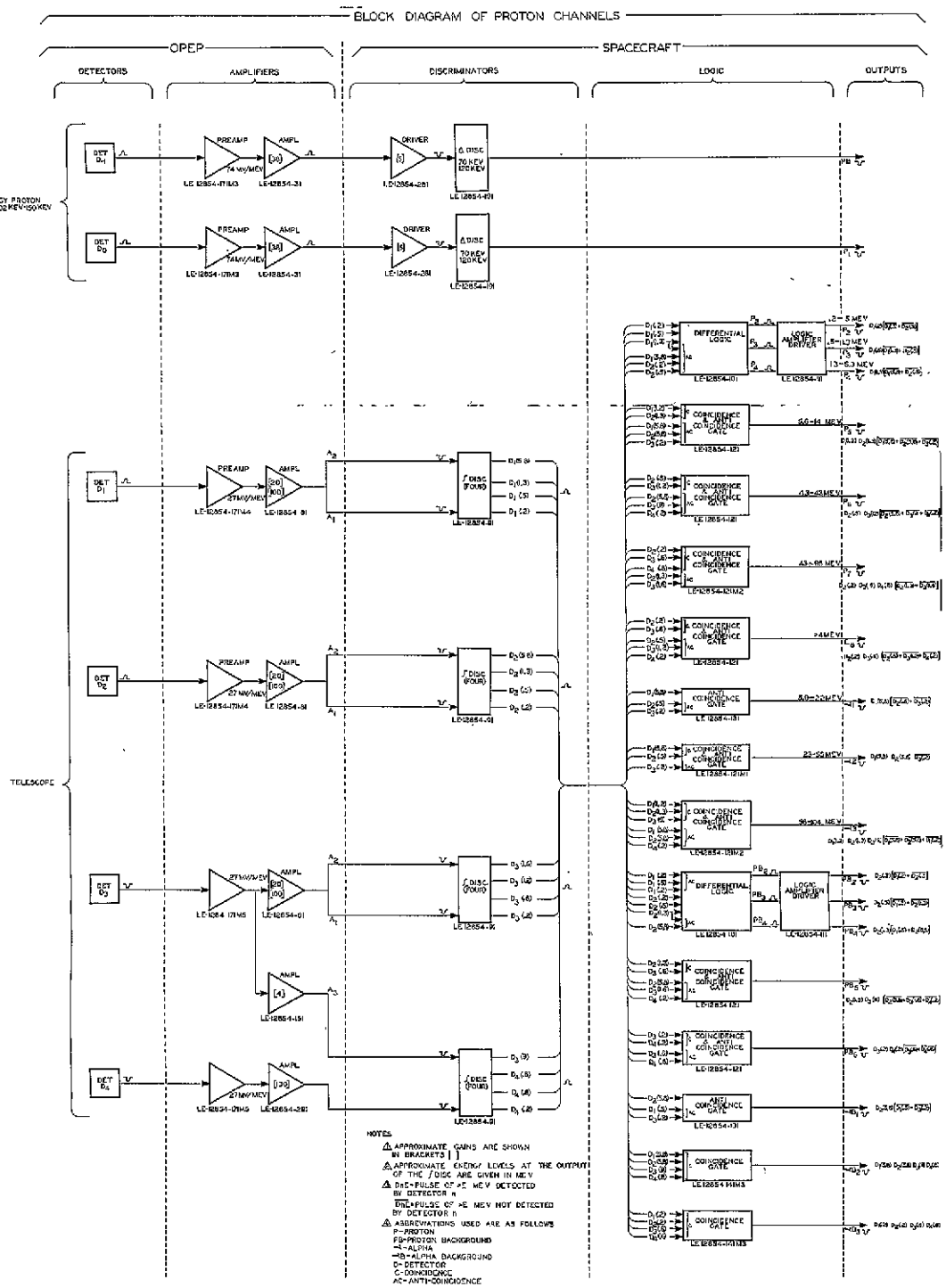

Fig. 3-3. Block diagram of proton channels (LE 12854-1 sheet 2).

FOLDOUT FRAME 2

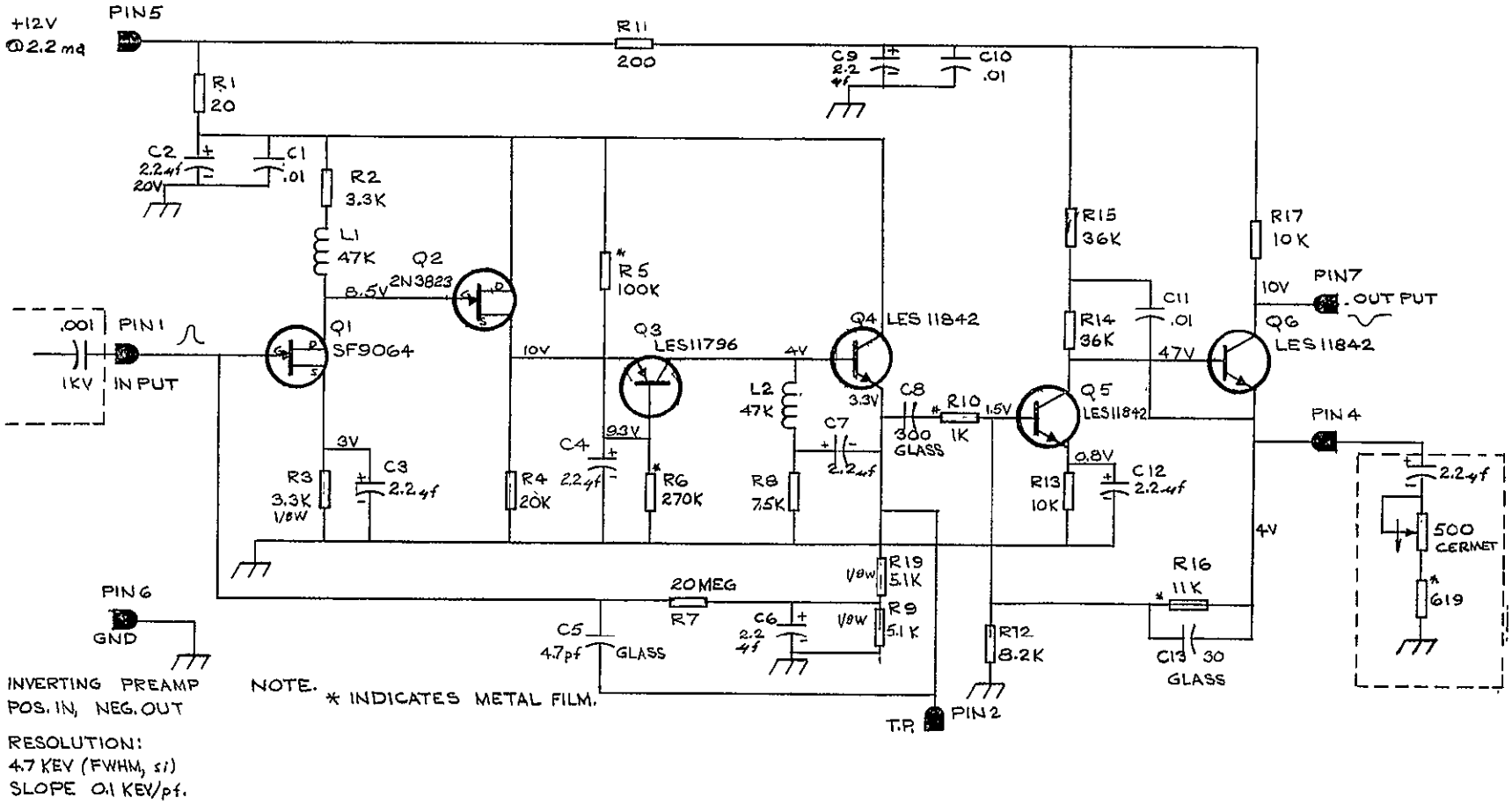

Fig. 3-4. Charge sensitive FET preamplifier for detectors D_1 and D_2 (LE 12854-171M4).

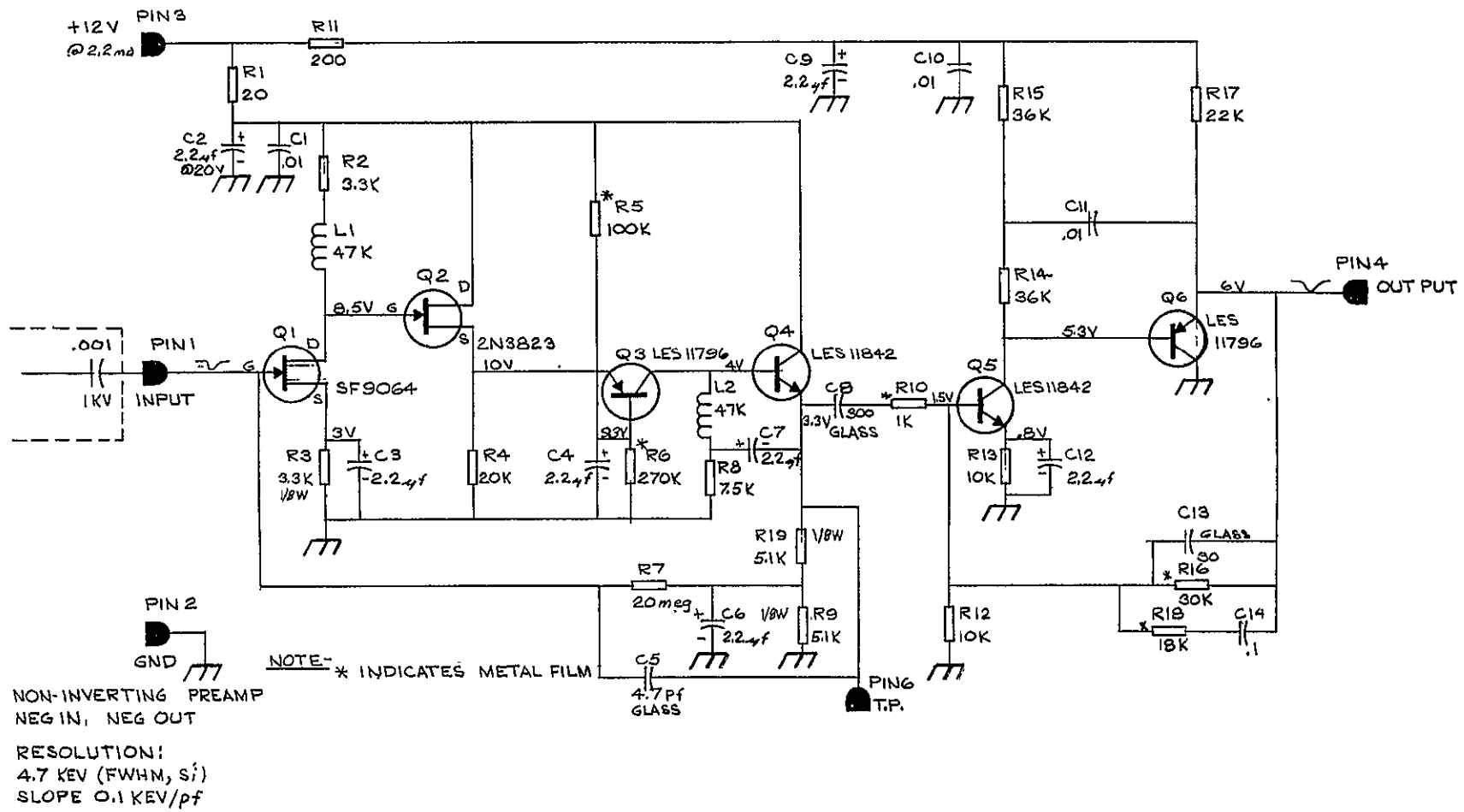

Fig. 3-5. Charge sensitive FET preamplifier for detectors D_3 and D_4 (LE 12854-171M5).

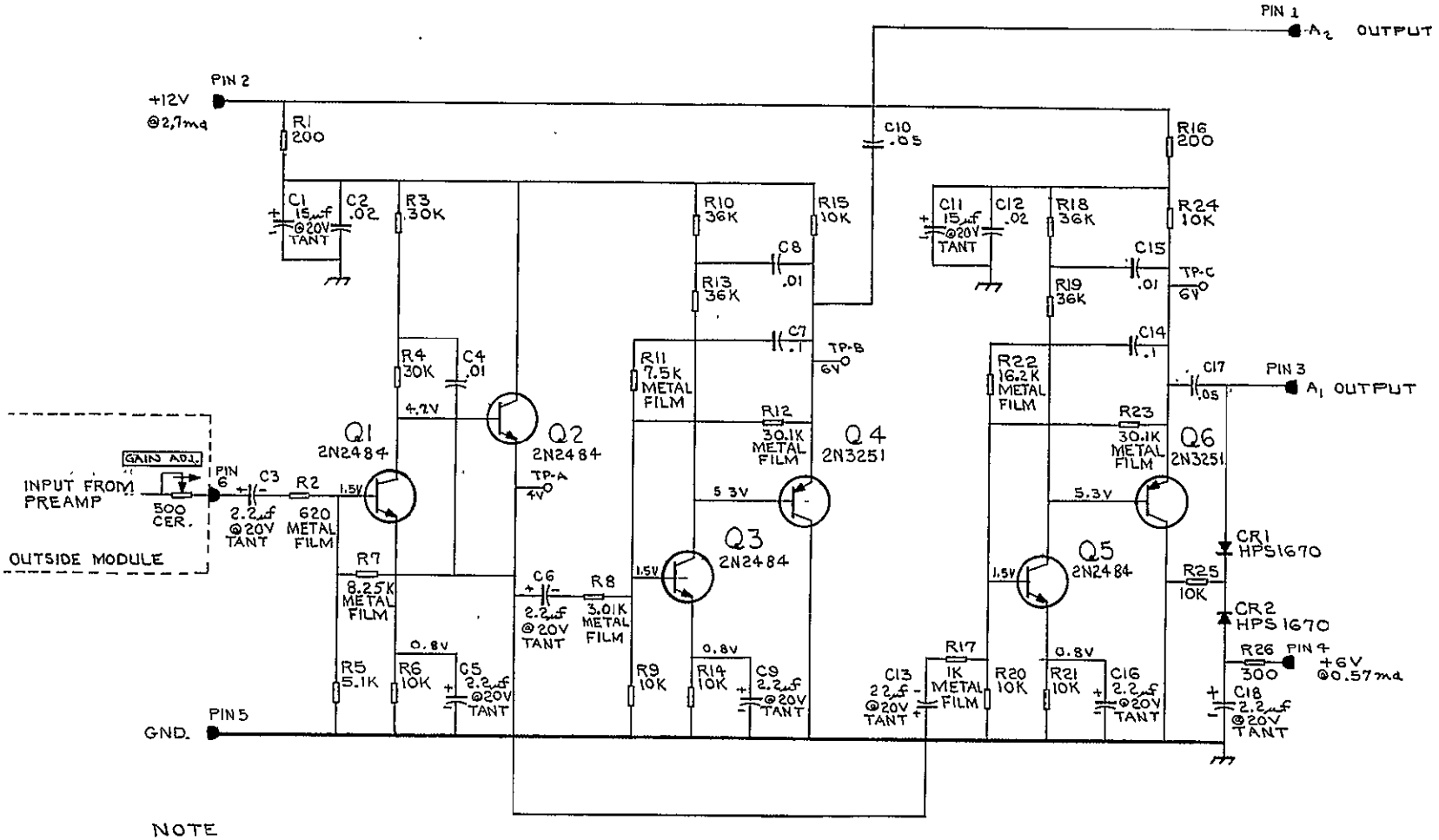

NOTE
1. GAIN OF AMPLIFIER A_1 = 100
2. GAIN OF AMPLIFIER A_2 = 20

Fig. 3-6. High-energy proton channels amplifier (LE 12854-81).

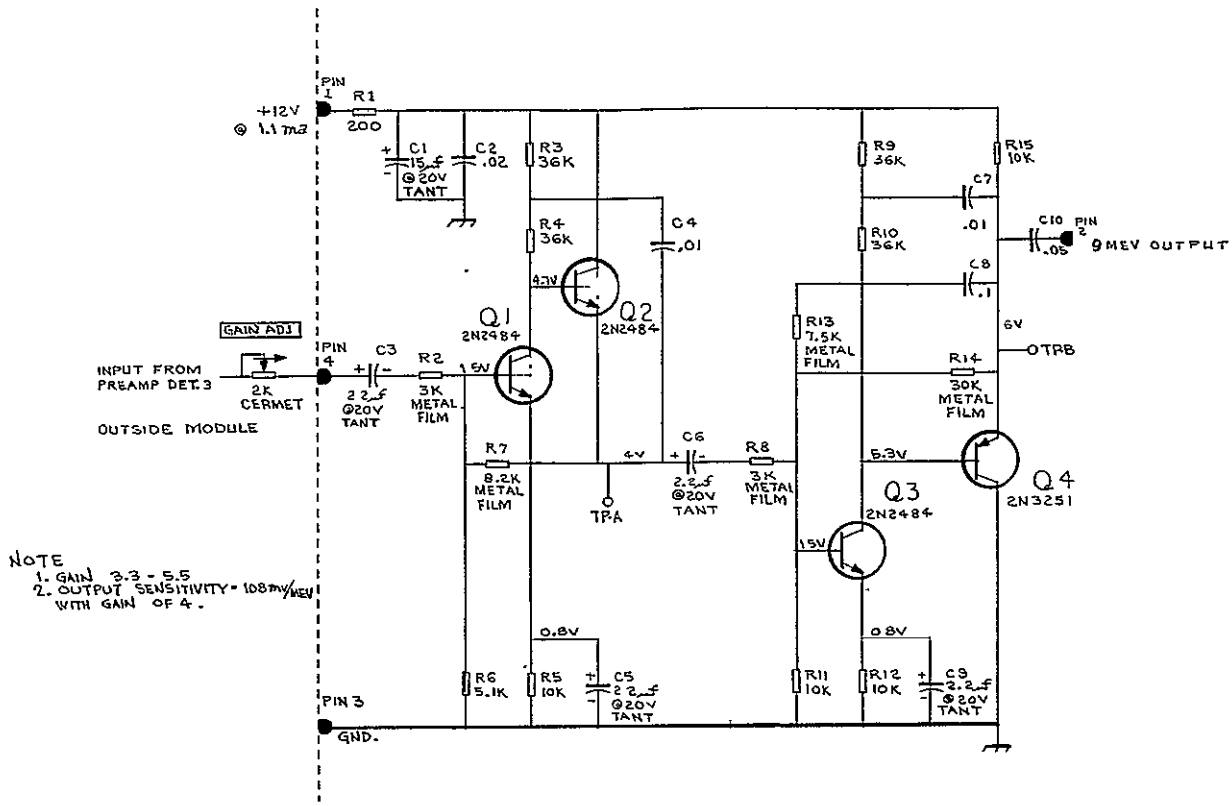

Fig. 3-7. Proton channel 9-MeV output detector 3 amplifier (LE 12854-151).

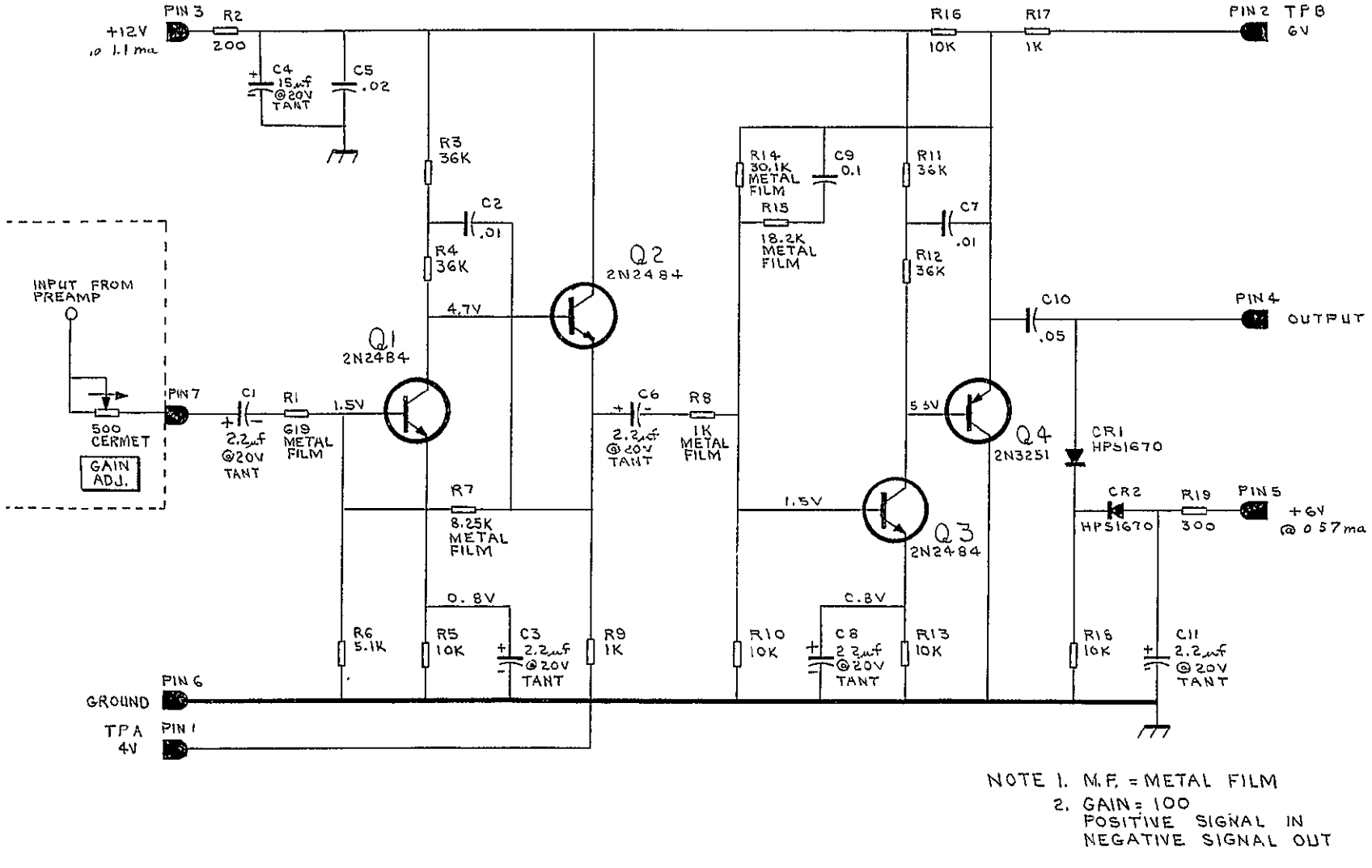

Fig. 3-8. Proton detector 4 amplifier (LE 12854-291).

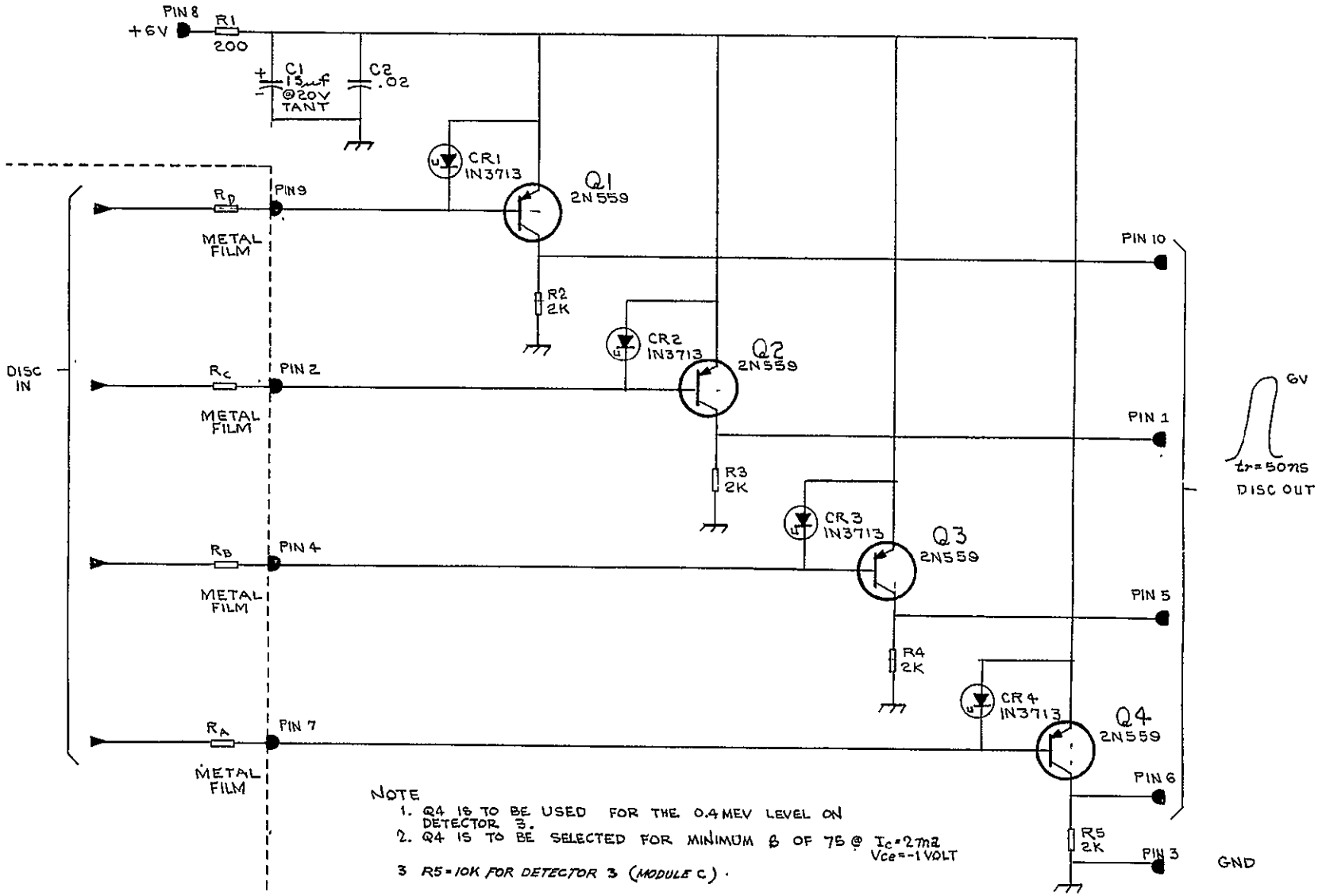

Fig. 3-9. Integral proton channels discriminator (LE 12854-91).

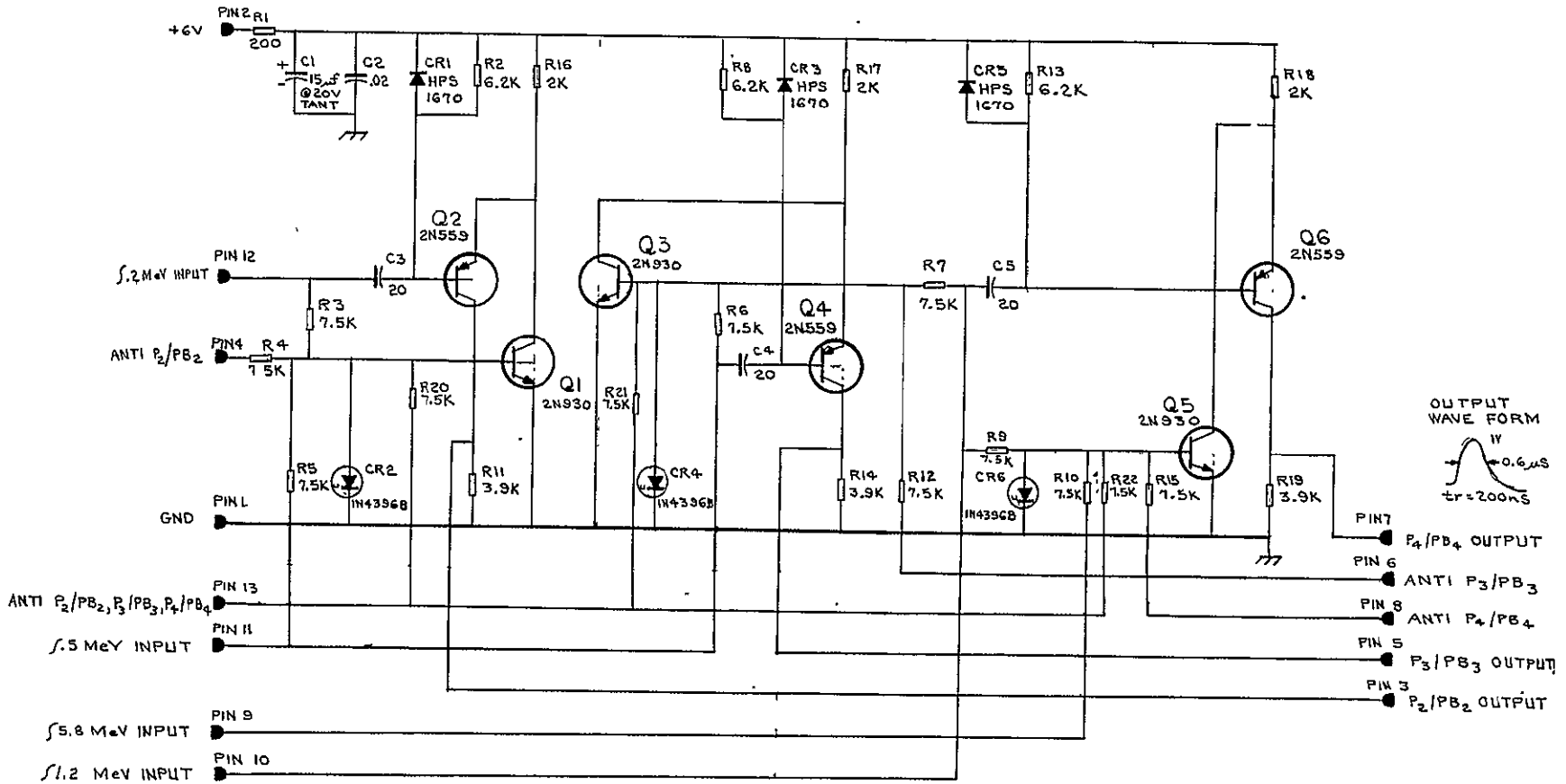

Fig. 3-10. Proton channels differential logic (LE 12854-101).

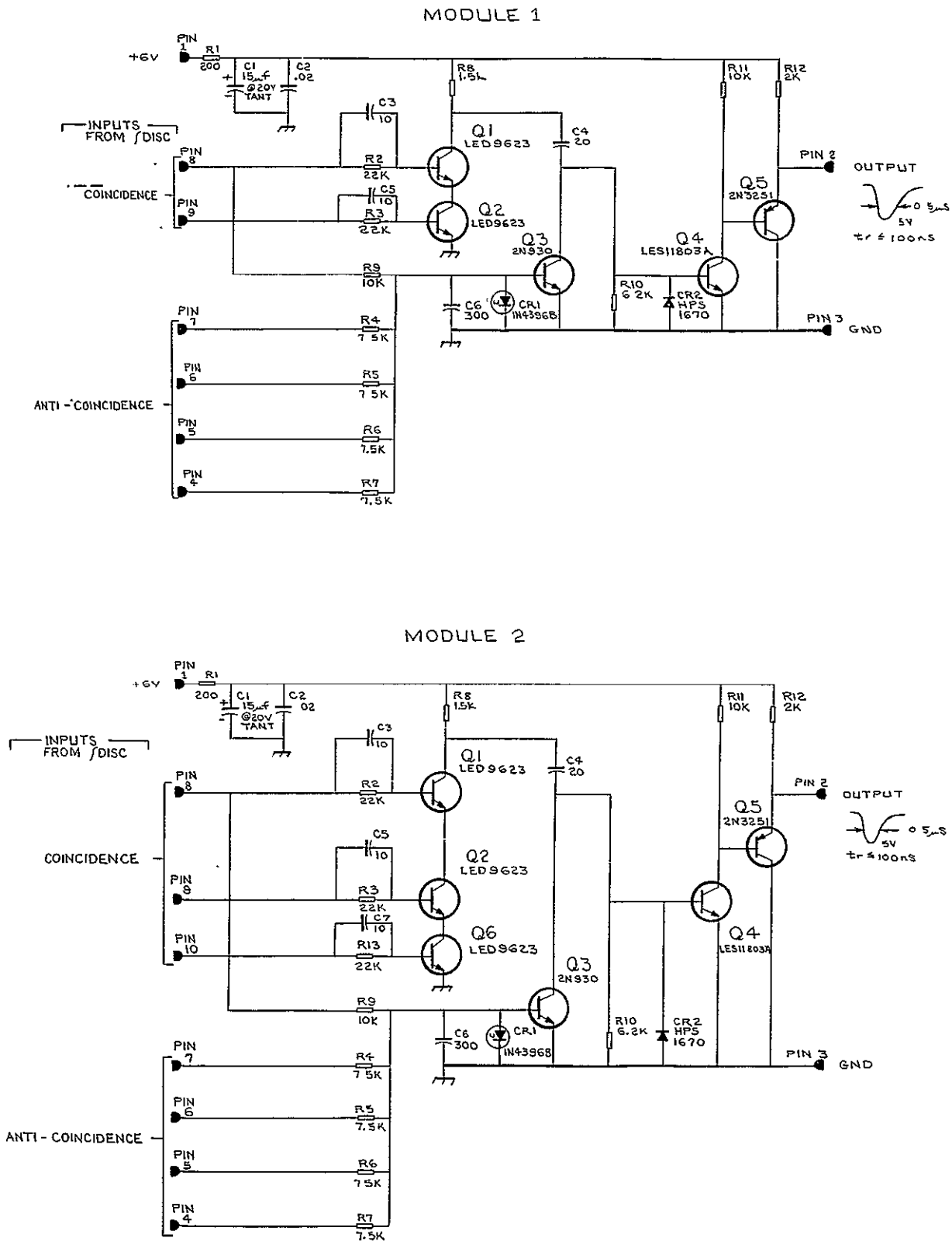

Fig. 3-11. Proton channels coincidence/anti-coincidence gate (LE 12854-121).

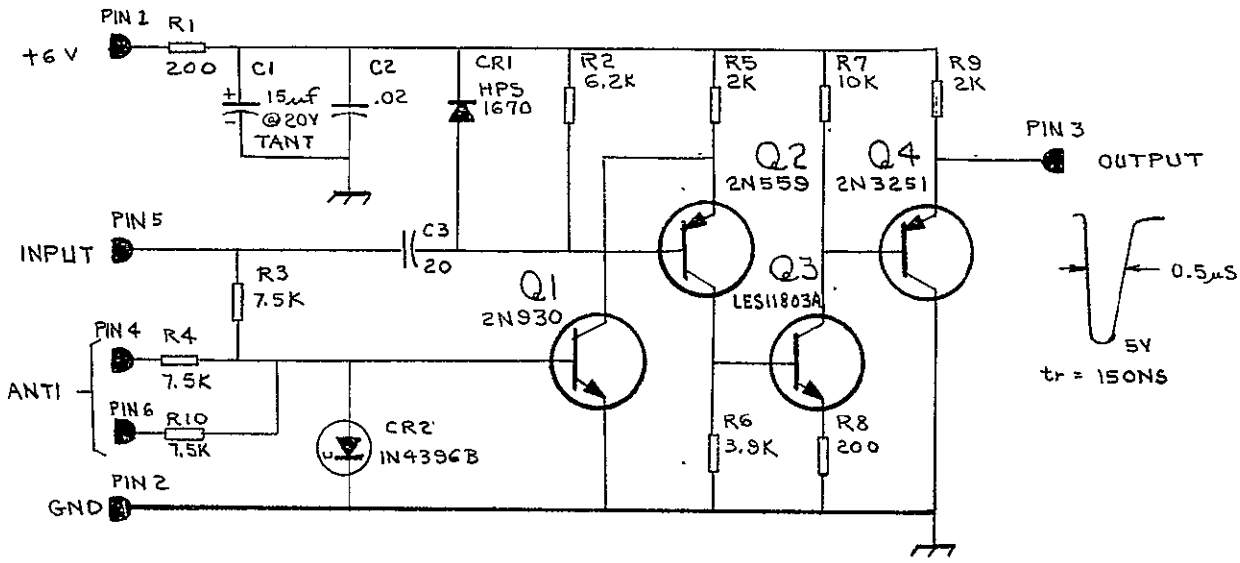

Fig. 3-12. Proton channels anti-coincidence gate (LE 12854-131).

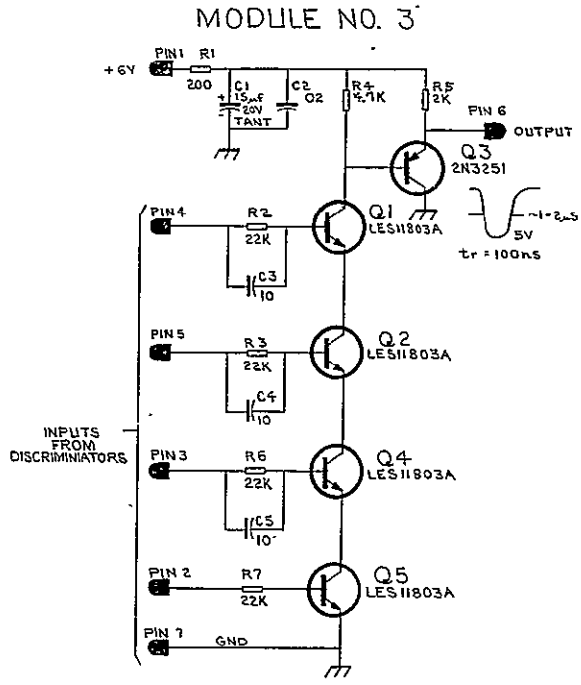

Fig. 3-13. Proton channels coincidence gate (LE 12854-141M3).

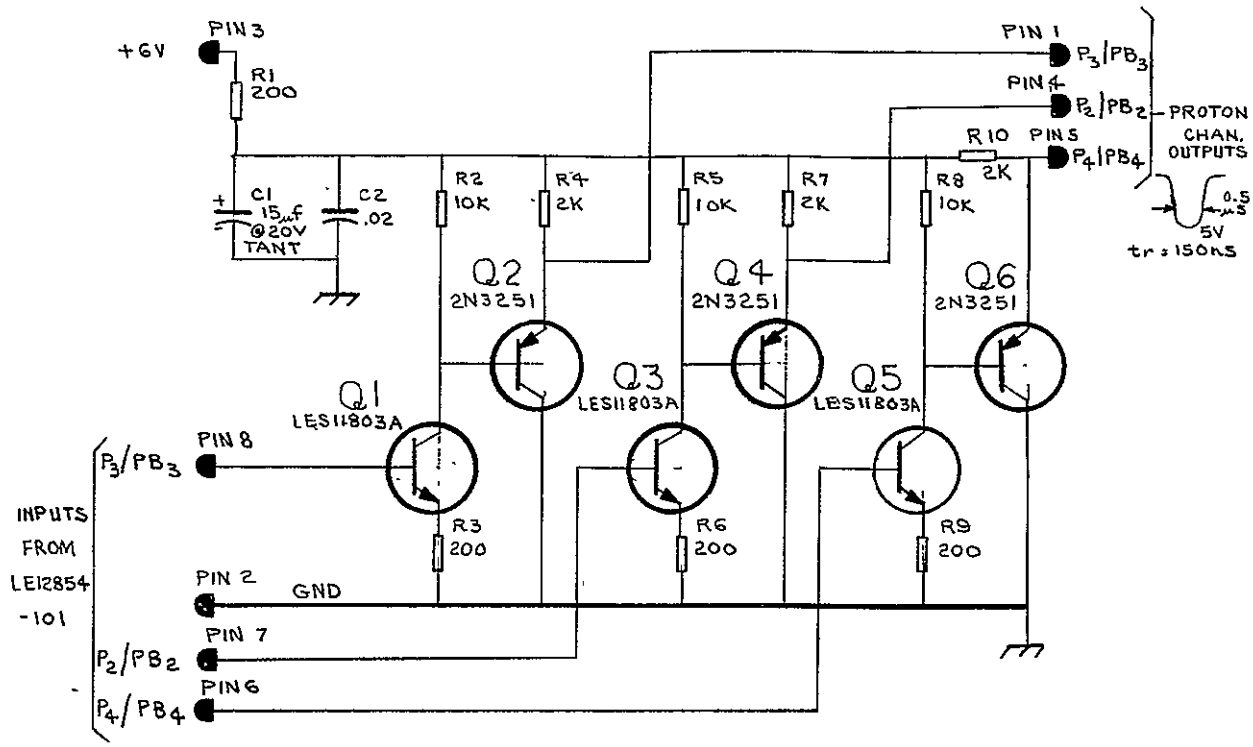

Fig. 3-14. Proton channels logic amplifier-driver (LE 12854-111).

4. Data Handling

4.1 INTRODUCTION

Figure 4-1 shows a block diagram of the experiment's data handling system. The interface with the spacecraft's data handling system is shown to the far left and right of the diagram. For completeness, we briefly describe the spacecraft's data handling system. For more detail the interested reader is referred to various NASA publications and specifications.[3]

OGO-V handles data primarily in a digital fashion. Analog data is acceptable, however, but is digitized into an 8-bit word prior to being accepted by the Digital Data Handling Assembly (DDHA). Two redundant DDHA's are provided in the spacecraft, called Equipment Groups 1 and 2 (EG_1 and EG_2). These are controlled by a central control system which determines the mode of operation of the DDHA's, e.g. which will be transmitting in "real time" and which will be tape recorded (both can go on simultaneously) or, if only one is in operation, which EG is handling data. Each EG is formated into 128, 9-bit words. This format is called the "main frame." Various words are relegated to spacecraft functions, three of which are further subcommutated by 128 words each to provide spacecraft and experiment status data.

The indication as to when the DDHA is ready to handle the data readout of a given word comes via the "inhibit" signals (I) from the two EG's, Fig. 4-2. Which EG is to receive data is determined by the "mode" and "switch" signals (SW), Fig. 4-3. This experiment is designed to output to real time whenever there is real-time transmission and to tape recorder otherwise. For this mode of operation, only the SW signal is needed. To provide data readout from the experiment, the spacecraft continuously provides shift pulses from the two EG's, the proper EG selected by SW. The shift pulses then cause the serial output of the experiment's shift register (SR), Fig. 4-4, as long as the appropriate I is present. Readout occurs at three rates: 1 kbit/sec, 8 kbits/sec, or 64 kbits/sec.

Out of the 128 words available on the main frame, this experiment is provided digital words 10, 27, 50, 89, 108, and analog word 55. In addition, the experiment uses analog word 102 in the No. 1 subcommutator as an indicator as to which of the experiment's two low voltage power supplies is in operation.

4.2 DATA ACCUMULATION

All counting data in the experiment is handled by flip-flop scalers or accumulators (ACC). The one analog word is used to provide the internal status of the experiment and to provide the synchronization internal to the experiment.

Associated with each digital word are four ACC's (see Figs. 4-1, 4-5, and 4-6. Appropriate gates at the inputs to the ACC's provide data routing. In all cases, data count for four frames of the DDHA. For data of secondary or tertiary importance, the data are counted one half the

[3] See Specification No. Revision D, D-13356-1, April 25, 1966, TRW Systems.

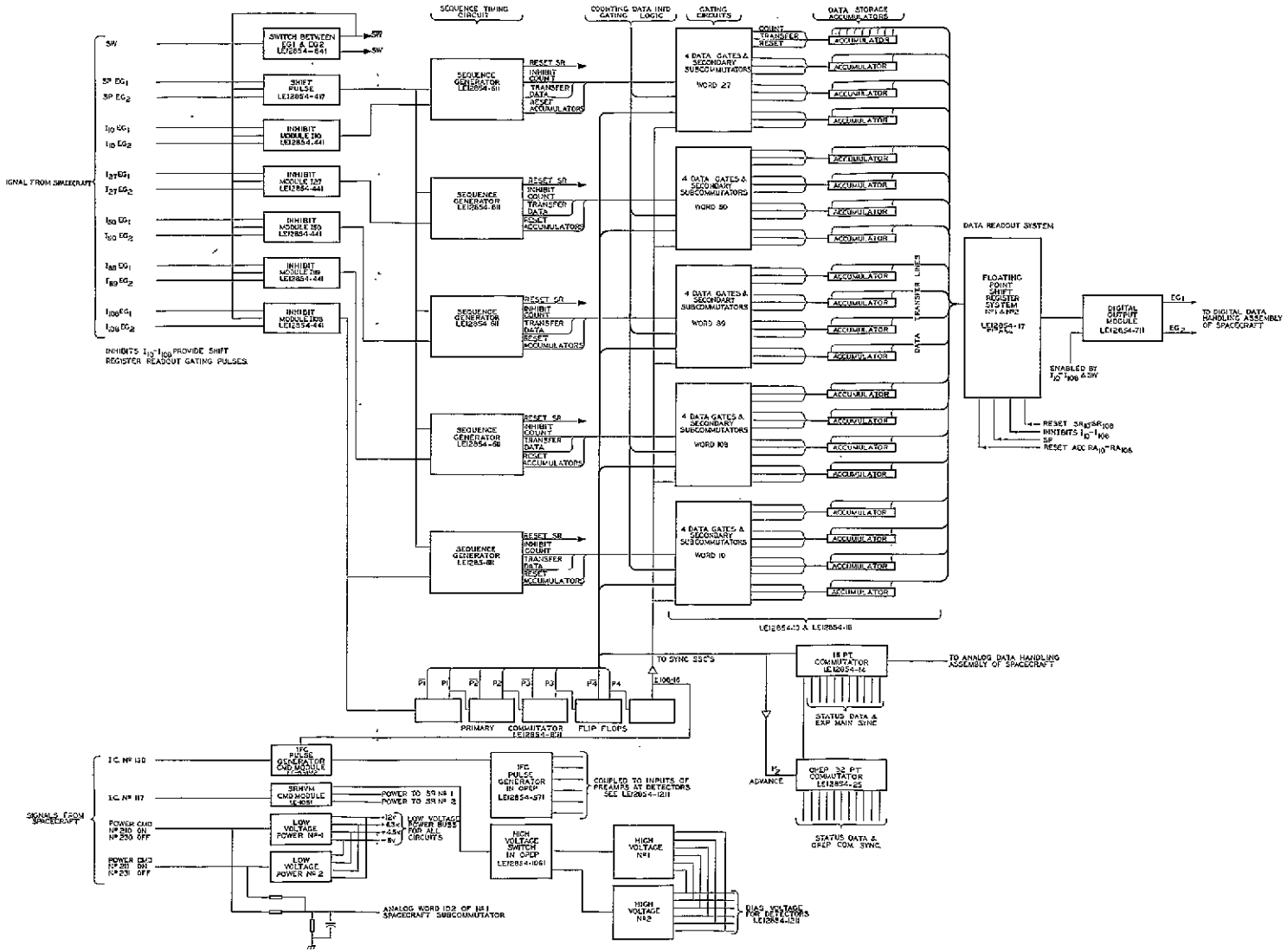

Fig. 4-1. Block diagram of data handling system (LE 12854-26).

FOLDOUT FRAME

FOLDOUT FRAME 2

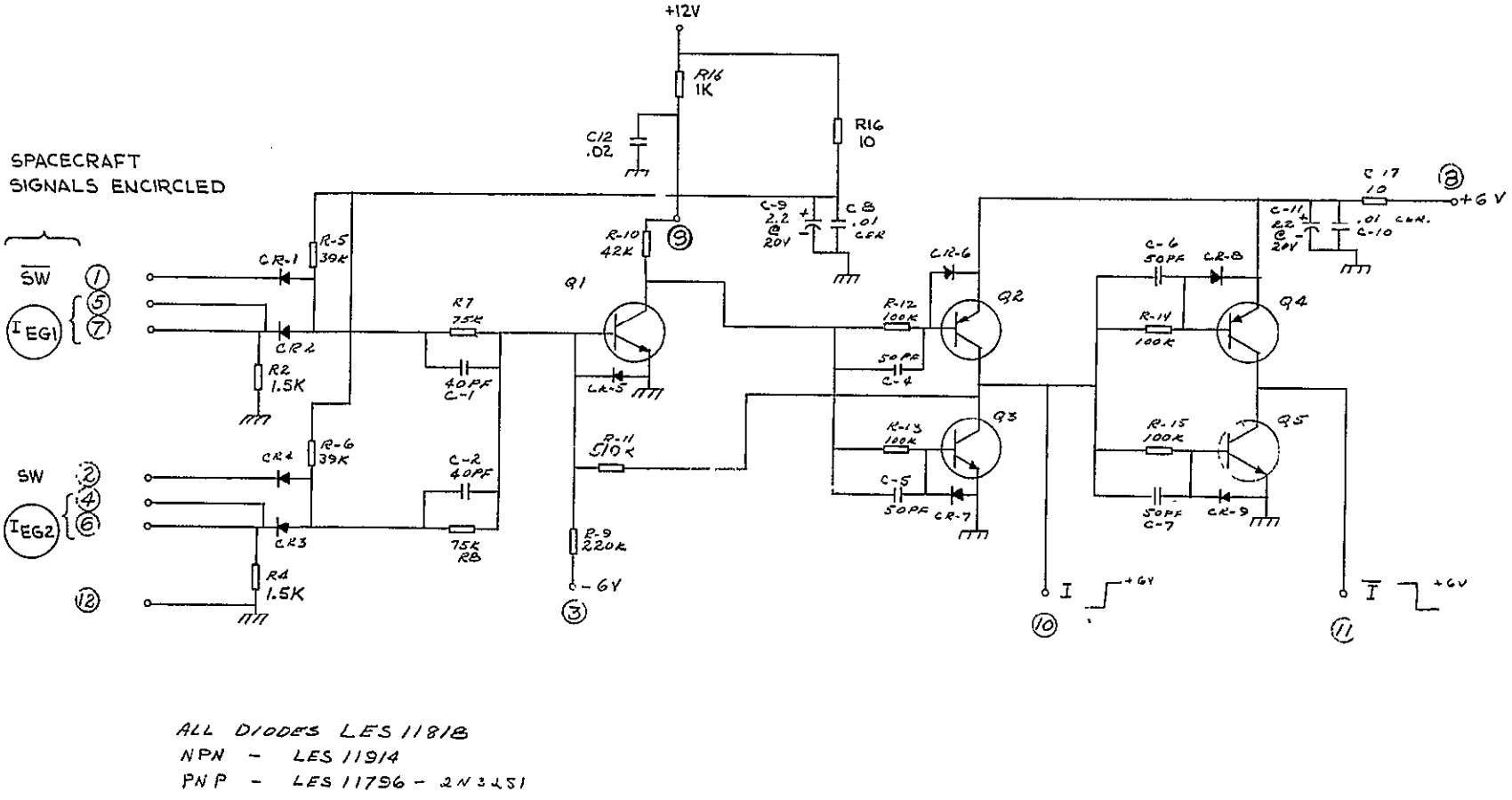

ALL DIODES LES 11818
NPN - LES 11914
PNP - LES 11796 - 2N3251

Fig. 4-2. Inhibit interface module (LE 12854-441).

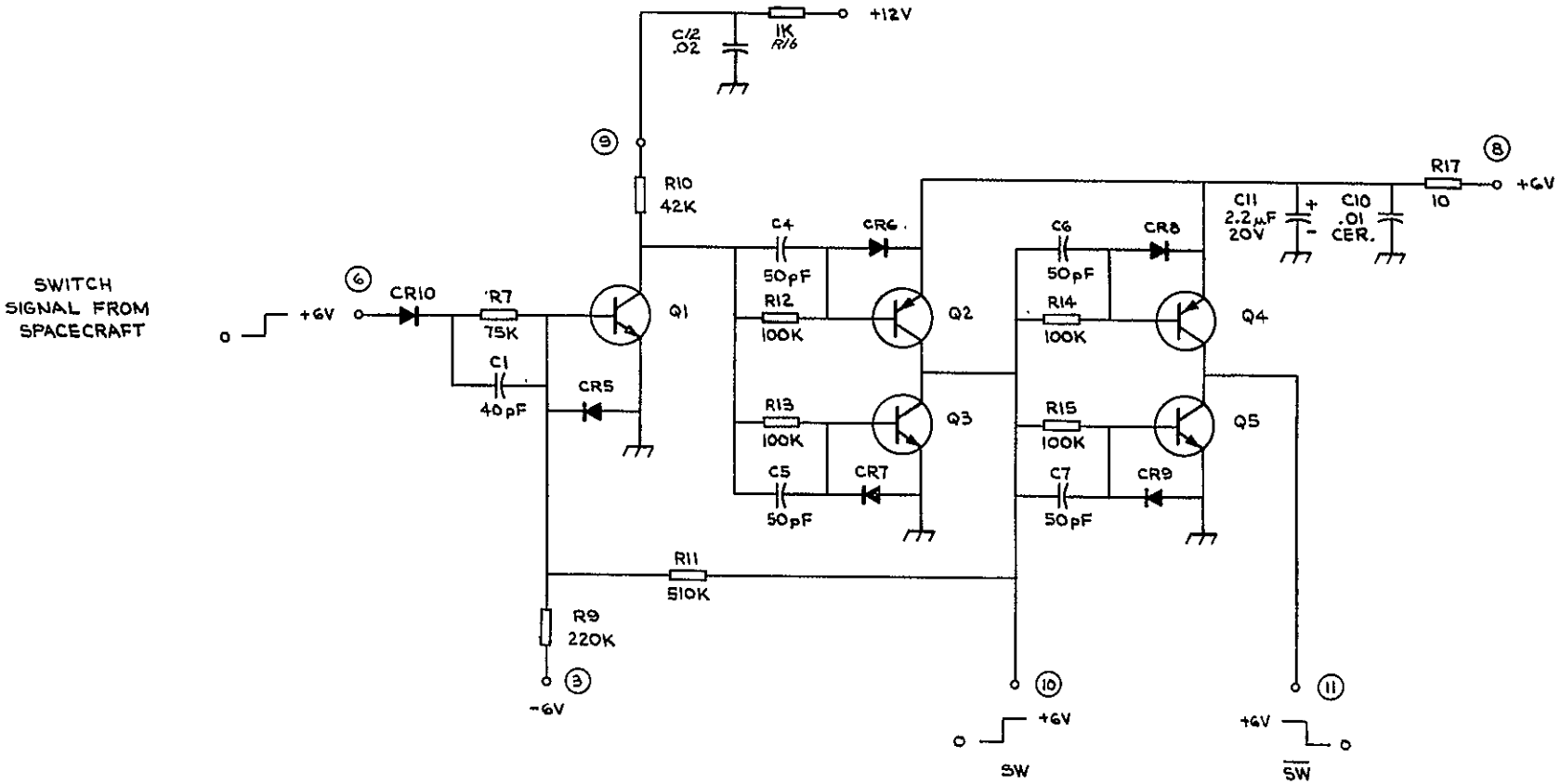

NOTE: (1) ALL DIODES ARE LES11818, ALL NPN TRANSISTORS ARE LES11914 AND ALL PNP TRANSISTORS ARE LES11796 (2N3251)

(3) THIS CIRCUIT IS SIMILAR TO LE12854-441. WHERE THE TWO CIRCUITS COINCIDE THE COMPONENT DESIGNATIONS ARE IDENTICAL.

Fig. 4-3. Switch interface module (LE 12854-841).

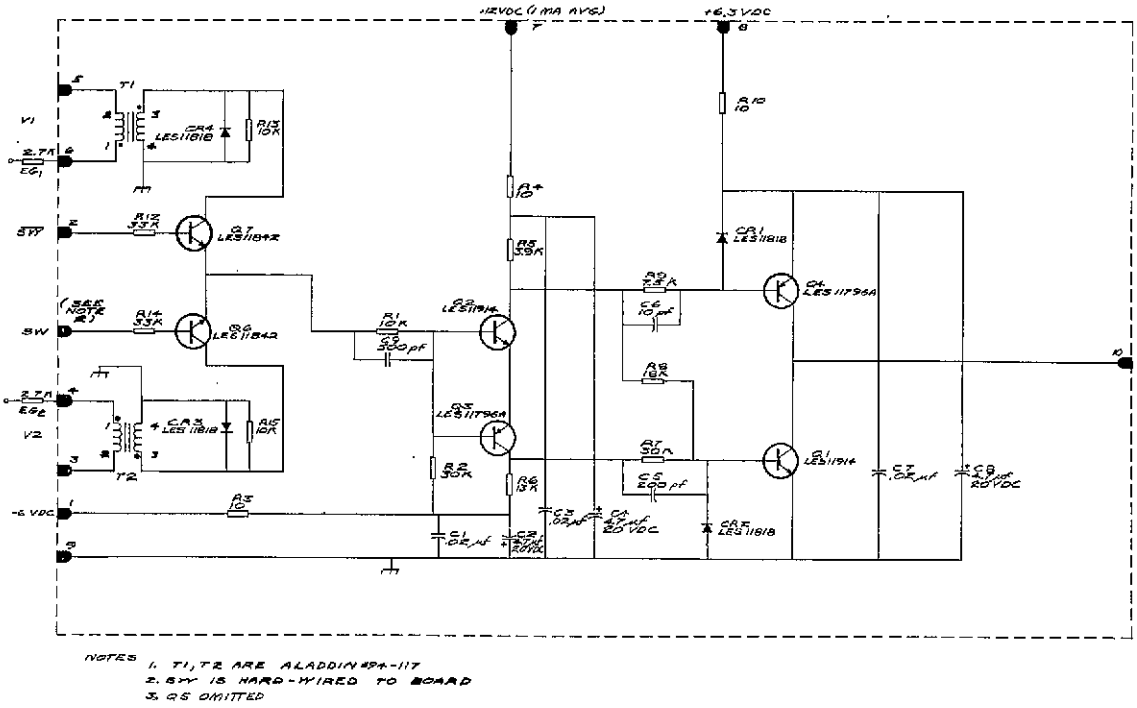

NOTES
1. T1, T2 ARE ALADDIN #94-117
2. SW IS HARD-WIRED TO BOARD
3. Q5 OMITTED

Fig. 4-4. Shift-pulse interface module (LE 12854-417).

ROUTING OF DATA INTO ACCUMULATORS

WORD	PRIMARY POSITION	STATE OF PRIMARY SUB COM FLIP-FLOPS		INPUT TO SECONDARY POSITION				BITS IN ACC
		P_a	P_b	S_1 S_2	$\overline{S_1}$ S_2	S_1 $\overline{S_2}$	$\overline{S_1}$ $\overline{S_2}$	
10	1	P_1	P_2	E_1				20
	2	$\overline{P_1}$	P_2	E_3				18
	3	P_2	$\overline{P_2}$	P_1				20
	4	$\overline{P_1}$	$\overline{P_2}$	E_{B1}	E_{B3}	E_{B5}	P_{B1}	16
27	1	P_1	P_2	E_5				16
	2	$\overline{P_1}$	P_2	P_5				16
	3	P_2	$\overline{P_2}$	O_2	P_7			16
	4	$\overline{P_1}$	$\overline{P_2}$	$\alpha B2$	$\alpha 2$	$\alpha 3$	$\alpha B3$	10
50	1	P_1	P_2	E_2				20
	2	$\overline{P_1}$	P_2	P_2				16
	3	P_1	$\overline{P_2}$	O_2	E_8			16
	4	$\overline{P_1}$	$\overline{P_2}$	E_{B2}	E_{B6}	P_{B2}	P_{B5}	18
89	1	P_1	P_2	E_6				16
	2	$\overline{P_1}$	P_2	P_6				16
	3	P_1	$\overline{P_2}$	P_3				18
	4	$\overline{P_1}$	$\overline{P_2}$	α_1	PB6	α_1	α_{B1}	10
108	1	P_1	P_2	P_4				18
	2	$\overline{P_1}$	P_2	E_7				16
	3	P_1	$\overline{P_2}$	E_4				18
	4	$\overline{P_1}$	$\overline{P_2}$	EB4	EB7	PB3	PB4	12

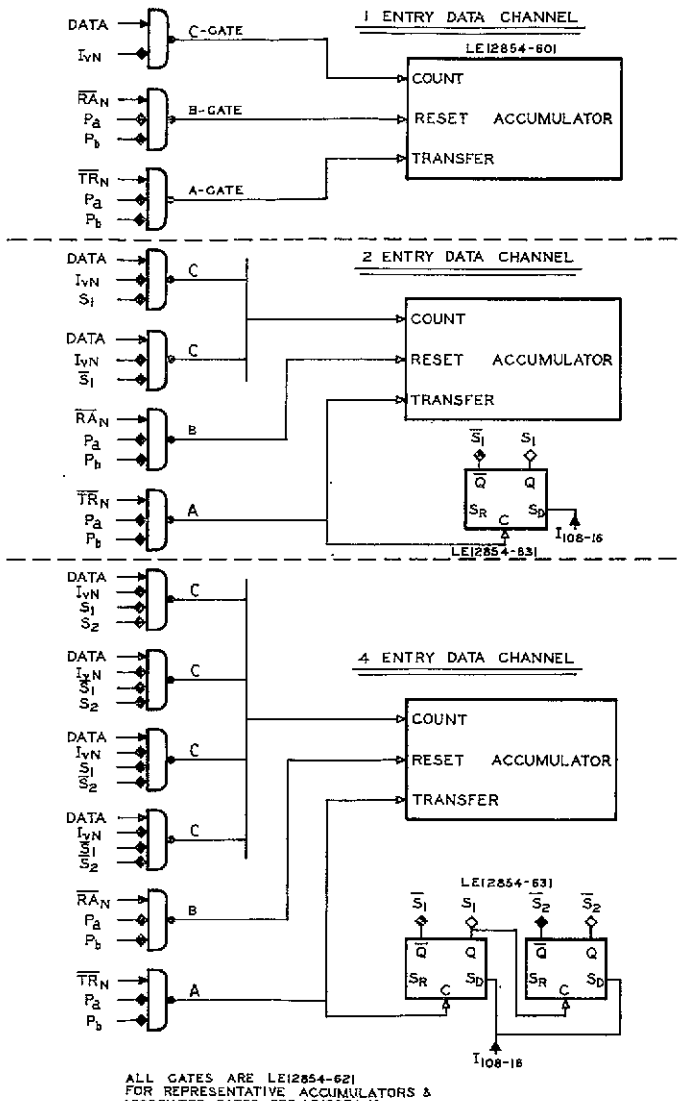

Fig. 4-5. Data acquisition logic (LE 12854-10).

FOLDOUT FRAME 1

FOLDOUT FRAME 2

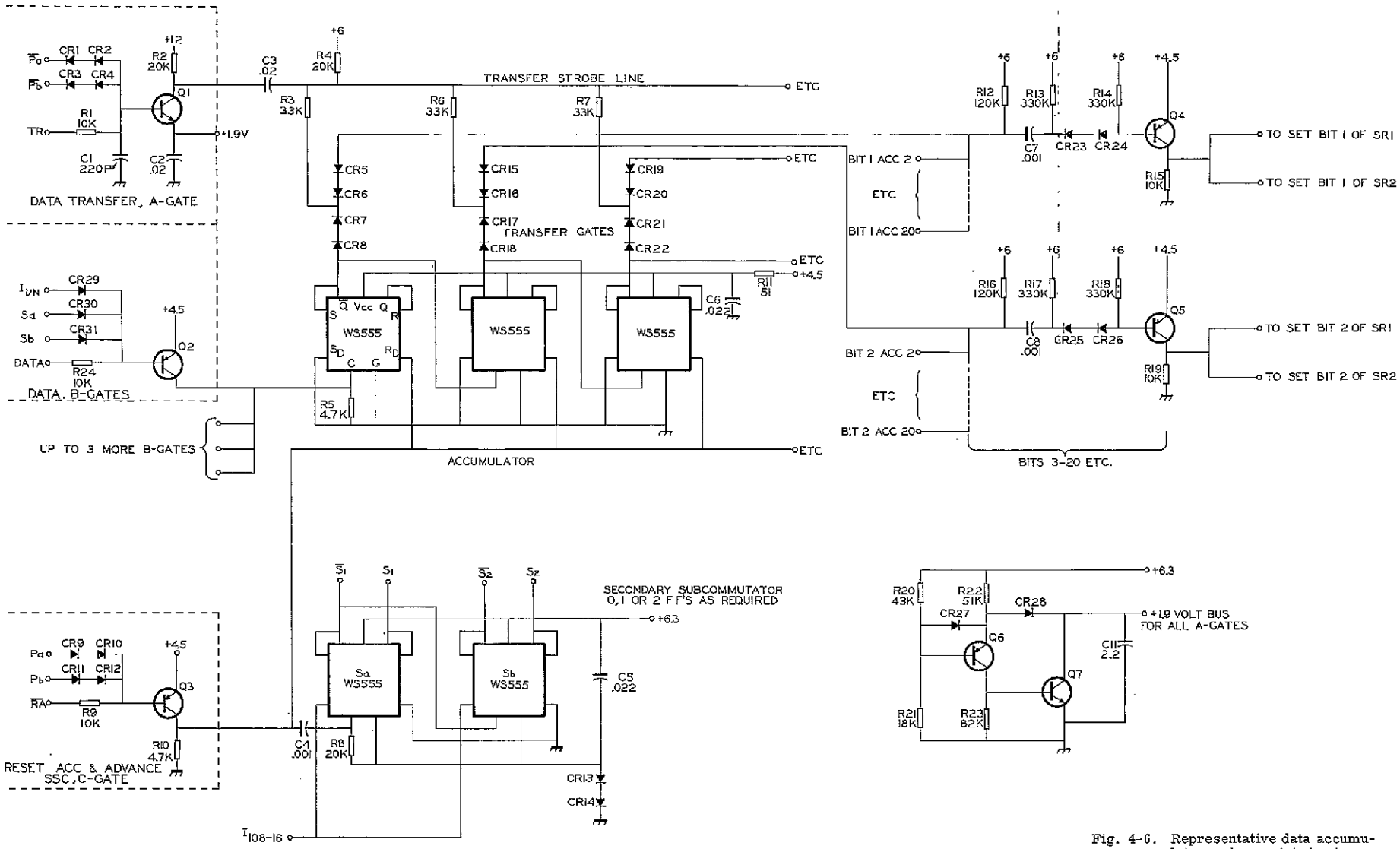

FOLDOUT FRAME 1

FOLDOUT FRAME 2

Fig. 4-6. Representative data accumulator and associated gates (LE 12854-16).

time or one fourth of the time. The basic commutation cycle internal to the experiment is 16 frames of the DDHA. This is provided by the commutator flip-flops P_1 through P_4 (Fig. 4-7). Advancement of the primary commutator is provided by the trailing edge of pulse $\overline{I}_{108}$. The primary commutator will do an adequate job of sequencing the readout of each of the four ACC's common to a given data word; but additional subcommutating is necessary to control the counting into a given ACC in the event it is to handle two or more data inputs. This secondary subcommutation (SSC) is provided by one or two flip-flops (Fig. 4-6) common only to the given ACC and its associated gates. They must be common to the one ACC only, because the updating of the SSC must occur at the time of data transfer from the respective ACC, and this time is not common to any other ACC. However, to keep the SSC's in step, it is necessary to periodically provide a sync pulse. This is done via the pulse called $I_{108\text{-}16}$ (Figs. 4-6 and 4-7). This pulse assures that all the SSC flip-flops are in the "set" condition at the start of a commutation cycle.

Table 4-1 shows the sequence in which the data comes up in readout. The synchronization of the format is provided by SYNC in word A 55 (a 11111111 in binary notation). The details of the analog output will be discussed later.

A binary floating point compression system reads the data from the 12 to 20 bits of the ACC's into the 9-bit word of the DDHA. This system requires set-up time prior to readout from the experiment. The timing of these operations starts at the trailing edge of the previous "inhibit", called I_{N-1}. The operations are controlled by the sequence generators, Fig. 4-8, one of which is common to each data word. The sequence of operations is as follows:

(1) Reset the shift register system via $\overline{RS}_N$.
(2) Inhibit data count in all four ACC's of the data word via $I_{\nu N}$.
(3) Transfer the data from the ACC to the shift register via $\overline{TR}_N$. Advance the SSC, if used with the ACC, via $\overline{TR}_N$.
(4) Reset the ACC via $\overline{RA}_N$.
(5) Start data "setup" in the shift register via $\overline{RA}_N$.
(6) Restart the data counts.

4.3 FLOATING-POINT SHIFT REGISTER SYSTEM

Figure 4-9 shows a block diagram of the system. The associated circuits are as follows:

- reset accumulator, Fig. 4-10;
- enable shift register, Fig. 4-11;
- reset shift register, Fig. 4-12;
- floating point SR, Fig. 4-13; and
- digital output gates, Fig. 4-14.

Our goal is to read out the most significant 5 bits of data and where they are located in the scalar chain. It is assumed that data from an accumulator has been transferred to bits 1 through 20 of the SR and that the control toggle has been set via $\overline{RA}_N$. The sequence of operations for data setup is then:

(1) Shift right in the SR.
(2) Count the number of shift pulses via the tally counter.
(3) When either bit 21 of SR is set or bit 4 of the tally counter is set, reset the toggle and stop the data shift.

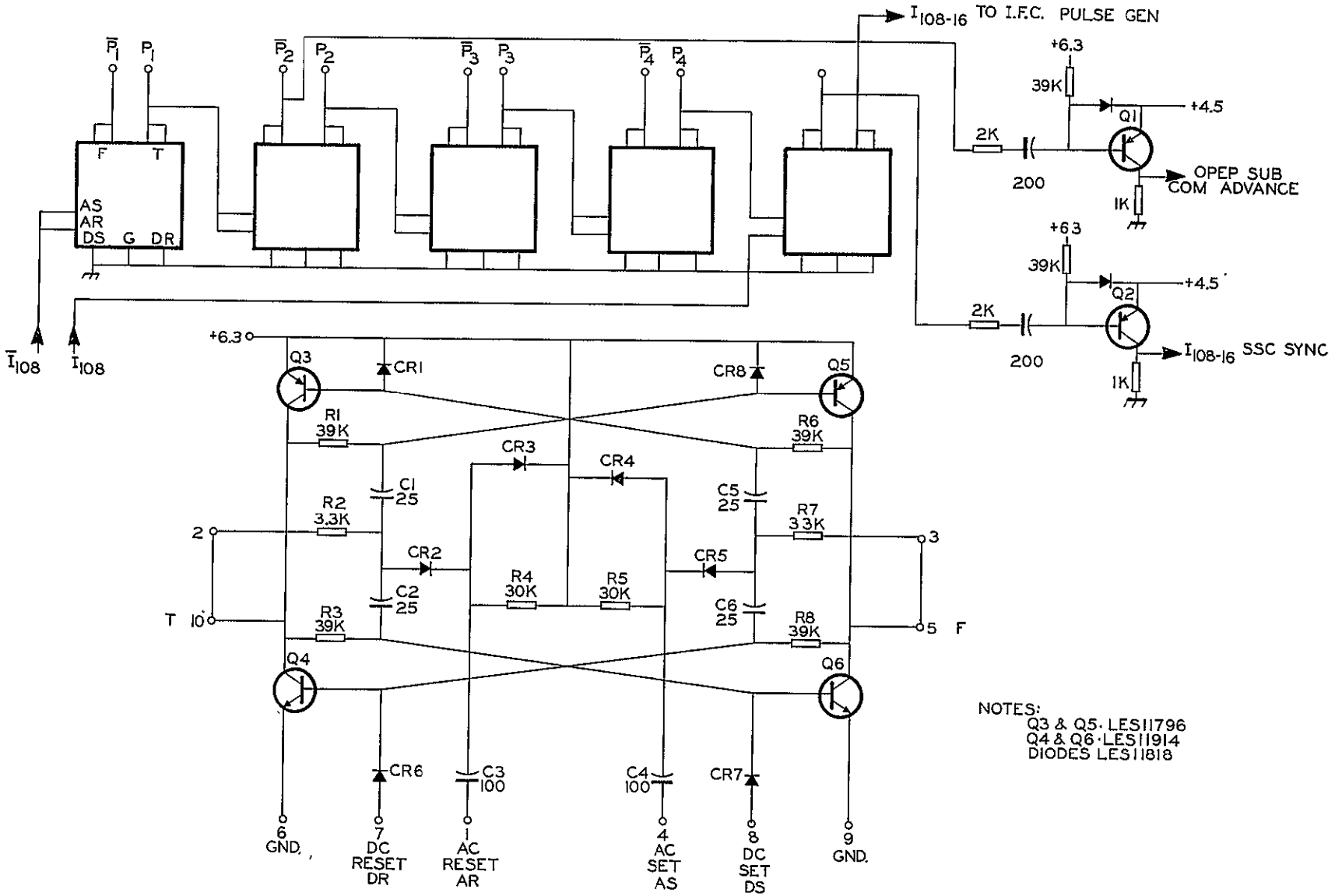

Fig. 4-7. Primary commutator (LE 12854-851).

Table 4-1. Main body package commutation sequence.

	Word					
Main Frame	D 10	D 27	D 50	A 55	D 89	D 108
1	E_1	E_5	E_2	PG	E_6	P_4
2	E_3	P_5	P_2	EG	P_6	E_7
3	P_1	O_2	O_1	OPEP	P_3	E_4
4	P_{B_1}	α_{B_2}	P_{B_5}	SRHVM	α_{B_1}	E_{B_4}
5	E_1	E_5	E_2	1.9 V	E_6	P_4
6	E_3	P_5	P_2	MBT	P_6	E_7
7	P_1	P_7	E_8	OPEP	P_3	E_4
8	E_{B_1}	α_3	E_{B_2}	PG	α_1	P_{B_4}
9	E_1	E_5	E_2	4.5 V	E_6	P_4
10	E_3	P_5	P_2	12 V	P_6	E_7
11	P_1	O_2	O_1	OPEP	P_3	E_4
12	E_{B_3}	α_{B_3}	E_{B_6}	6.3 V	P_{B_6}	P_{B_3}
13	E_1	E_5	E_2	-6.0 V	E_6	P_4
14	E_3	P_5	P_2	Ground	P_6	E_7
15	P_1	P_7	E_8	OPEP	P_3	E_4
16	E_{B_5}	α_2	P_{B_2}	SYNC	α_1	E_{B_7}

(4) Transfer the data from the tally counter to bits 22-25 of the SR to complete the data setup.

Readout occurs when I_N enables the ystem as follows:

(1) Enable shift pulses via I_N. Enable Digital Output Gates and Drivers via I_N, the proper EG is selected by SW and $\overline{SW}$.

(2) Shift 9 bits of data out of the SR noting that the contents of bit 21 may or may not be part of the data readout. Usually we know if bit 21 was set or not by the contents of the Tally Counter and there is no need to read out bit 21, hence the data shift is steered around bit 21 except when the tally counter has filled. Here, there is an ambiguity since bit 21 can be set, and hence we must read out this bit if we are to remove the ambiguity. This operation is controlled by flip-flop No. 5 of the tally counter.

Since the shift register system is a crucial part of the experiment, and redundancy could be supplied without undue complexity, a redundant unit is provided. The one in use is controlled by ground command.

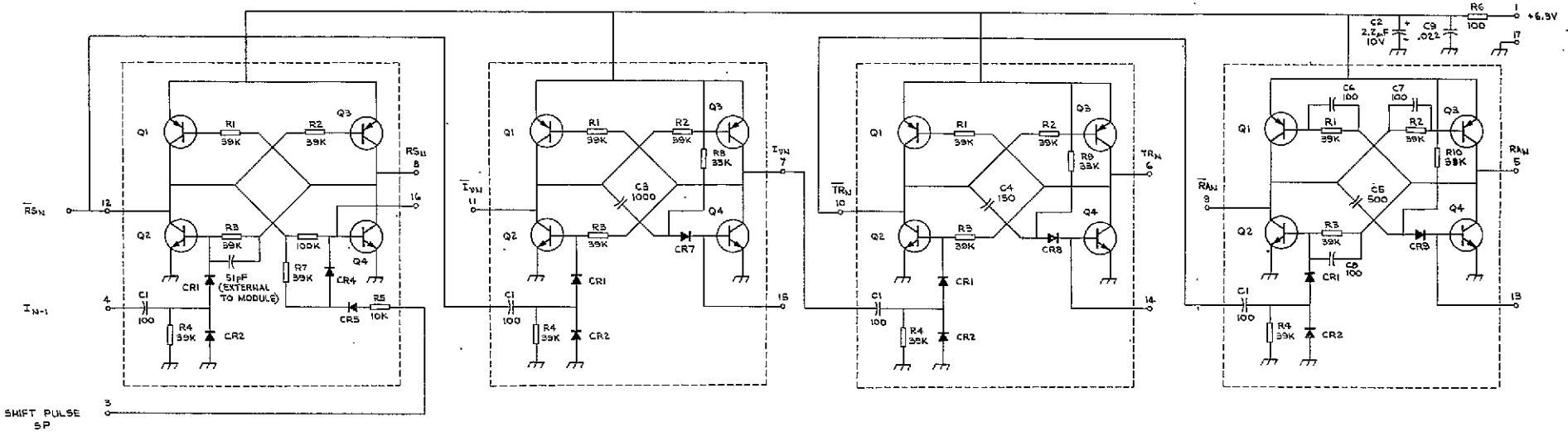

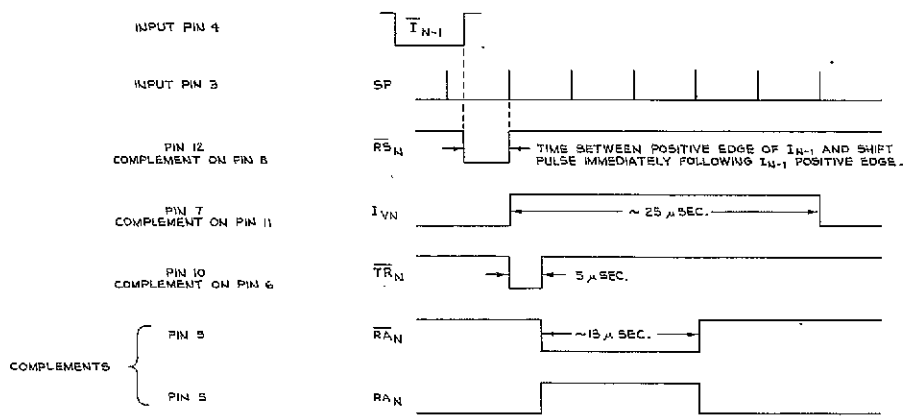

INDEX

SHIFT PULSES

RESET SHIFT REGISTER

INHIBIT COUNT IN ALL FOUR ACCUMULATORS OF WORD N

TRANSFER DATA FROM SELECTED ACCUMULATORS OF WORD N

RESET ACCUMULATOR

ENABLE START OF DATA SETUP IN SR

NOTE:
1. ALL NPN TRANSISTORS ARE LES 11914.
2. ALL PNP TRANSISTORS ARE LES11796.
3. ALL DIODES ARE LES 11818.
4. COMPONENTS WITHOUT ALPHANUMERIC IDENTIFICATION ARE EXTERNAL TO WELDED MODULE.
5. CR3 REMOVED.

Fig. 4-8. Sequence generator (LE 12854-611).

FOLDOUT FRAME 1

FOLDOUT FRAME 2

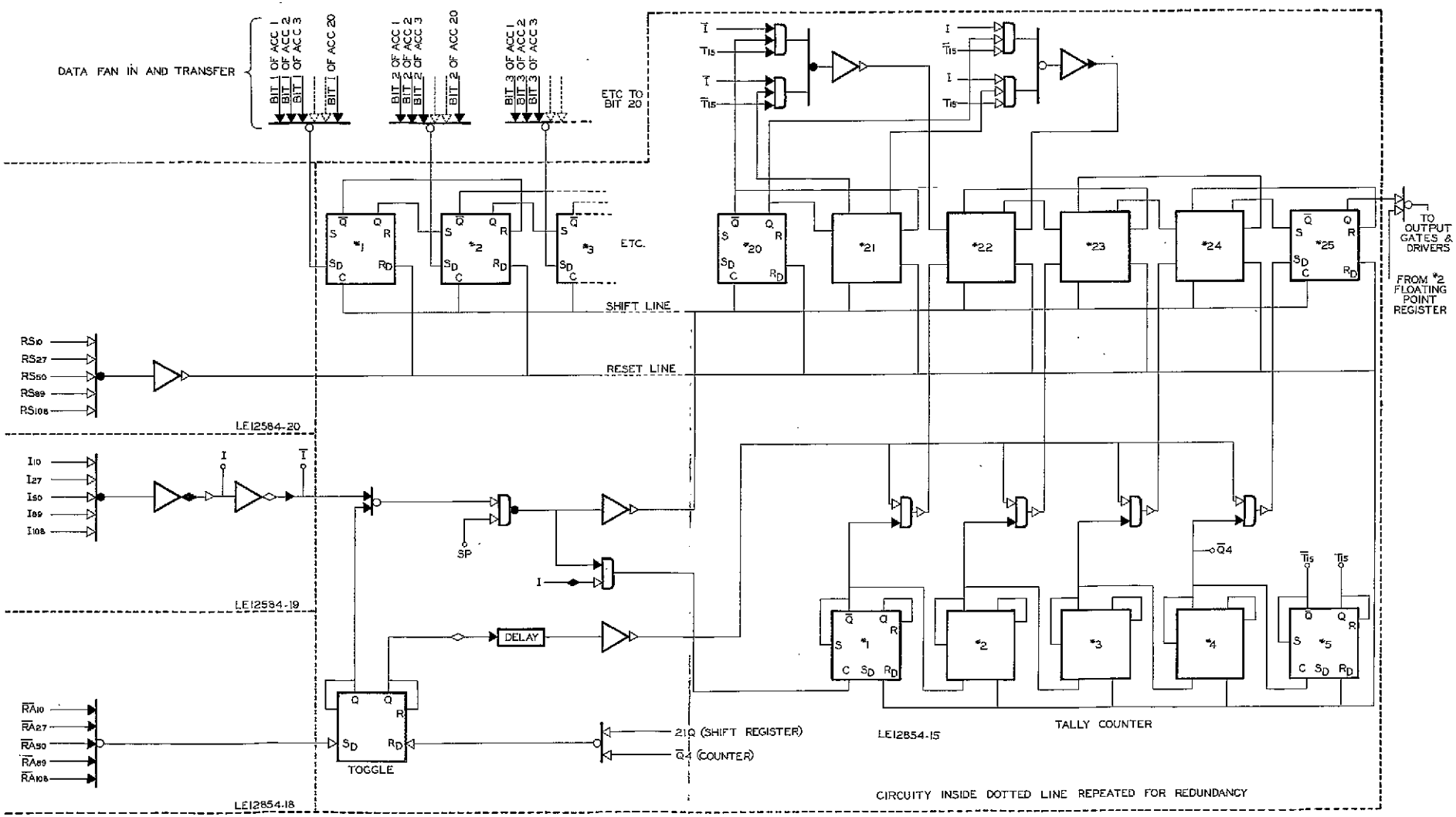

Fig. 4-9. Logic diagram of the floating-point shift register system (LE 12854-17).

FOLDOUT FRAME 1

FOLDOUT FRAME 2

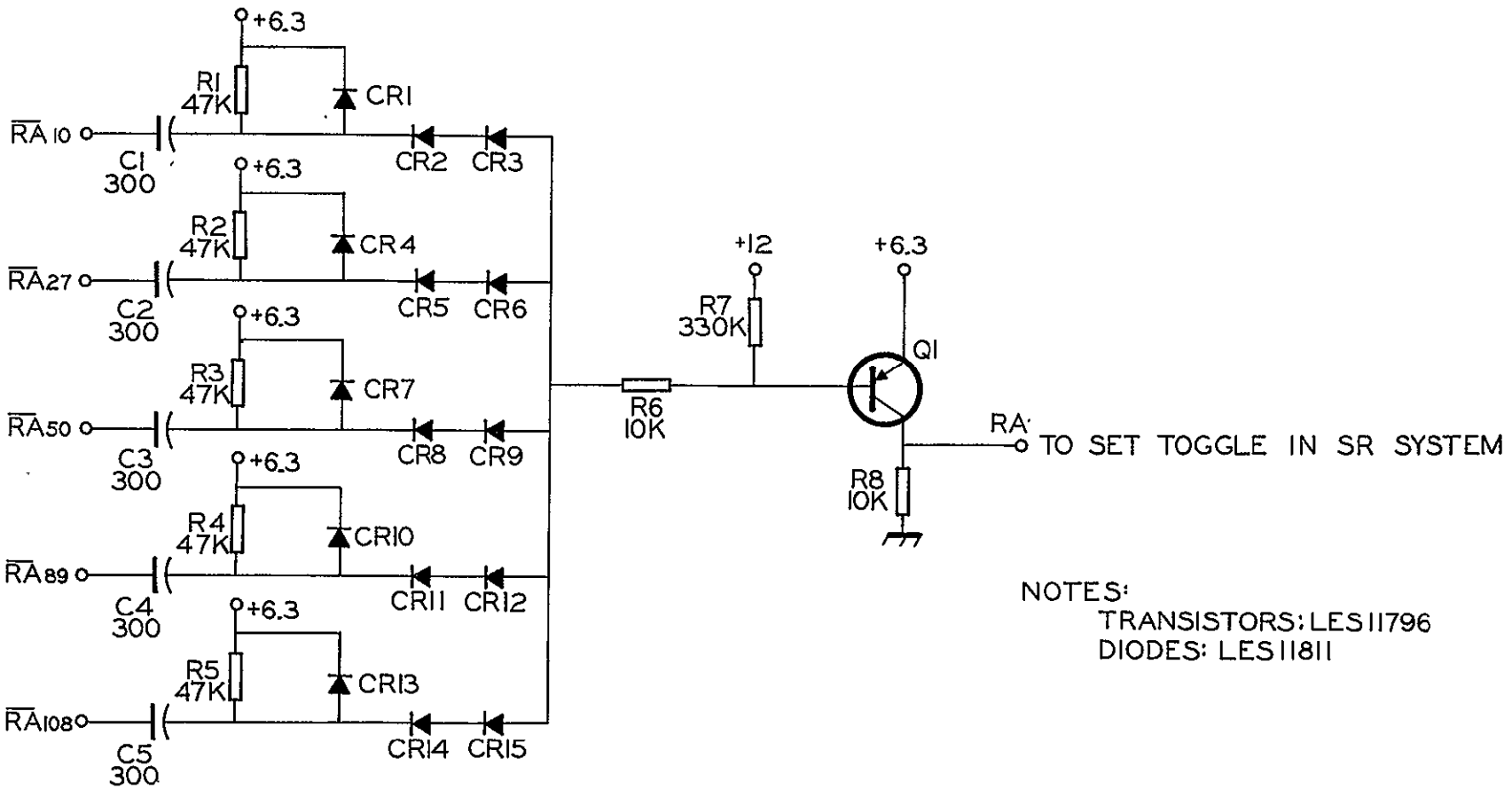

Fig. 4-10. Enable SR setup (LE 12854-18).

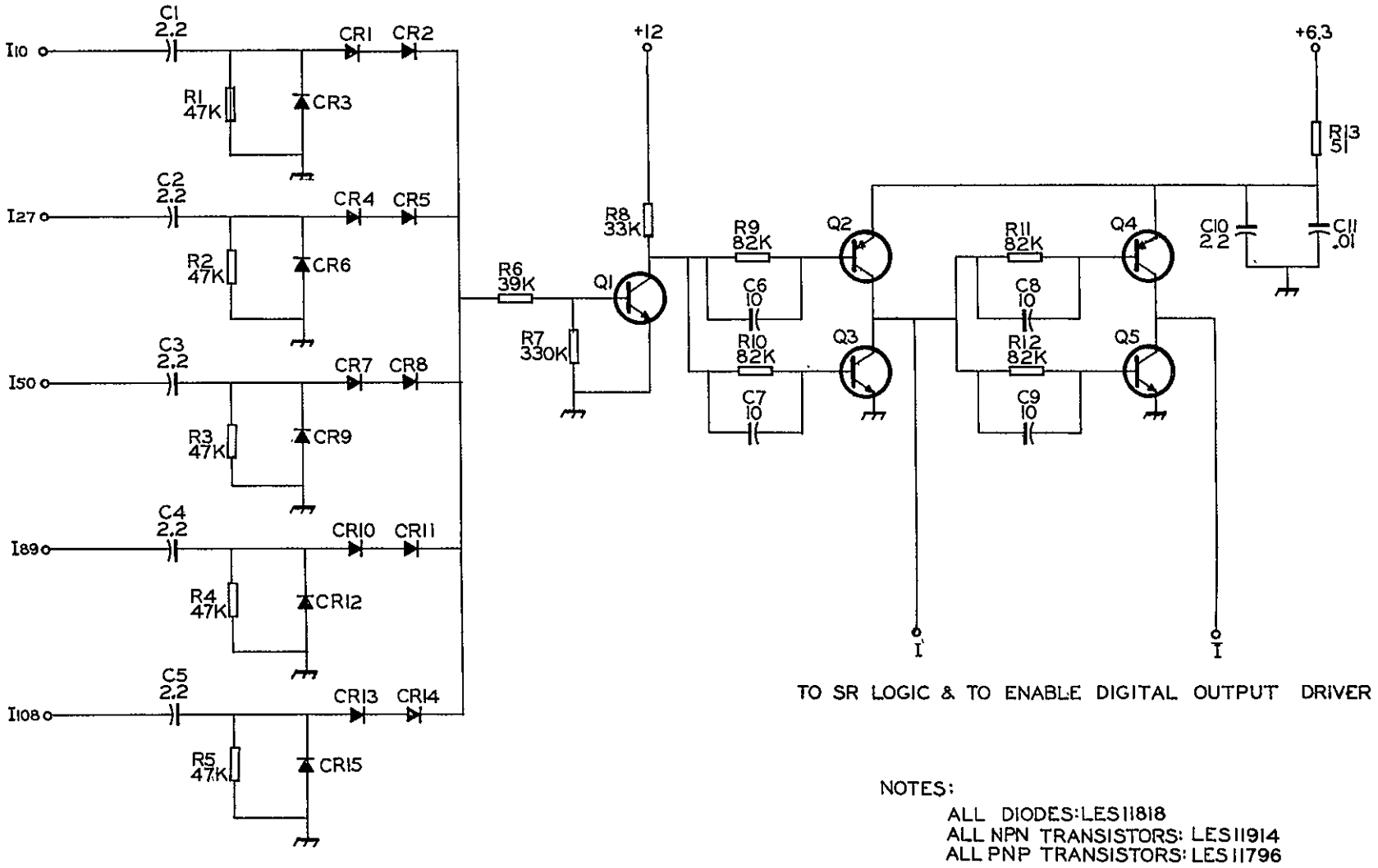

Fig. 4-11. Readout SR enable (LE 12854-19).

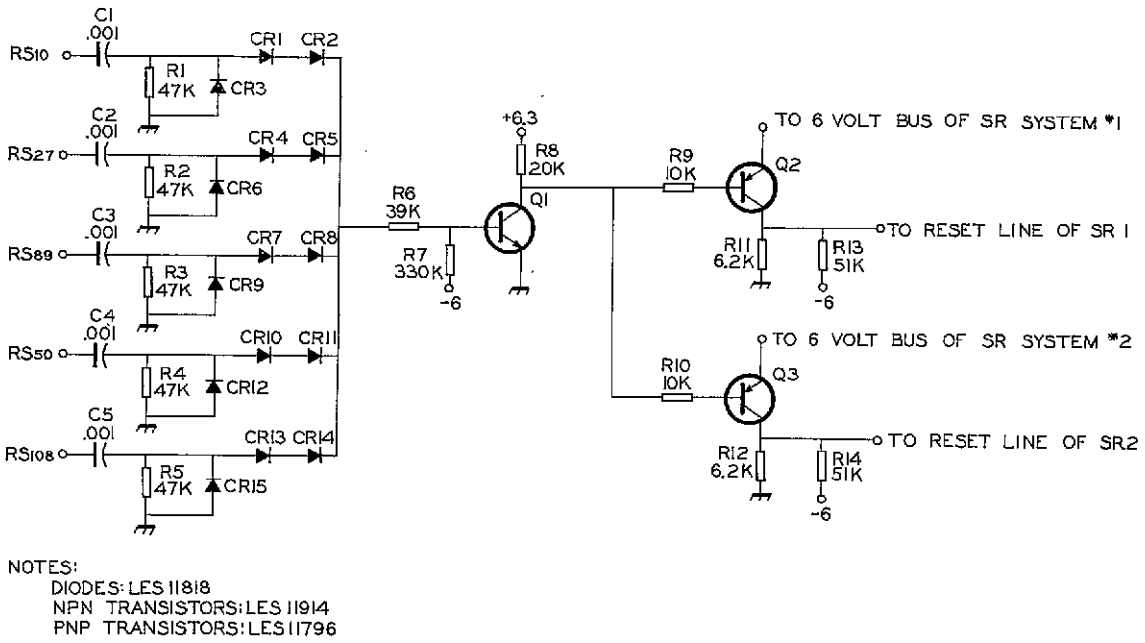

NOTES:
DIODES: LES 11818
NPN TRANSISTORS: LES 11914
PNP TRANSISTORS: LES 11796

Fig. 4-12. Reset SR (LE 12854-20).

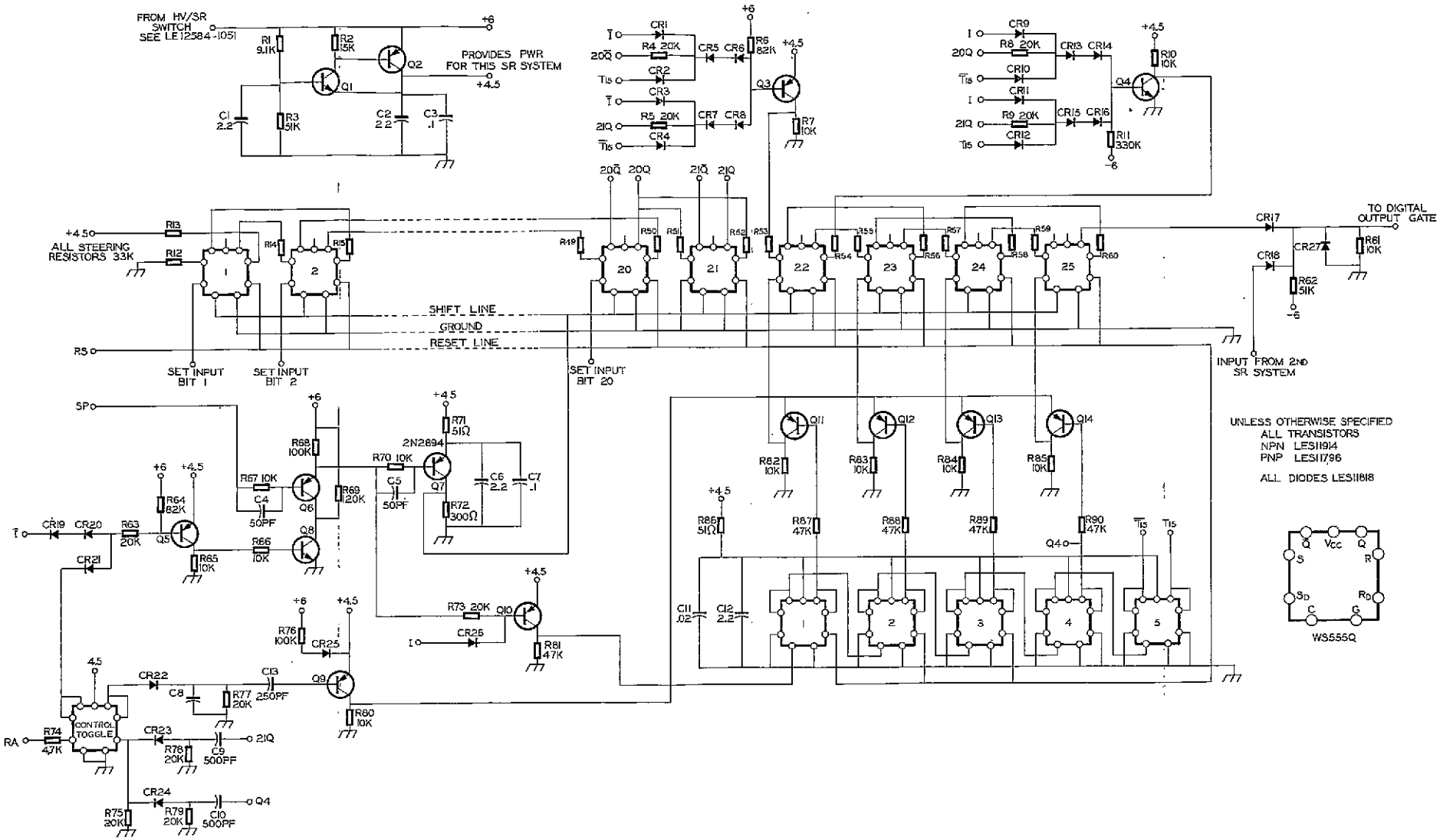

Fig. 4-13. Floating-point shift register system (LE 12854-15).

FOLDOUT FRAME 1

FOLDOUT FRAME 2

The decoded data output is given by:

$$N = (\overline{1},1)_9 + (\overline{2},2)_8 + (\overline{4},4)_7 + (\overline{8},8)_6 + (\overline{16},16)_5$$

if

$$(\overline{8},8)_4 + (\overline{4},4)_3 + (\overline{2},2)_2 + (\overline{1},1)_1 = 15$$

otherwise

$$N = [(\overline{1},1)_9 + (\overline{2},2)_8 + (\overline{4},4)_7 + (\overline{8},8)_6 + (\overline{16},16)_5 + 32]\, 2^{[(\overline{8},8)_4+(\overline{4},4)_3+(\overline{2},2)_2+(\overline{1},1)_1]}$$

In this notation, the subscript indicates the bit number, bit 1 appearing first in time or to the left of the word. Note that with zero count the code comes up as 111100000. This none-zero output has been invaluable during experiment test, especially during integration of the experiment into the spacecraft.

4.4 ANALOG DATA—MAIN BODY COMMUTATOR

The commutation scheme is shown in Fig. 4-15. Diode gates are used which are controlled by the outputs of the primary commutator flip-flops, Fig. 4-7. Non-linearity caused by current division between the input and output diode is largely controlled by feedback in the output driver. Diode variations do occur which limit the over-all linearity and offsets to ±30 mV when the signal is larger than the zero non-linearity which is about 0.2 V at 22°C.

The data provided at the output of the main body commutator is shown in Table 4-2. The details of some of the circuits are supplied later.

4.5 ANALOG DATA—OPEP COMMUTATOR

The commutation scheme is shown in Fig. 4-16. The general approach is the same as for the main body commutator. Five WS 555 integrated flip-flops control the data sequencing. They are advanced on the trailing edge of P_2 to provide for data readout through the main body commutator slots 3, 7, 11, and 15. A description and comments on the data outputed is given in Table 4-3. Details of the circuits are given later.

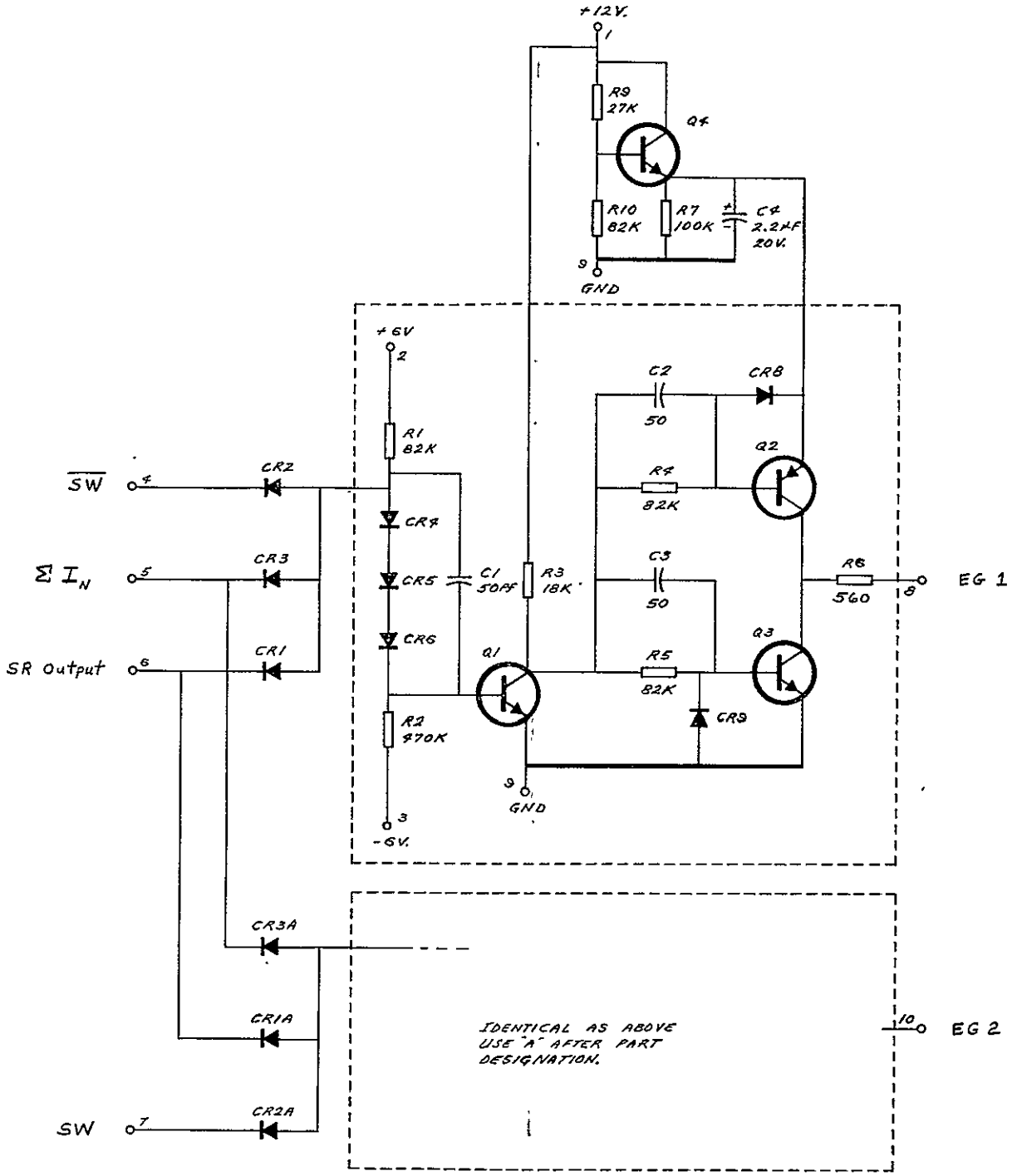

NOTES:
1. ALL DIODES ARE LES11818
2. ALL NPN TRANSISTORS ARE LES11918
3. " PNP " " LES11796

Fig. 4-14. Digital output gates and drivers (LE 12854-711).

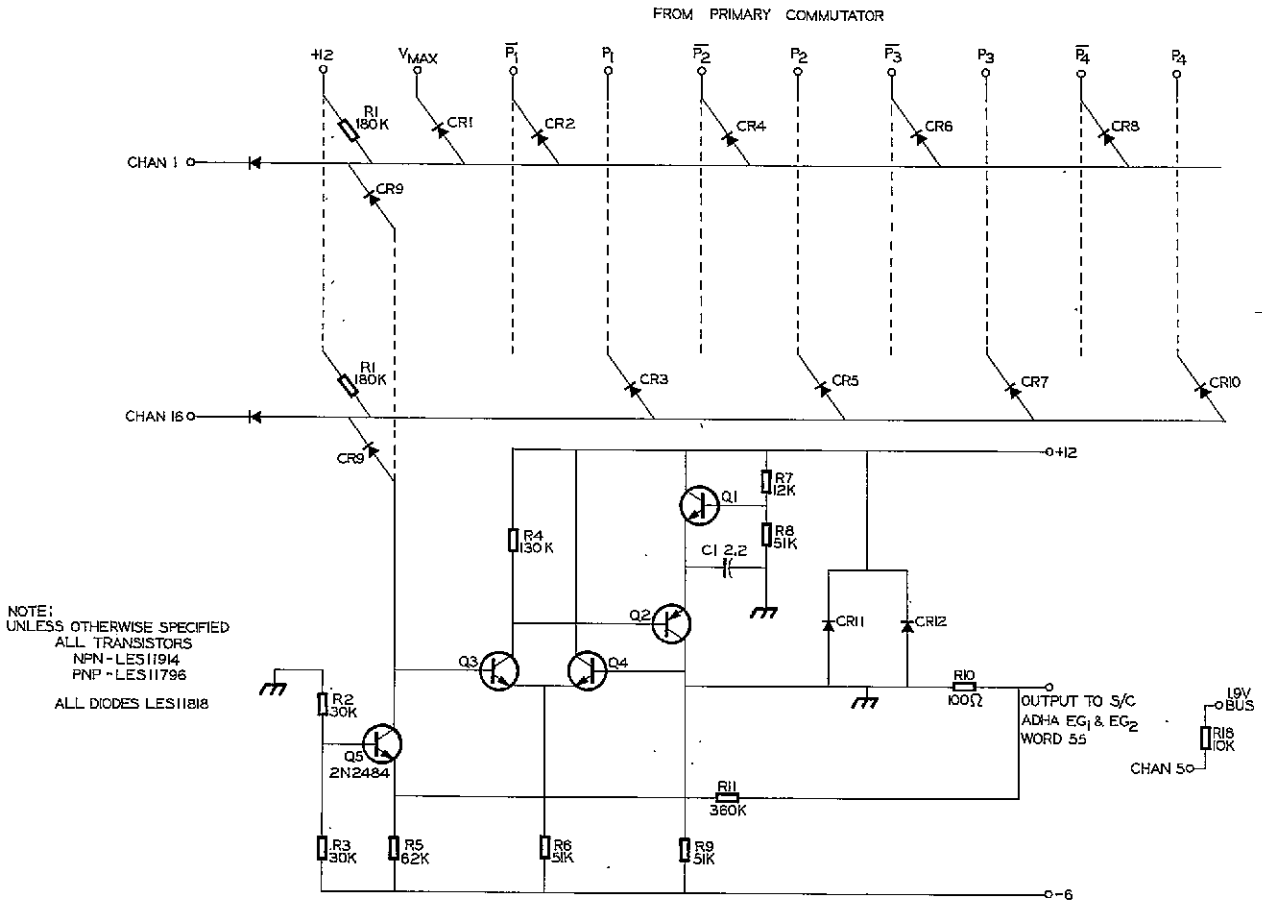

CHAN	DATA	$\overline{P_1}$	P_1	$\overline{P_2}$	P_2	$\overline{P_3}$	P_3	$\overline{P_4}$	P_4	V_{MAX}
1	IFC PG INDICATOR	X		X		X		X		X
2	SWITCH		X	X		X		X		X
3	OPEP	X			X	X		X		X
4	SHIFT REG HV		X		X	X		X		X
5	+1.9V MONITOR	X		X			X	X		X
6	MAIN BODY TEMP		X	X			X	X		X
7	OPEP	X			X		X	X		X
8	IFC PG INDICATOR		X		X			X		X
9	4.5 VOLT MONITOR	X		X		X			X	X
10	12 VOLT MONITOR		X	X		X			X	X
11	OPEP	X			X	X			X	X
12	+6.3 VOLT MONITOR		X		X	X			X	X
13	-6 VOLT MONITOR	X		X			X		X	X
14	GROUND		X	X			X		X	X
15	OPEP	X			X		X		X	X
16	SYNC		X		X		X		X	

Fig. 4-15. Main body analog commutator (LE 12854-14).

FOLDOUT FRAME 1

FOLDOUT FRAME 2

Table 4-2. Main body package commutated analog data.

Frame	Data designation	Comments
1 and 8	PG	Inflight calibration pulse generator. Initiated via Impulse Command (I. C.) No. 130. The calibration sequence synchronously starts with frame No. 1 and stops with frame No. 16. PG normally reads 4.70 ± 0.03[a] V. In the calibration mode, it will read 1.77 ± 0.03 V. PG mode is used only at the 1-k bit rate.
2	EG	Switch signal EG_1 = 0.47 ± 0.02 V EG_2 = 4.68 ± 0.02 V
3	OPEP	See Table 4-3.
4	SRHVM	Indicates the operational status of the two shift registers and the two detector high voltage supplies. At experiment turn on, the switching unit comes up in reset condition. The operational state after each exercising of I. C. No. 117 is

I. C. Command			SRHVM
0	SR_1	No HV	0.19 ± 0.02 V
1	SR_1	HV_2	3.03 ± 0.02
2	SR_2	HV_1	3.69 ± 0.02
3	SR_2	HV_2	4.29 ± 0.02
4	SR_1	HV_1	2.41 ± 0.02
5			

(repeat)

5	1.9 V	Monitor of the 1.9-V bus. Normally reads 2.29 ± 0.02 V.
6	MBT	Main body temperature. $T = 22.86\ V^{-1} + 36.73 - 12.16\ V - 0.155\ V^2$ in °C where V is the output signal in volts.
7	OPEP	See Table 4-3.
9	4.5 V	Normally reads 3.23 ± 0.02 V.
10	12 V	Normally reads 2.68 ± 0.04 V.
11	OPEP	See Table 4-3.
12	6.3 V	Normally reads 3.40 ± 0.02 V.
13	-6 V	Normally reads 3.07 ± 0.08 V.
14	Ground	Reads 0.20 ± 0.03 V.
15	OPEP	See Table 4-3.
16	SYNC	Provides experiment synchronization. It normally appears at the output of the experiment as a greater than 5.1-V pulse, and hence appears in telemetry as a binary 11111111. Note, however, that a guard is supplied in the experiment so that the other outputs (1-15) cannot rise above 4.69 ± 0.05 V. Hence, any signal ~4.8 to 5.1 V may be used for sync although 5.1 V is normally adequate.

[a]The limit assigned to each number is an indication of the normal variation to be expected over the operating temperature ranges of 0 to +40°C for the main body package and -30 to +30°C for the OPEP. In addition, the OPEP variation includes the offset variations (0.04 + 0.04 V) in slots 3, 7, 11, and 15 of the main body commutator. These values hold for flight unit 1 only. Flight unit 2 values are slightly different; however, the syncs do not change significantly.

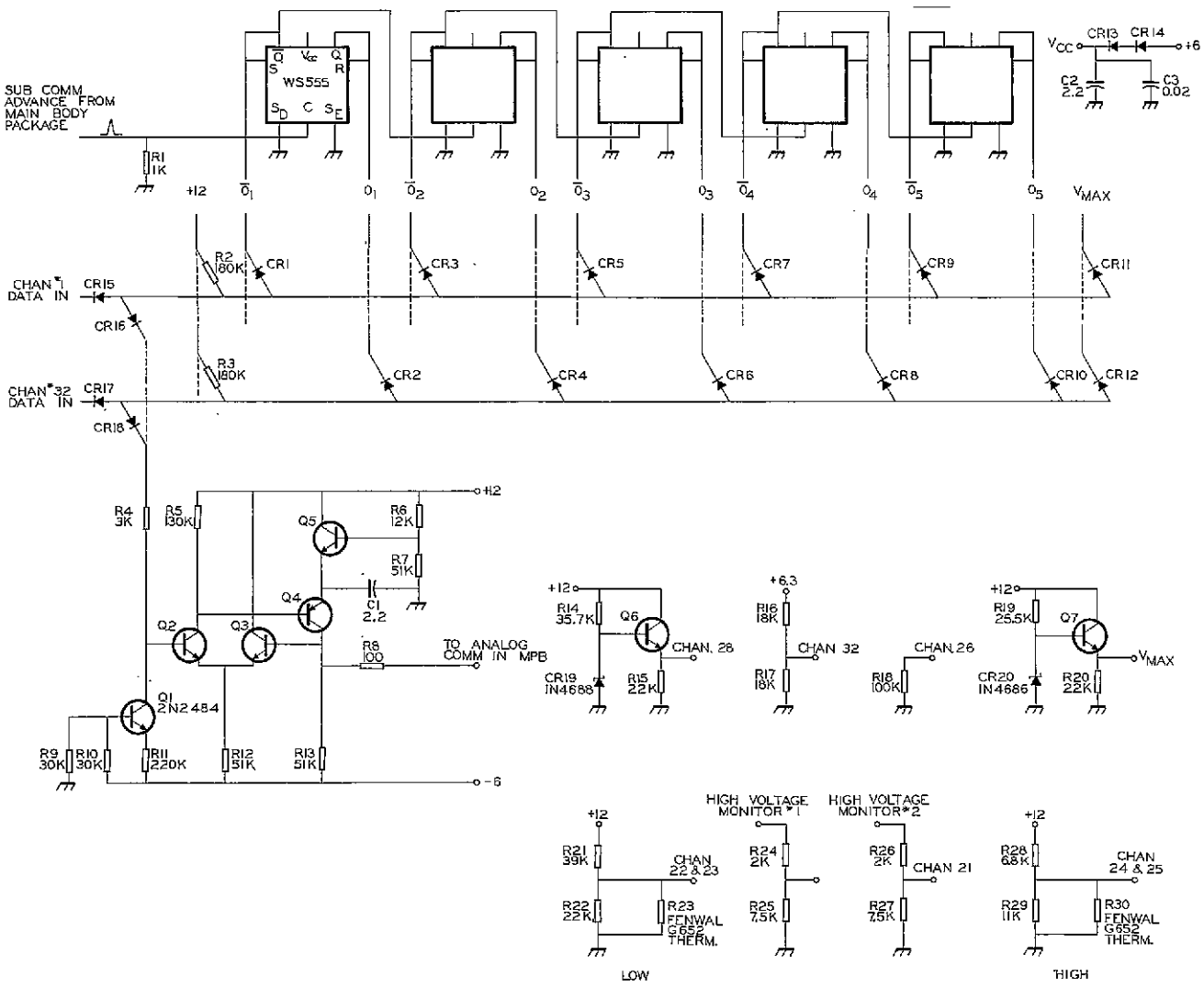

DIODE MATRIX CONNECTIONS

CHAN	DATA		$\overline{O}_1$	O_1	$\overline{O}_2$	O_2	$\overline{O}_3$	O_3	$\overline{O}_4$	O_4	$\overline{O}_5$	O_5	V_{MAX}
1	CURRENT MONITOR	E_1	X		X		X		X		X		X
2	"	B_1 & B_2		X	X		X		X		X		X
3	"	E_2	X			X	X		X		X		X
4	"	E_3		X		X	X		X		X		X
5	"	B_3	X		X			X	X		X		X
6	"	E_4		X	X			X	X		X		X
7	"	B_4	X			X		X	X		X		X
8	"	E_5		X		X		X	X		X		X
9	"	B_5	X		X		X			X	X		X
10	"	E_6		X	X		X			X	X		X
11	"	B_6	X			X	X			X	X		X
12	"	E_7		X		X	X			X	X		X
13	"	B_7	X		X			X		X	X		X
14	"	D_1		X	X			X		X	X		X
15	"	D_0	X			X		X		X	X		X
16	"	D_1		X		X		X		X	X		X
17	"	D_2	X		X		X		X			X	X
18	"	D_3		X	X			X		X		X	X
19	"	D_4	X			X	X			X		X	X
20	HV POWER #1			X		X	X			X		X	X
21	HV POWER #2		X		X			X	X			X	X
22	L.F MAG TEMP 1			X	X			X	X			X	X
23	H F MAG TEMP 1		X			X		X	X			X	X
24	L.F. MAG TEMP 2			X		X		X	X			X	X
25	H.F. MAG TEMP 2		X		X		X			X		X	X
26	+12 VOLTS			X	X			X			X		X
27	GROUND		X			X	X				X		X
28	OPEP FRAME SYNC'			X		X	X				X		X
29	GROUND		X		X			X			X		X
30	HALL PROBE 1 LF MAG			X	X			X			X		X
31	HALL PROBE 2 HF MAG		X			X		X			X		X
32	+6.3 VOLT			X		X		X			X		X
	HALL PROBE 1 ON			X	X			X			X		
	HALL PROBE 2 ON		X			X		X			X		
	HALL PROBE 1&2 RESET			X		X		X			X		

Fig. 4-16. OPEP package analog commutator (LE 12854-25).

FOLDOUT FRAME 1

FOLDOUT FRAME 2

Table 4-3. OPEP package commutated analog data.

Slots starting at sync	Data designations	Comments
1	SYNC	A 4.58 ± 0.08 V signal. The guard band voltage is set at ~4.0 V for OPEP signals. One uses ~4.3 to 4.7 V as OPEP SYNC, imposing of course the condition that the OPEP data comes out through the main body commutator at frames 3, 7, 11, and 15. Note that OPEP SYNC is not in a predetermined synchronization with the main body SYNC.
2	Ground	0.21 ± 0.08 V.
3	HE - 1	Hall effect probe for inflight measurement of the magnetic field of the low-field magnet. B = 175 + 358 V G. The normal temperature dependence is $V = 2.139 - 8.986 \times 10^{-3} T - 9.161 \times 10^{-5} T^2 + 0.856 \times 10^{-7} T^3$. T = °C.
4	HE - 2	For high-field magnet, B = 100 (17.96 - 6.20 V + 6.339 V^2 - 1.015 V^3) G. The normal temperature dependence is V = 2.921 - 1.147 T - 1.781 T^2 + 3.108 T^3. T = °C.
5	+ 6.3	Voltage monitor normally = 3.28 + 0.06 V.
6	CME 1	I = (3.30 - V)/1.10
7	CMB1B2	I = (2.65 - V)/1.10
8	CME2	I = (2.7 - V)/1.10
9	CME3	I = (2.3 - V)/0.34
10	CMB3	I = (2.5 - V)/0.34
11	CME4	I = (2.80 - V)/0.17
12	CMB4	I = (2.90 - V)/0.17
13	CME5	I = (2.95 - V)/0.17
14	CMB5	I = (2.35 - V)/0.17
15	CME6	I = (2.40 - V)/0.115
16	CMB6	I = (2.85 - V)/0.115
17	CME7	I = (3.15 - V)/0.085
18	CMB7	I = (2.52 - V)/0.085
19	CMDM1	I = (3.15 - V)/0.575
20	CMDZ	I = (2.60 - V)/0.575
21	CMD1	I = (3.56 - V)/0.114
22	CMD2	I = (3.0 - V)/0.114
23	CMD3	I = (3.73 - V)/0.114
24	CMD4	I = (3.37 - V)/0.114
		Detector current monitors. V = telemetry output in volts (0 to 5.1 V). I = leakage current in μA.
25	HV1	When the high voltage supply is off, HV1 = 4.00 ± 0.04 V. When on, HV1 = 3.38 ± 0.08 V. A reading of less than normal indicates excessive loading of the power supply.
26	HV2	Indicator for redundant supply.
27	LMT1	Low-field-magnet temperature probe. Low range. T = 7.29 V^{-2} + 2.07 V^{-1} + 15.2 - 17.3 V. T = °C.
28	HMT1	High-field-magnet temperature probe. Low range. See LMT1 for calibration.
29	LMT2	Low-field-magnet temperature probe. High range. T = 7.68 V^{-2} + 48.67 V^{-1} + 25.1 - 10.1 V. T = °C.
30	HMT2	High-field-magnet temperature probe. High range. See LMT2 for calibration.
31	+ 12 V	Normally = 3.36 ± 0.06 V.
32	Ground	Normally = 0.20 ± 0.08 V.

5. Status and Miscellaneous Circuits

5.1 INFLIGHT CALIBRATION PULSE GENERATOR

A major problem in space research is the credibility of the data. As an aid in solving this problem, we have included a pulse generator in the experiment. A pulse train rising in amplitude is inserted at the input to each detector-preamplifier (Fig. 2-13). The pulse train allows checking the discrimination levels of most of the discriminators in the system, provides a partial check of the accumulators, and provides a partial check of the shift register readout system.

The circuit diagrams are shown in Figs. 5-1 and 5-2. The system consists of two modules; the logic, located in the main body electronics package and the ramp pulse generator, situated in the OPEP package. Flip-flop No. 1 of the logic is initially set by a ground impulse command (No. 130). Occurrence of the 16th frame of I_{108} can then result in the synchronized turn-on of flip-flop No. 2, thus activating the 7.68-kHz pulse generator in the OPEP. The envelope of pulses rises linearly over a period of 16 frames of the DDHA (1-kbit rate) at which point the pulse train is terminated through resetting the logic circuits.

One stage of fail-safe protection is provided via the circuitry of Q9 in the ramp circuitry which provides turn-off of the pulse generator after about 3 min of operation. A second stage of fail-safe operation is provided by the circuitry associated with Q5 in the logic circuitry. In case the first flip-flop fails with its output at 0 V, the circuit will prevent Q1 from turning on, thereby preventing the possibility of the pulse generator operating without a pulse command.

The pulse generator pulses, after proper attenuation (Fig. 2-13), are inserted via a 4.7-pF capacitor into the input of each detector-preamplifier. As the pulses accumulate, they are read out every four frames of the DDHA. A typical data run is shown in Table 5-1. The data run is for Jan. 1, 1969. The OPEP was at +2°C and the Main Body Package at +22°C. For a check on the pulse generator frequency, note the second O_1 readout. This readout was for four complete frames of the DDHA, that is, $4 \times 1.152 = 4.608$ sec. An indication of the channel width is determined by adding all readouts common to a given channel. The bottom discriminator tripping level of a channel is then found from the first reading and the upper level from the last reading.

The voltage dividers for the protons are selected to check out the maximum number of channels. Unfortunately a rather complex scheme would be required to checkout the complete proton and alpha logic, and this has not been done.

5.2 HALL PROBE

The magnetic flux from the permanent magnet material (Ferrimag V) of the magnets is temperature sensitive (temperature coefficient of the magnetic field being -0.19%/°C), and the change of flux with temperature is irreversible below ~-50°C. There is also the question of the long term stability of the magnetic material even

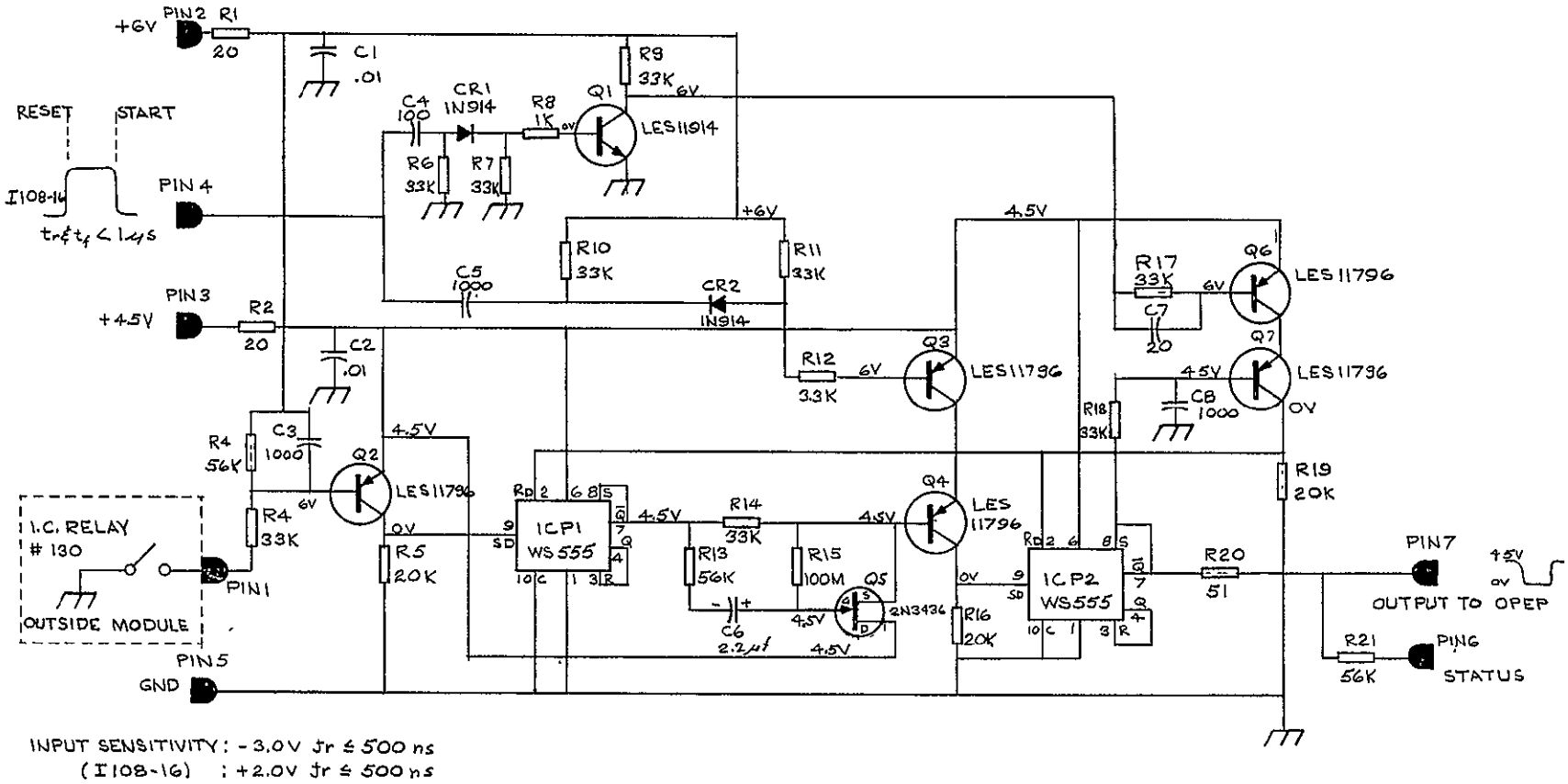

INPUT SENSITIVITY: -3.0V $t_r \leq 500$ ns
(I108-16) : +2.0V $t_r \leq 500$ ns

Fig. 5-1. Logic for inflight test pulser (LE 12854-561M2).

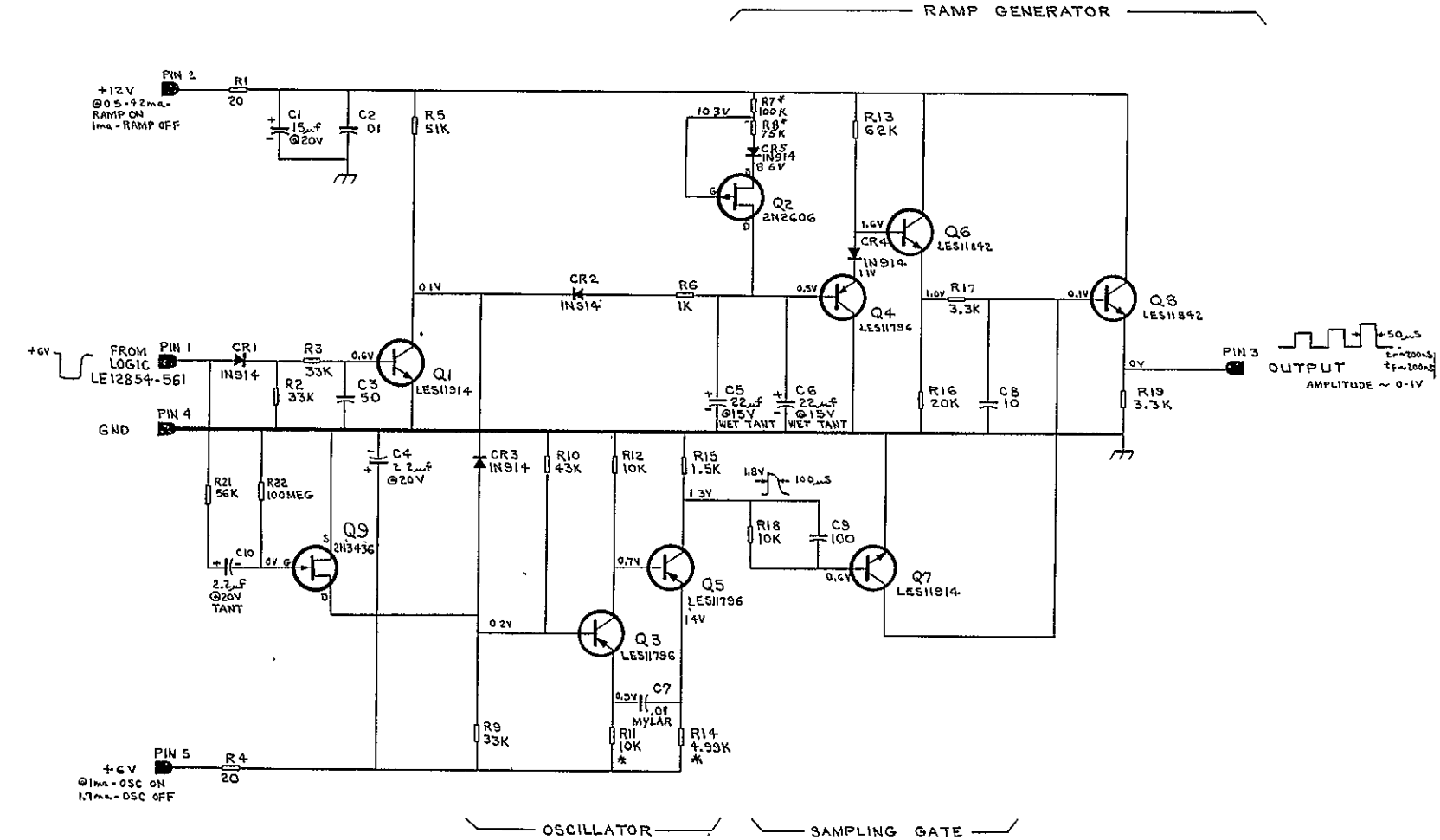

NOTE
1. VOLTAGES ARE GIVEN FOR CIRCUIT DURING THE "OFF" PERIOD WHICH IS CONTROLLED BY A +6V LEVEL INPUT FROM LOGIC.
2. THE SAMPLED RAMP OUTPUT AT EMITTER OF Q8 HAS A DURATION OF 16 SECONDS WITH A RANGE OF 0.5-8 VOLTS FIRST 8 SECOND OF RAMP IS LINEAR WITHIN 2%.
3. OSCILLATOR FREQUENCY APPROX. 6KC.
4. * METAL FILM

Fig. 5-2. Inflight test pulser (LE 12854-571).

Table 5-1. Typical in-flight pulse generator run.

Frame of readout	Data count readout in the following words in the indicated frame									
	Word D10		Word D27		Word D50		Word D89		Word D108	
1										
2					P_2	3648				
3					O_1	20992				
4	PB_1	18432								
5	E_1	11	E_5	13312	E_2	14080	E_6	736		
6					P_2	5504			E_7	25088
7	P_1	28160					P_3	15616		
8	EB_1	18944								
9	E_1	25600	E_5	31744	E_2	18944	E_6	34816		
10	E_3	12800							E_7	1088
11	P_1	14336			O_1	35840	P_3	6912	E_4	23040
12	EB_3	23552			EB_6	32768				
13	E_1	30208	E_5				E_6	24064		
14	E_3	35840								
15									E_4	35840
16										
1	E_1									
2	E_3	12800								
3					O_1	14336			E_4	8448
4									EB_4	784

though the ferroceramics are fairly stable magnetic materials. For these reasons, it appeared advisable to provide each of the magnets with Hall probe magnetic field monitors.

The circuit diagram is shown in Figs. 5-3 and 5-4 (also reported in UCRL-14650-T[4]). The sequence of operations is as follows:

(1) Pulse Hall probes at position 30 and 31 of OPEP subcommutator.
(2) Amplify and stretch output pulses from Hall probe.
(3) Read out via analog output.
(4) Reset pulse stretchers at position 32 of the subcommutator.

5.3 DETECTOR LEAKAGE CURRENT MONITORS

A convenient way to monitor the state of the solid-state detectors is by means of leakage current. As long as we know the temperature of the detector, leakage current provides a rough check on the progress of radiation damage. In a well behaved detector, leakage current doubles every 8 to 10°C in the range of room temperature. Figure 5-5 shows the circuit used for measuring the current. The current consists of a simple FET source follower with a constant-current transistor. Values are chosen to be partially temperature compensating. Calibration is given as equations in Table 4-3.

5.4 TEMPERATURE PROBES

Temperature probes are provided to monitor the center of the main body electronic package and the two electron spectrometer magnets. Two probes are provided for each of the magnets. See Figs. 4-15 and 4-16. Calibration equations are given in Tables 4-2 and 4-3.

5.5 VOLTAGE MONITORS

The voltage monitors are simple resistive networks. See the circuit diagrams of the main body package and OPEP commutators, Figs. 4-15 and 4-16, respectively. Note that the commutator inputs load the networks. This must be considered in data interpretation in case significant deviations from normal are observed.

5.6 HIGH VOLTAGE/SHIFT REGISTER SWITCH

Redundant high voltage supplies and shift registers are provided which are controllable by ground command. The command logic is shown in Fig. 5-6 and the high voltage switch in Fig. 5-7.

[4] J. McQuaid, A Low-Powered Magnetic Hall Probe for Space Applications, Lawrence Radiation Laboratory, Livermore, Rept. UCRL-14650-T (1966).

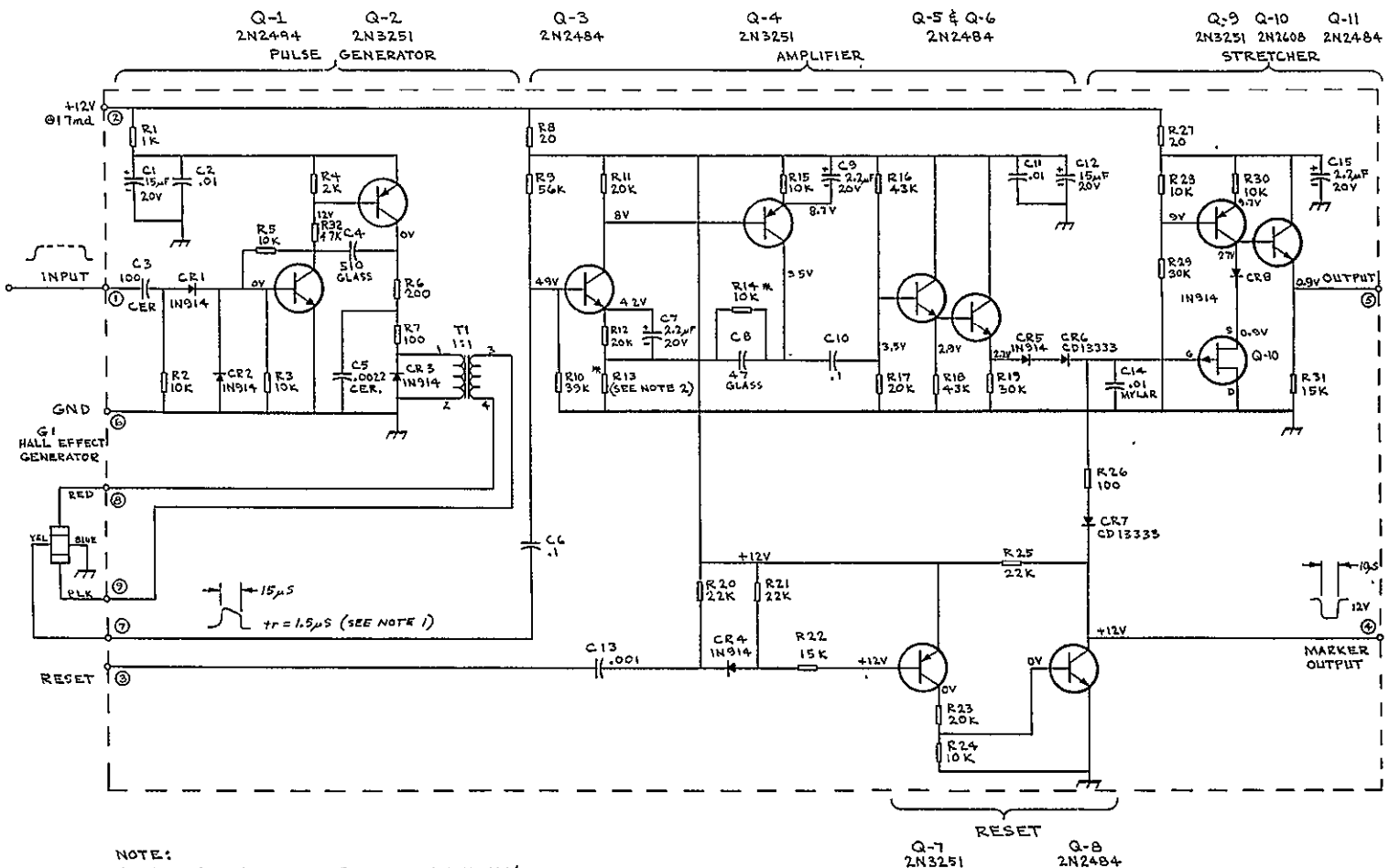

NOTE:

1. HALL GENERATOR OUTPUT = 0.154 VOLTS/KILOGAUSS.
2. R13 = 1K FOR 2500 GAUSS MAGNET (AMPL. GAIN: 11) (MOD 1)
   R13 = 300Ω FOR 800 GAUSS MAGNET (AMPL. GAIN: 21) (MOD. 2)
3. HALL GENERATOR G1 - BECKMAN MOD. 350, 7.7 VOLTS/AMP KG SENSITIVITY.
4. STRETCHER TIME CONSTANT = 50 SECONDS
5. TEMPERATURE COEFFICIENT = .03%/°C
6. INPUT SENSITIVITY ≥ 1.7 VOLTS
7. * = METAL FILM
8. HALL GENERATOR IS TO BE MOUNTED WITH "X" TOWARD NORTH POLE.

Fig. 5-3. Magnetic hall probe for spectrometer magnet (LE 12854-461).

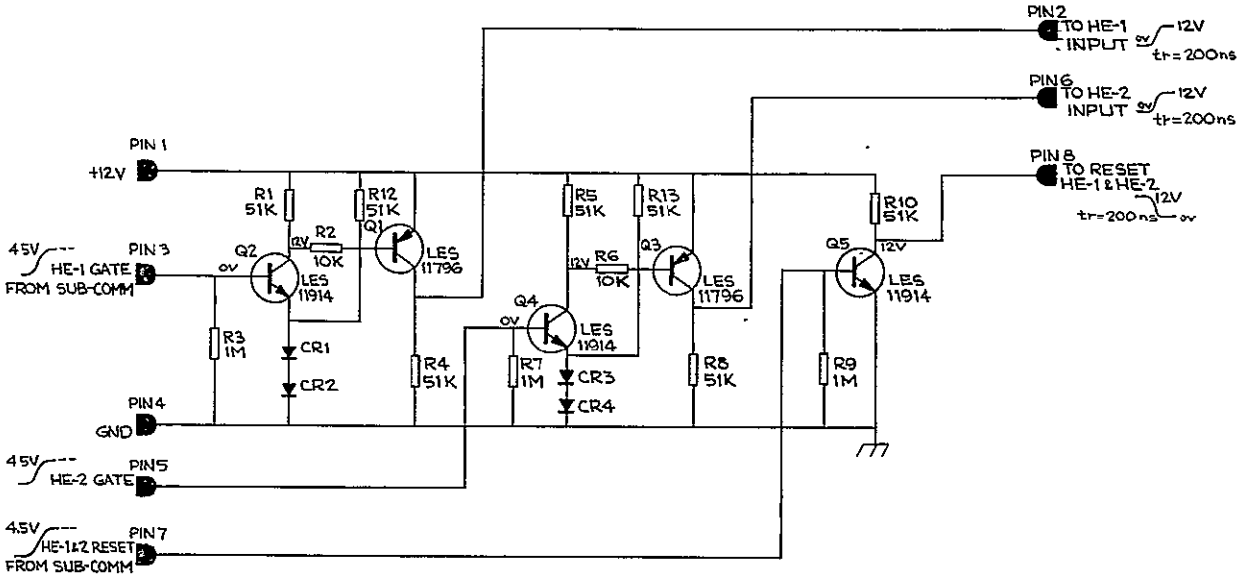

Fig. 5-4. Hall probe driver (LE 12854-1031).

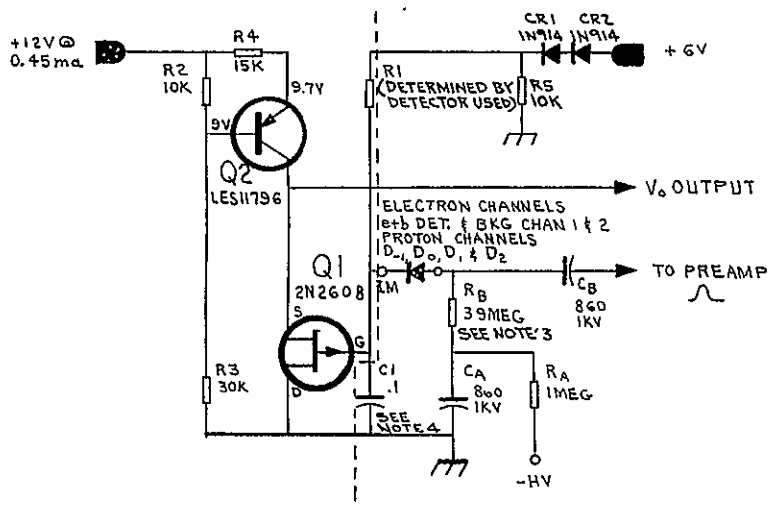

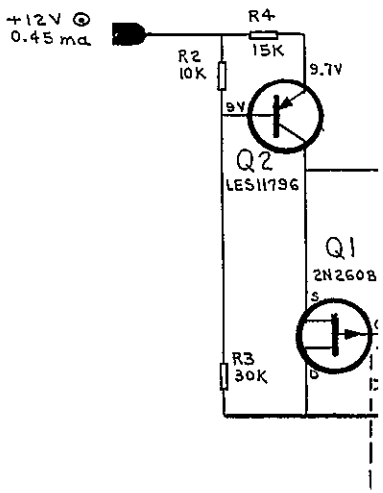

CHANNEL	RANGE (μa)	R1 (KΩ)	V_o (VOLTS)	SENSITIVITY V/μa
1	.2 - 2	1M	4.5 - 2.15	- 1.3
2	.2 - 2	1M	4.5 - 2.15	- 1.3
3	.5 - 10	300	4.5 - 1.65	- 0.30
4	2 - 20	150	4.35 - 1.65	- 0.15
5	2 - 20	150	4.35 - 1.65	- 0.15
6	3 - 30	100	4.35 - 1.65	- 0.10
7	8 - 40	75	4.05 - 1.65	- 0.106
D_0, D_{-1}	.3 - 5	500	4.5 - 2.15	- 0.40
D_1 - D_4	3 - 30	100	4.35 - 1.65	- 0.10

VOLTAGES ASSUME V_{GS} TO BE ~1.35V

NOTE 1. LEAKAGE MONITOR TEMP. COEF
2. OUTPUT VOLTAGE FROM MO PROPORTIONAL TO DETECT AS SHOWN IN TABLE AT LE
3. RB = 10 MEG FOR CHANNELS e_1, e_2,
4. LOCATED AT DETECTORS

Fig. 5-5. Detector leakage monitor (LE 12854-421).

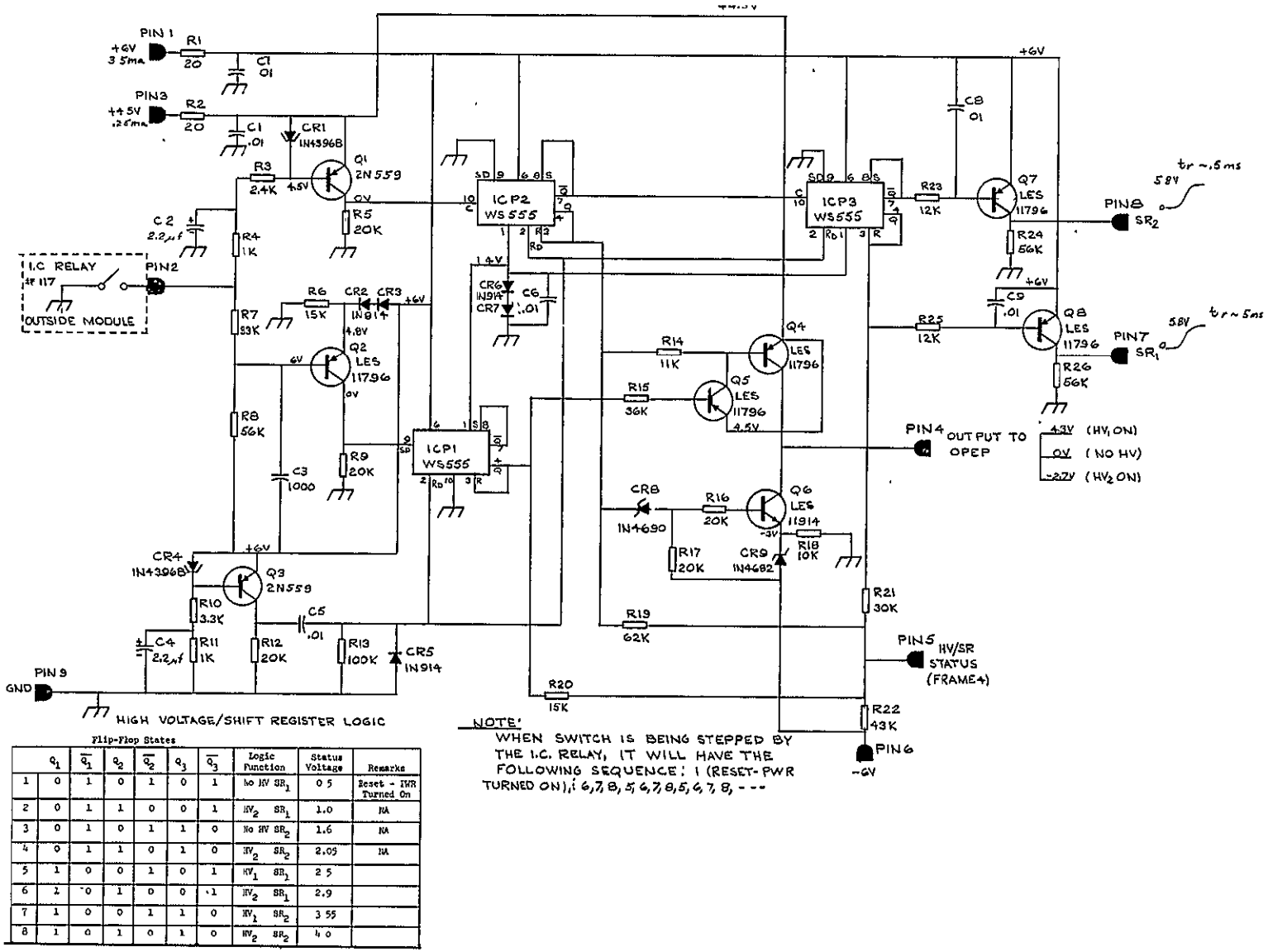

Flip-Flop States

	Q_1	$\overline{Q_1}$	Q_2	$\overline{Q_2}$	Q_3	$\overline{Q_3}$	Logic Function	Status Voltage	Remarks
1	0	1	0	1	0	1	No HV SR_1	0 5	Reset - PWR Turned On
2	0	1	1	0	0	1	HV_2 SR_1	1.0	NA
3	0	1	0	1	1	0	No HV SR_2	1.6	NA
4	0	1	1	0	1	0	HV_2 SR_2	2.05	NA
5	1	0	0	1	0	1	HV_1 SR_1	2 5	
6	1	0	1	0	0	1	HV_2 SR_1	2.9	
7	1	0	0	1	1	0	HV_1 SR_2	3 55	
8	1	0	1	0	1	0	HV_2 SR_2	4 0	

Fig. 5-6. High voltage/shift register switch (LE 12854-1051).

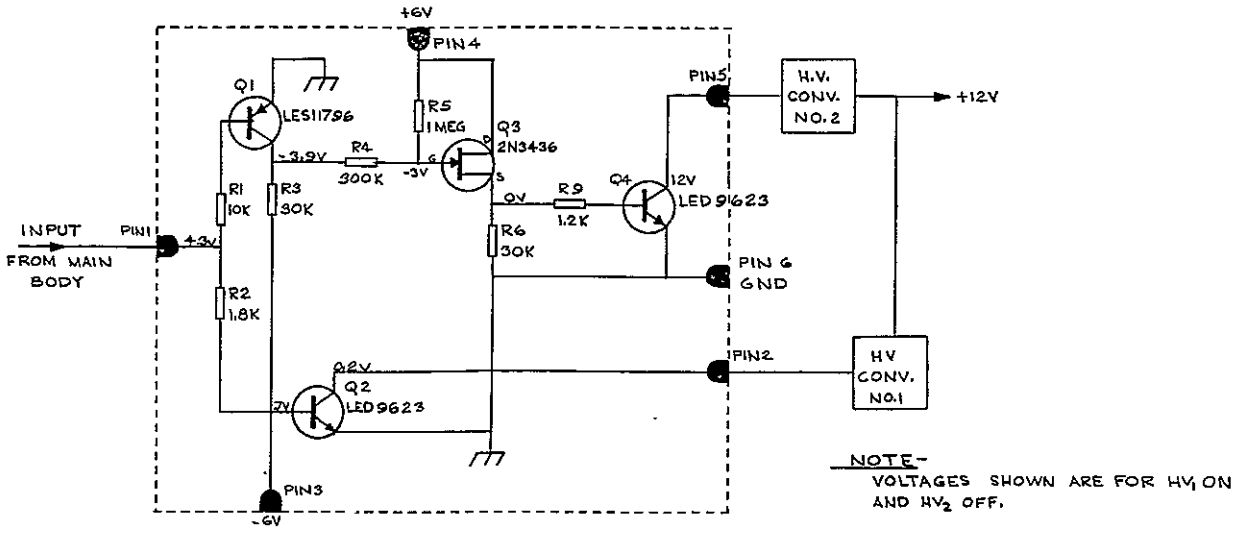

Fig. 5-7. High voltage switch (LE 12854-1061).

6. Electrical Construction

6.1 COMPONENTS

In keeping with the 1-year mission expectancy of the spacecraft, considerable effort went into component selection and screening. (See Table 6-1.)

All transistors and diodes were procured under high reliability specifications initiated by LRL, or tested to the specified levels at LRL. In addition to 100% of lot screening for hermetic seal, mechanical shock survival, and temperature cycling/stabilization; all devices were burned-in at full rated power for a minimum of 200 hr. Two parameters were monitored as a screening criteria; h_{FE} and I_{CBO} for transistors, V_f and I_L for diodes. Devices which exhibited a parameter drift >5% in V_f or h_{FE}, or >25% in leakage current were rejected from flight model fabrication. The conservative design use of transistors and diodes, using these devices at typically less than 0.05% of rated power, also contributes to high reliability.

The WS 555Q integrated circuit flip-flop, procured from Westinghouse Electric Corp., was extensively used in the experiment. The WS 555Q device was chosen for reasons of good noise immunity and low power dissipation. Noise immunity (all inputs and outputs including the supply voltage) is a nominal 1.5 V, while standby power dissipation for a supply voltage of 4.5 V is less than 1 mW. The NPN-PNP complementary outputs are well-suited to space application since a low output impedance is presented for both positive and negative going signals, and the relatively high power dissipation of collector resistors is avoided. More than 400 flip-flops are used in the experiment, indicating the need for low-power elements.

The WS 555Q devices were carefully screened by the manufacturer. Each device was x-rayed before and after a mechanical shock to insure that cracked, chipped, or voided dies were not allowed into the final test phase. After a hermetic seal test, each device had 30 parameters read and recorded while part serialization was established. A 168-hr burn-in at 125°C, with the device undergoing switch-testing, followed the preliminary parameter screen. Upon completion of burn-in, the 30 parameters were again read and recorded. After delivery to, and acceptance by, LRL the devices were incorporated into subassemblies and exposed to three temperature cycles of -55 to 125°C at a rate of 10°C per min. A 24-hr bake at 125°C completed thermal testing, after which electrical tests were performed on all assemblies. These tests simulated use conditions as nearly as practicable, and were conducted with the supply voltage at normal (+4.5 V) level and at half-level. Devices which would not pass this functional test were rejected from flight model use.

Two types of DC/DC converters were used in the system, a low-voltage (LV) type for developing +12, ±6, and +4.5 V from the 28-V spacecraft supply, and a high-voltage (HV) type for supplying bias to the solid-state detectors.

Two LV supplies were used in parallel redundancy, selectable by spacecraft power command. The LV supplies were furnished by Power Conversions, Inc. of

Table 6-1. Electrical components.

Device	LRL specification	Nearest vendor and/or equivalent
Integrated circuit	LES21051	Westinghouse WS 555Q
Transistor	LES11796	2N3251
Transistor	LES11803	2N2784
Transistor	LES11826	2N930
Transistor	LES11842	2N2484
Transistor	LES11825	2N396A
Diode	LES11818	IN3206
Transistor	Burned-in/screened at LRL	2N559
Zener diodes	Burned-in/screened at LRL	TRW 400-mW series
Tunnel diode	Burned-in/screened at LRL	IN4396B
Tunnel diode	Burned-in/screened at LRL	IN3713
Diode	Burned-in/screened at LRL	HPS1670
Field-effect transistor	Burned-in/screened at LRL	2N2606/08
Field-effect transistor	Burned-in/screened at LRL	2N3436
Field-effect transistor	Burned-in/screened at LRL	2N3823
Field-effect transistor	Burned-in/screened at LRL	TIX-S-41
Diode	Burned-in/screened at LRL	CD13333
Capacitor, solid tantalum	—	Sprague 350D
Capacitor, glass	—	Corning CYFR
Capacitor, wet tantalum	—	ITT RL
Capacitor, mylar	—	TRW 600 series
Capacitor, ceramic	—	Glenite/Chem-Electro
Delay line, lumped constant	LES11785	—
Resistors, carbon composition	—	Allen-Bradley AB, BB
Resistors, metal film	—	RN 55, Mil. Spec.
Transformers, pulse	—	Aladdin 94-117
Hall probe	—	Beckman Model 350
Connectors	—	Cannon DM series
Connectors	—	ITT Cannon ME series
Connectors	—	Continental MM series

Long Beach, California under a specification generated by Goddard Space Flight Center, and modified to meet the experiment requirements for +4.5-V power. These supplies, designated PS-14, weigh 150 g and operate at an efficiency of 60%. The power into the converter under normal operation and with the HV supply on is 3.5 W.

The input and output of the power supply are dc isolated as required by NASA specifications. The power supply uses a

chopper, free running at about 7.4 kHz and can be synchronized to the third harmonic of the spacecraft power-supply sync frequency. The experiment loads are approximately 80 mA at +12 V, 40 mA at +6.3 V, 70 mA at 4.5 V and 3 mA at -6 V. The design request was 140, 80, 150, and 6 mA, respectively. The current limiting of the outputs with the other outputs at design load were 250, 130, 130, and 375 mA respectively.

The HV converters were developed and produced by Electro-Development Corp. of Seattle. Each experiment flight package uses two HV supplies in parallel redundancy, programmable by impulse command. The same impulse command which is used to select output shift registers selects the HV supply to be operated.

The HV supplies weigh 35 g each, less electrostatic shield which adds several grams. The units operate from the well-regulated +12 V supplied by the experiment LV converter. The output voltages are isolated from ground, permitting either positive or negative operation of a particular output voltage. Outputs are: 500, 300, 200, 150, 100, 50, and 4 V; the lowest voltage is used as a status monitor. Design output currents are nominally 100 μA, contributing to the low overall efficiency of 30% which is not unusual for converters of this type. Current limiting sets the power out of the power supply to about 30 mW.

Particular attention was focused on RFI control, with tests conducted independently to insure that conducted/radiated EM energy would not interfere with other experiments. The converter frequency of 75 kHz was chosen in order to place the fundamental and all harmonics outside of the frequency bands measured by the antenna system of Haddock (Experiment E-20), University of Michigan.

6.2 FABRICATION

All circuit modules were either welded cordwood construction or integrated circuits. Soldering was used to secure the modules to the mother boards. The mother boards provide the electrical interconnections between the modules. The majority of this work was performed in this Laboratory by people having at least 5 years experience in aerospace fabrication. Inspection was performed at each level of fabrication. Each module was completely tested, including thermal cycling, before being incorporated into the various subsystems. Completed circuits were cleaned and then conformal coated with Epoxylite 2518, a polyurethane circuit board coating. The results of the fabrications may be seen in Figs. 7-2 through 7-6 and Figs. 7-8 through 7-12, the photographs of the experiment.

7. Mechanical

7.1 CONSTRUCTION OF OPEP PACKAGE

The OPEP package contains the sensors, consisting of the two magnetic electron spectrometers, and the proton telescope. Along with the sensors are the preamplifiers, detector HV supplies and status circuits. Fig. 7-1 shows the construction details. The base plate mounts on the scanning mechanism supplied by the Goddard Space Flight Center. Figs. 7-2 through 7-6 are photographs showing the configuration and general location of all the parts.

Note: The numbers shown in parentheses in Figs. 7-3 through 7-6 are prefixed with LRL drawing No. LE 12854-. E.g. in Fig. 7-3, (31M2) is LE 12854-31M2. When the OPEP is deployed, the-Z-axis of the spacecraft is perpendicular to the base plate of the OPEP package. Note that the apertures of the sensors look out and scan in the XY plane of the spacecraft (see Fig. 8-1).

The best angular resolution in the scan plane is achieved by mounting the spectrometers vertically. The spectrometers are mounted on Synthane plates (epoxy fiberglass) glued to the honeycomb uprights. The outside box as well as the uprights are of Hex-Cell honeycomb clad with 24 SRT aluminum. The inside of the cover as well as the upright members are at circuit ground. The whole outside is at chassis ground. The stray magnetic field from the magnets must be contained. This is accomplished by using vacuum-annealed Conetic 4 mils thick. This is bonded to the two outside upright panels and passes between the panels and the baseplate. A Synthane reinforced cover passes over the uprights and is held in place with screws. Battened joints in the Conetic shielding are provided. We were originally provided with a test shake specification of 60 g. Design models easily passed this test. Flight tests were to 30 g: The OPEP package weighs 12.0 lb.

7.2 CONSTRUCTION OF MAIN BODY PACKAGE

Refer to the mechanical drawing Fig. 7-7 and photographs Figs. 7-8 through 7-12. The circuitry is mounted on four Synthane mother boards which hold the circuit modules and provide electrical interconnections. These boards are 7.5 × 7.5 in. and are 0.0032 in. thick. The mounting scheme consists of clamping the outer edges of the boards with aluminum channel frames. Internal to the package, stiffness is provided by standoffs and the frames of interconnecting electrical connectors. The main body package weighs 6.5 lb.

7.3 TEMPERATURE RANGE

The experiment was tested over the range of -45 to +50°C and will operate indefinitely at these temperatures without damage. However, due to leakage current at high temperatures and the affect of adverse temperature coefficients at low temperatures, good operation is limited to -20 to +30°C. Channel E_1 is faulty below -20°C, and channel E_7 is faulty at greater than +30°C.

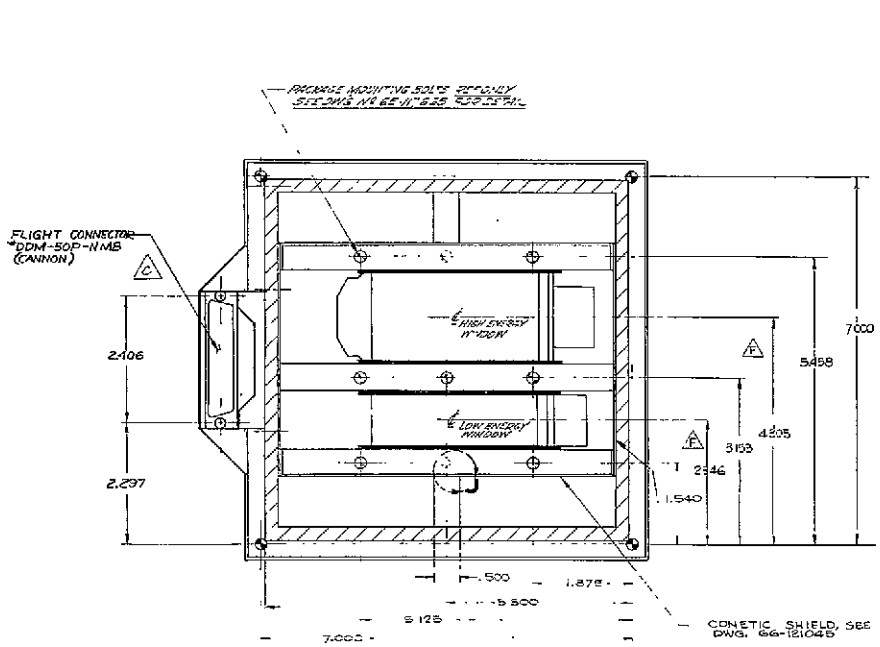

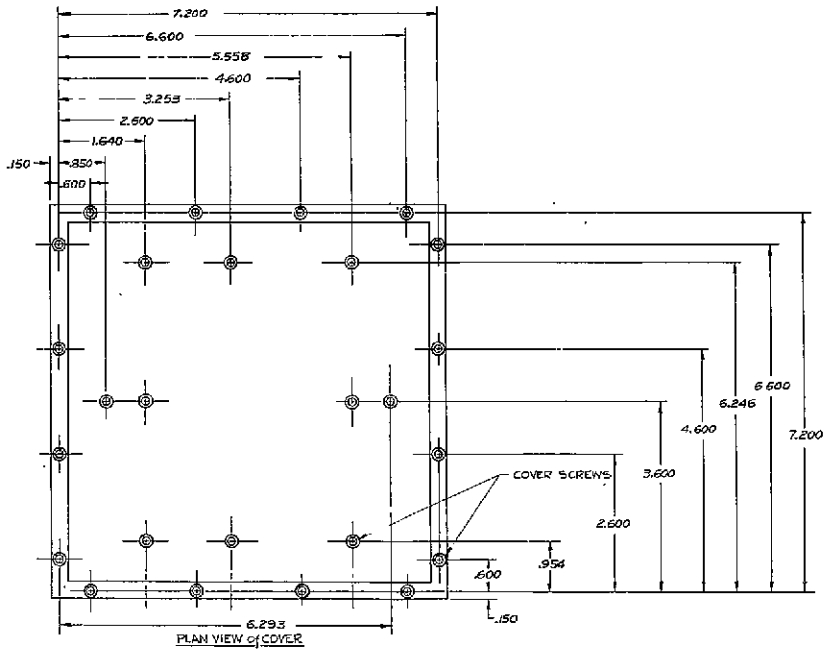

Fig. 7-1. Mechanical layout of OPEP package (sheet 1 of 2).

FOLDOUT FRAME 1

FOLDOUT FRAME 2

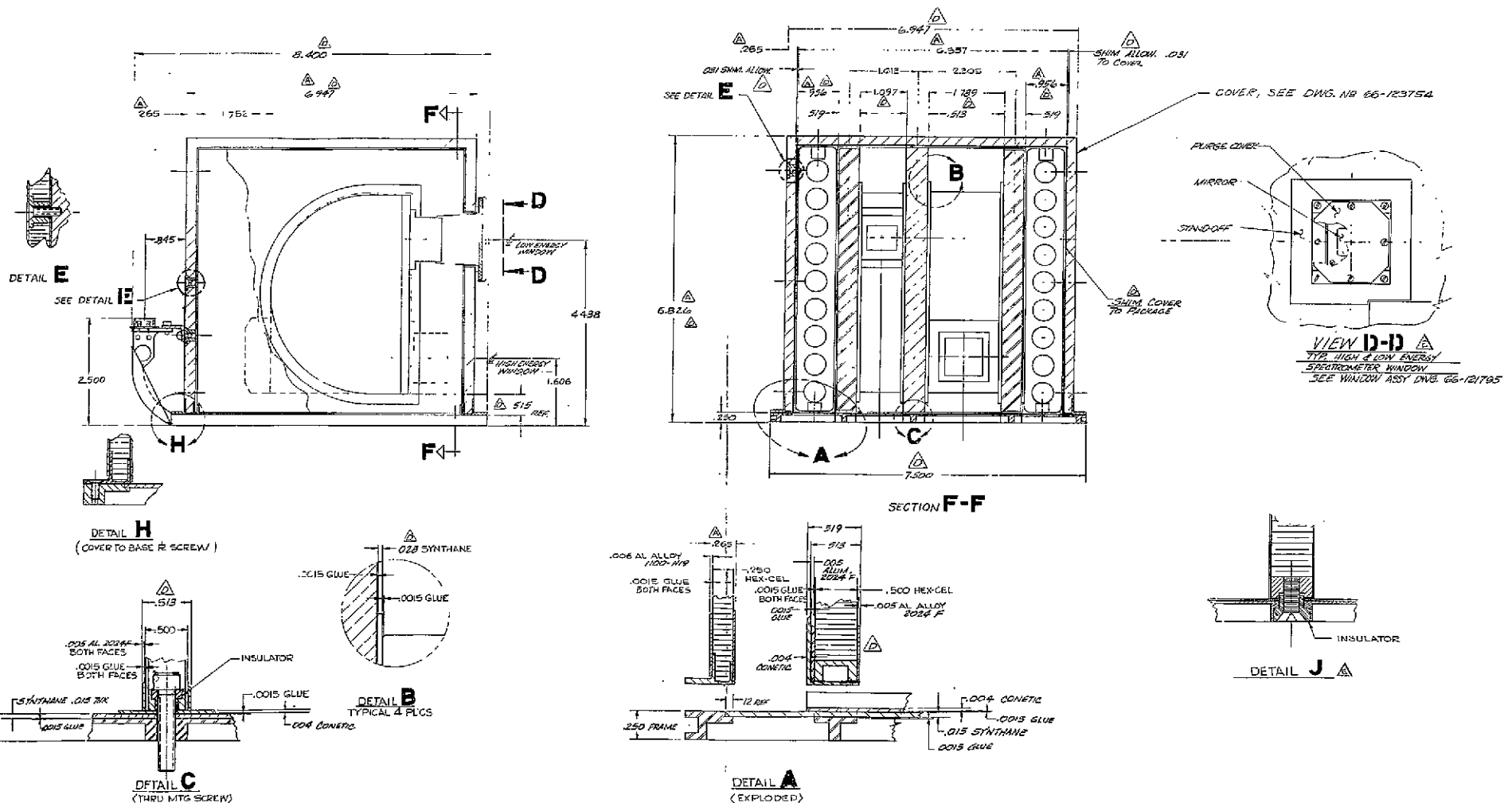

Fig. 7-1. Mechanical layout of OPEP package (sheet 2 of 2).

FOLDOUT FRAME 1

FOLDOUT FRAME 2

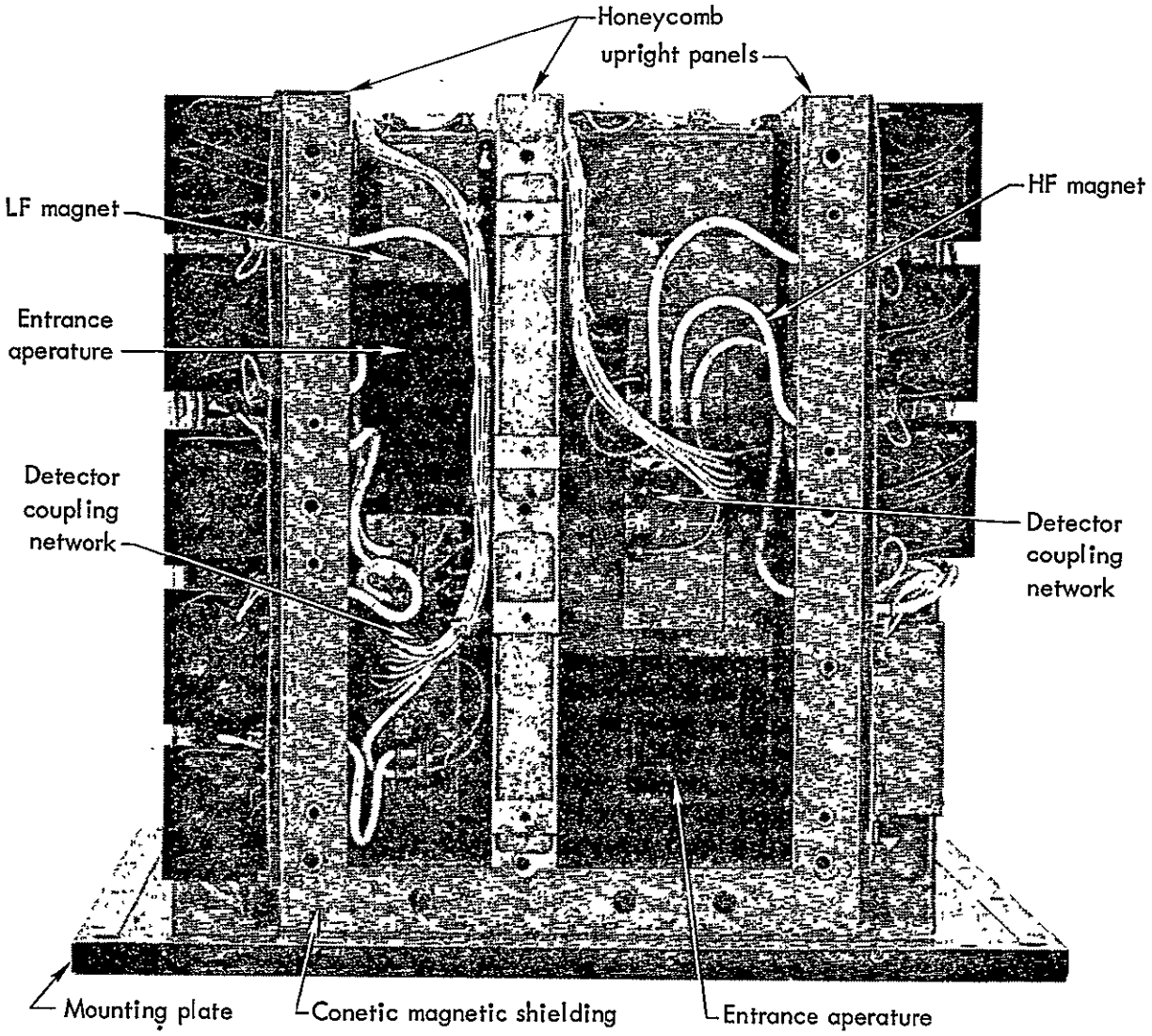

Fig. 7-2. Front view of OPEP package.

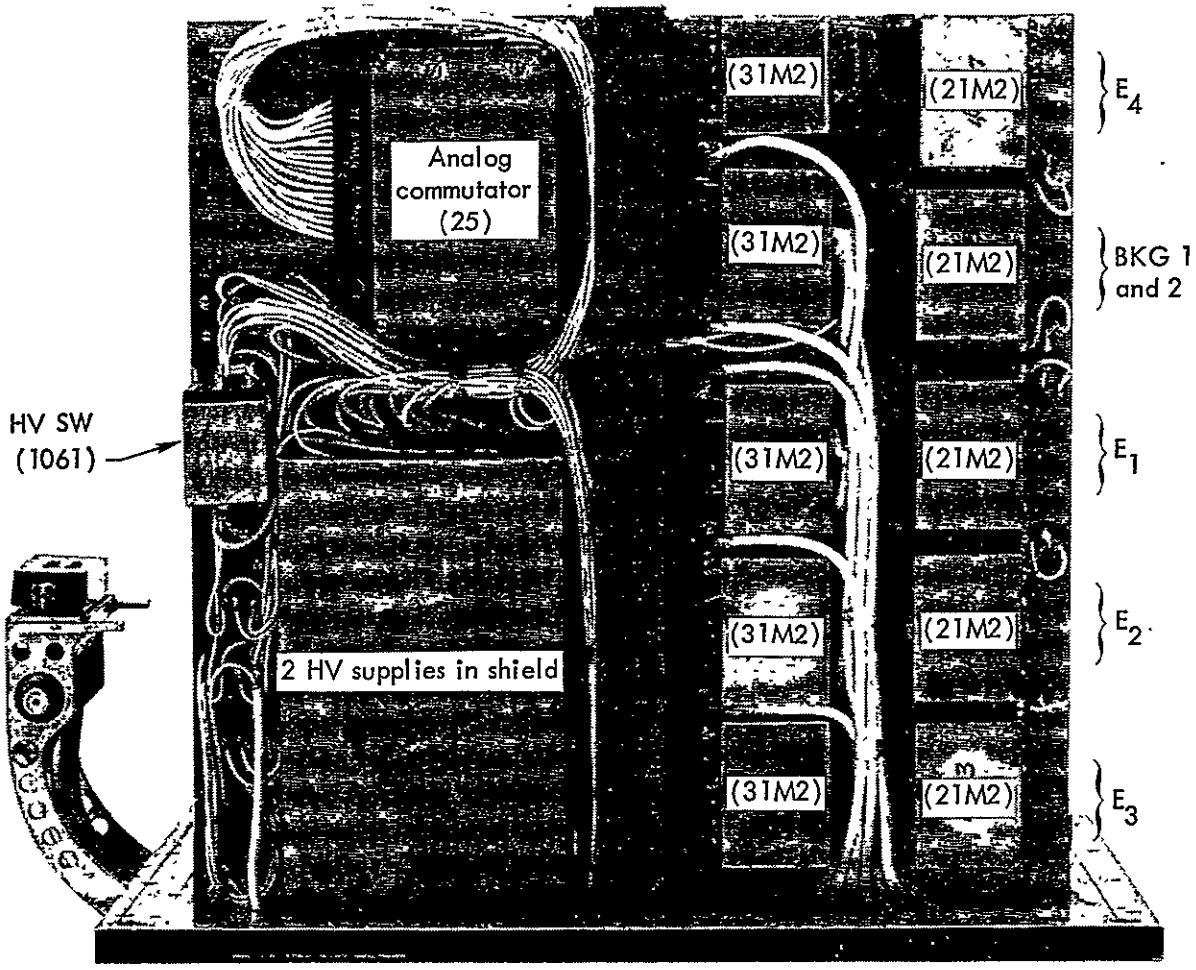

Fig. 7-3. Left view of OPEP package.

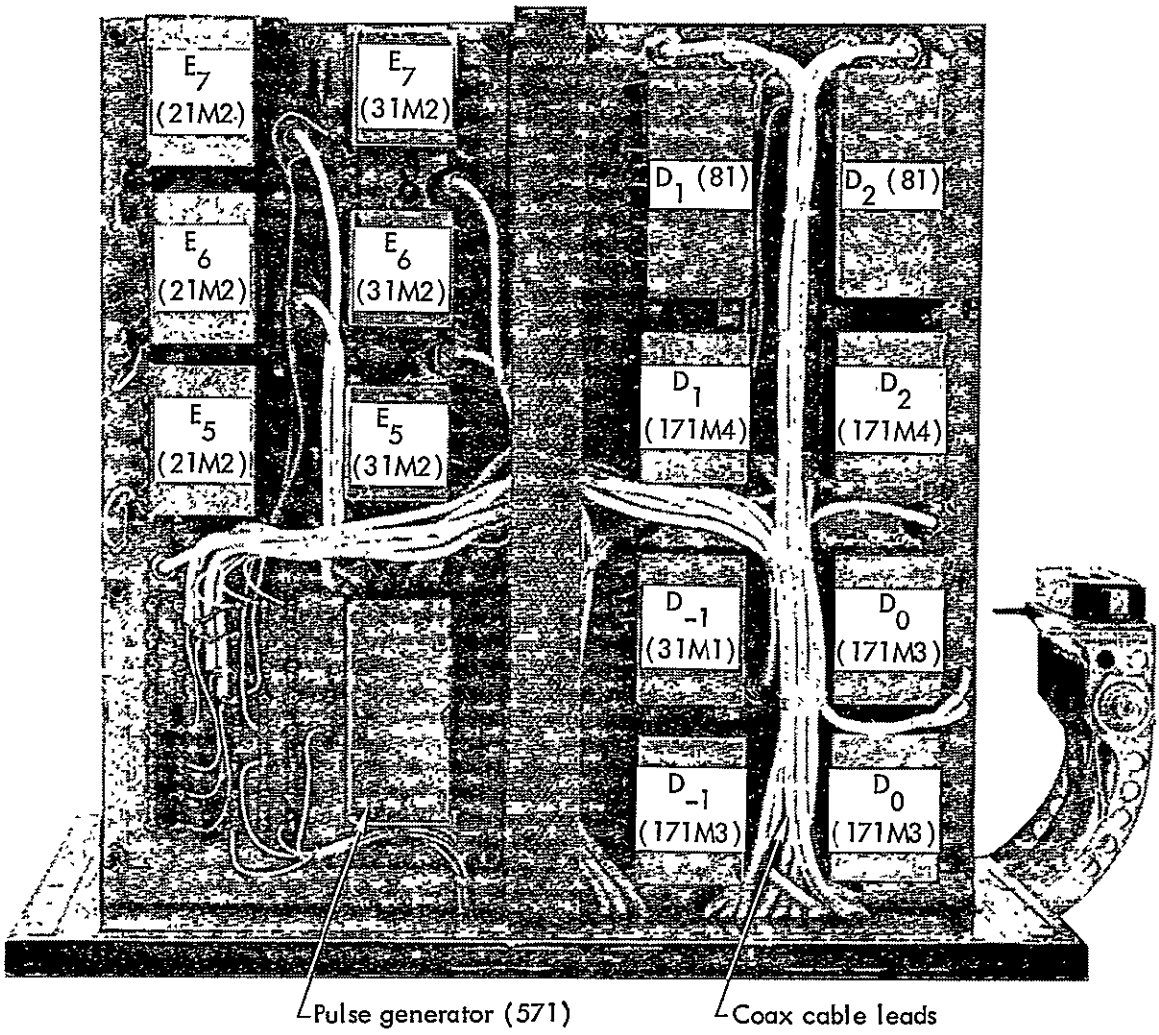

Fig. 7-4. Right view of OPEP package.

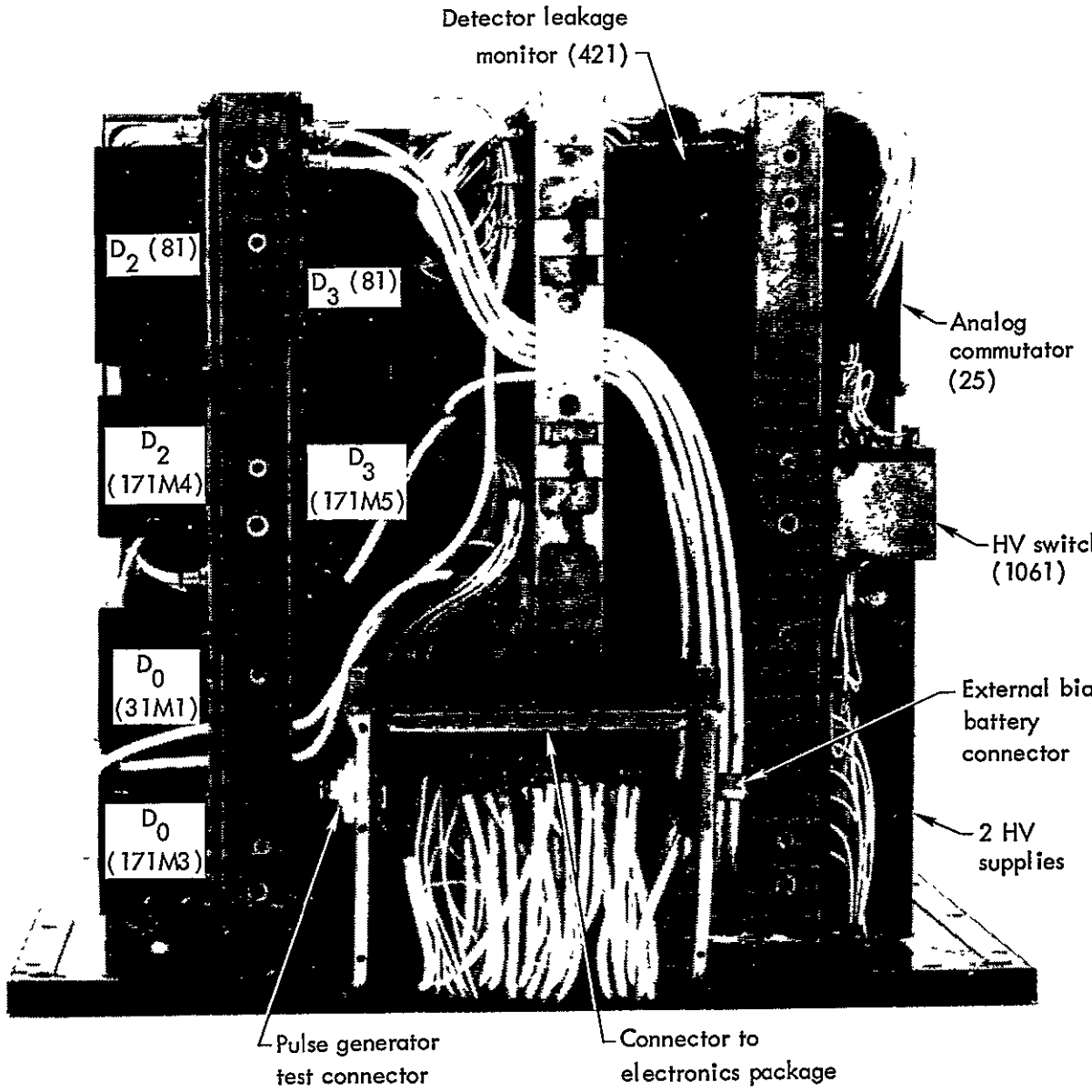

Fig. 7-5. Rear view of OPEP package.

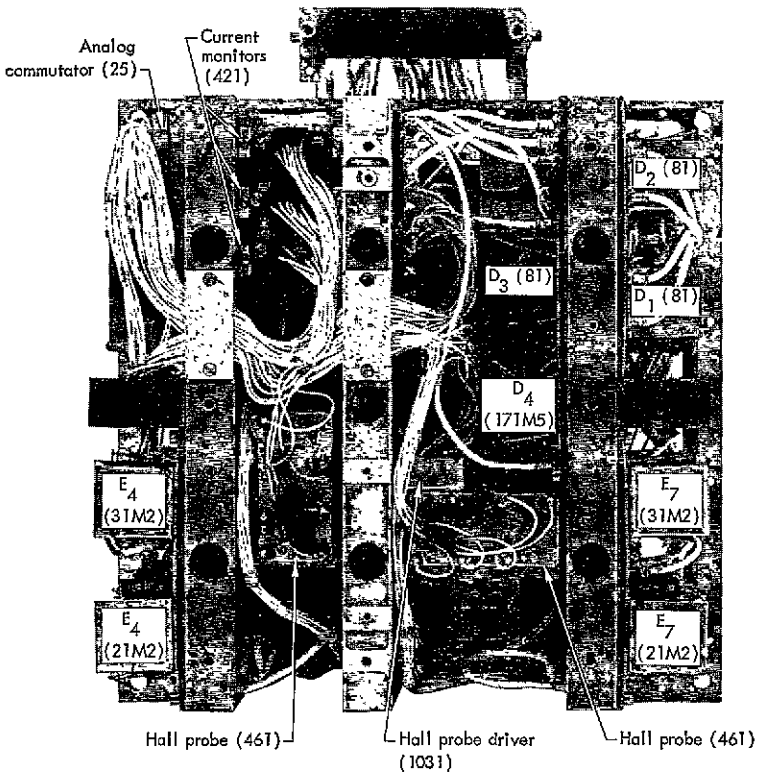

Fig. 7-6. Top view of OPEP package.

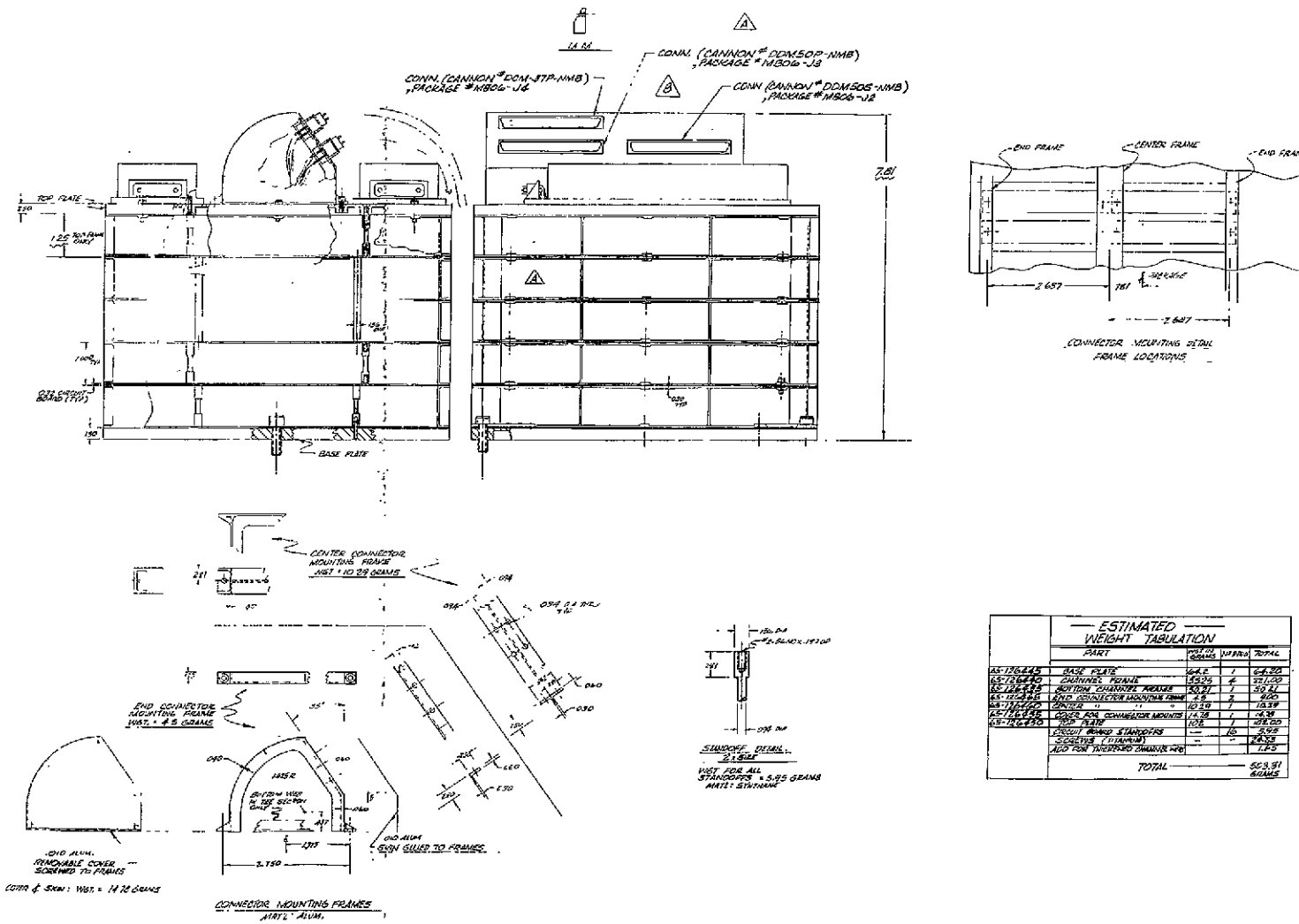

CONNECTOR MOUNTING DETAIL
FRAME LOCATIONS

	ESTIMATED WEIGHT TABULATION			
	PART	WGT. IN GRAMS	UNITS REQ'D	TOTAL
A5-1764-15	BASE PLATE	64.20	1	64.20
A5-1764-10	CHANNEL FRAME	15.75	4	63.00
A5-1764-20	BOTTOM CHANNEL BRACES	10.21	1	10.21
A5-1764-30	END CONNECTOR MOUNTING FRAME	4.5	2	9.00
A5-1764-40	CENTER " " "	10.29	1	10.29
A5-1764-45	COVER FOR CONNECTOR MOUNTS	14.72	1	14.72
A5-1764-50	TOP PLATE	108	1	108.00
	CIRCUIT BOARD STANDOFFS	—	18	5.95
	SCOTCH TY (TYPICAL)	—	—	24.73
	ADD FOR THICKER CHASSIS WEB			1.80
	TOTAL			503.31 GRAMS

Fig. 7-7. Main body package electronic layout (sheet 1 of 2).

FOLDOUT FRAME 1

FOLDOUT FRAME 2

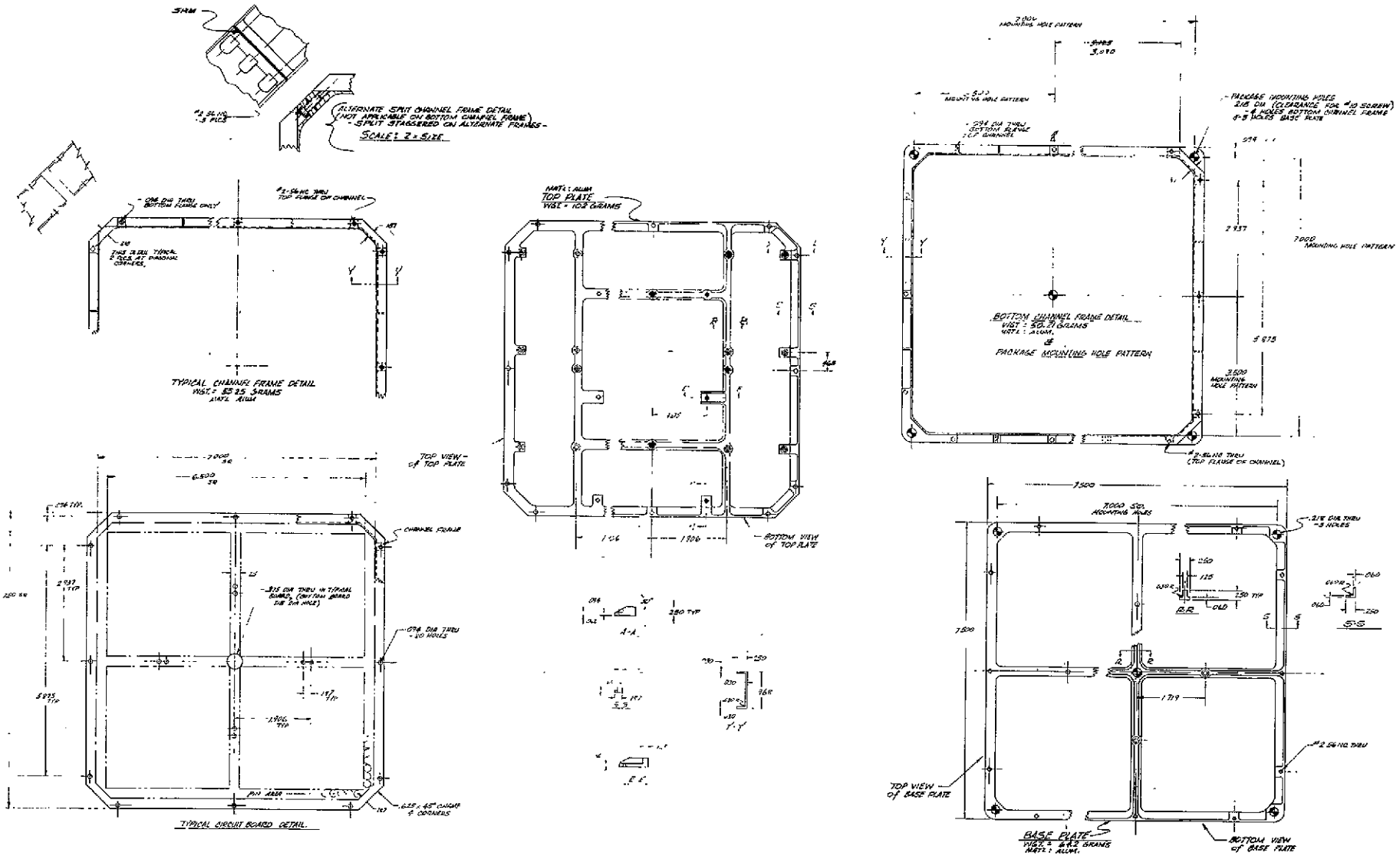

Fig. 7-7. Main body package electronic layout (sheet 2 of 2).

FOLDOUT FRAME 1

FOLDOUT FRAME 2

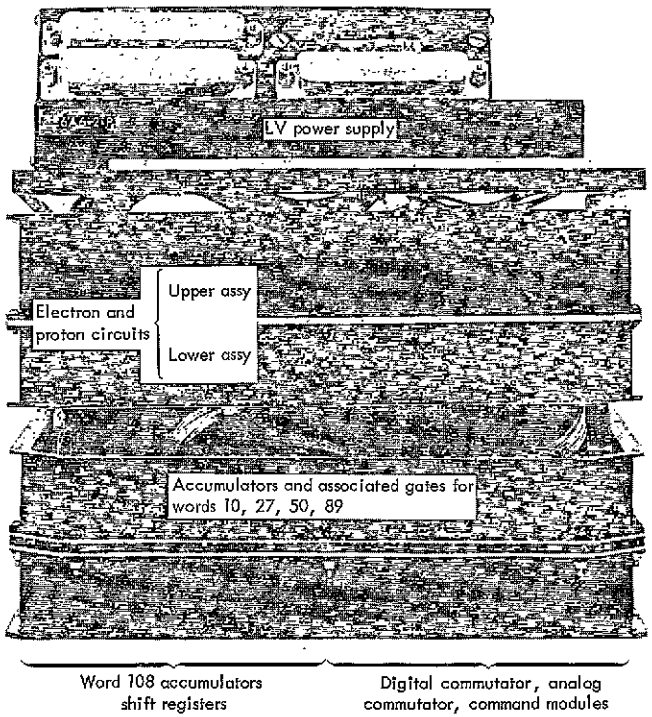

Fig. 7-8. Main body electronics package.

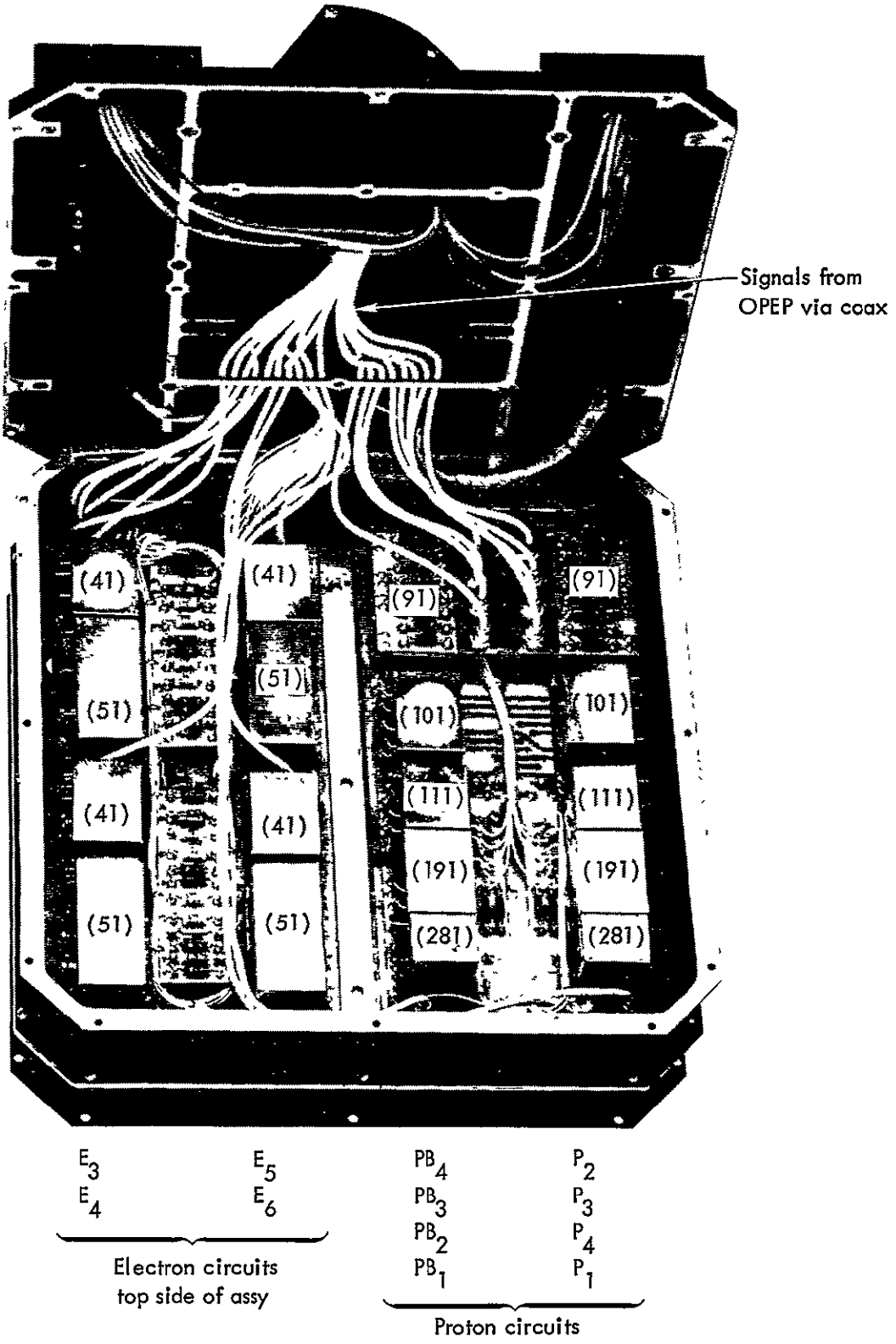

Fig. 7-9. Proton and electronic logic, top side.

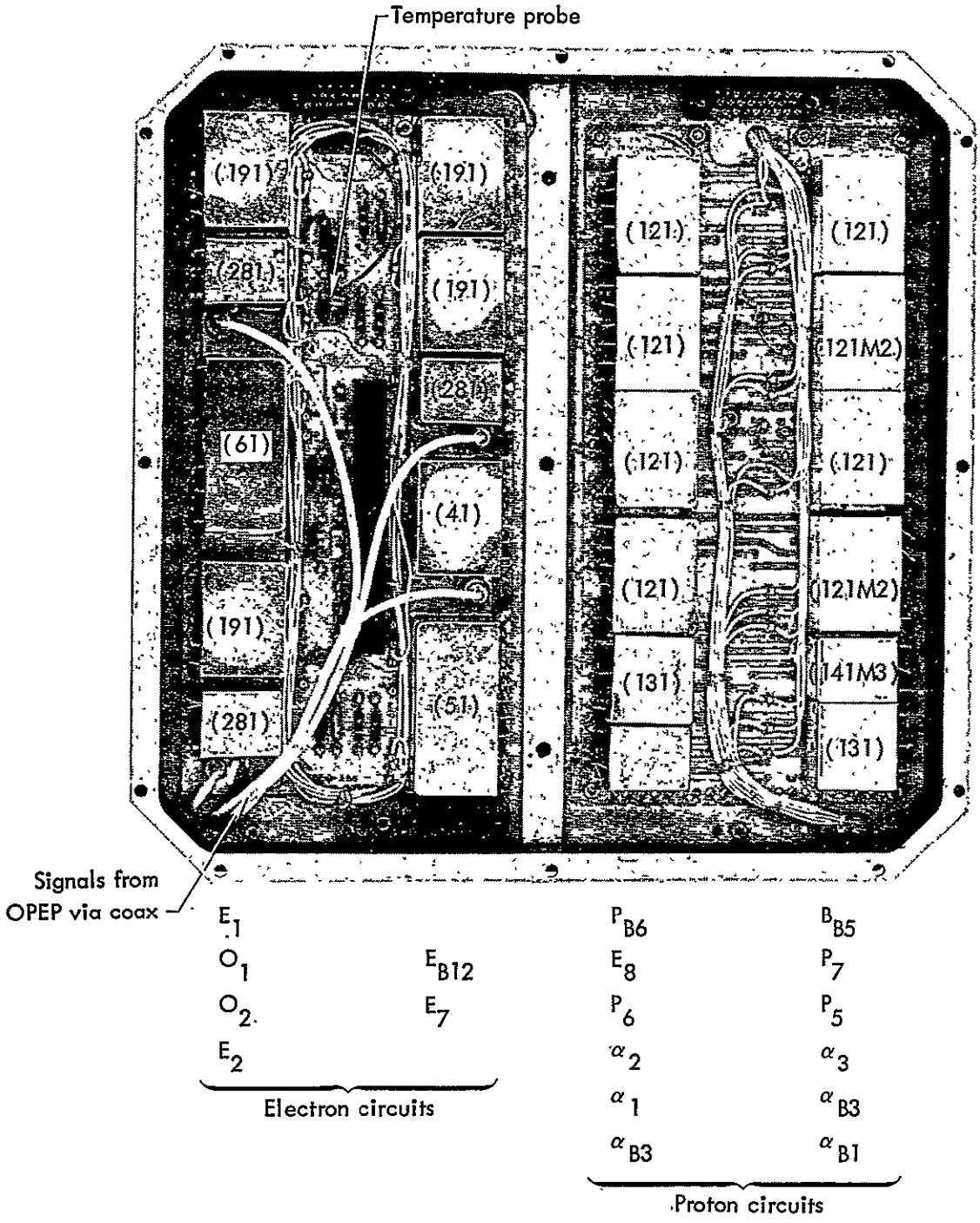

Fig. 7-10. Proton and electronic logic, bottom side.

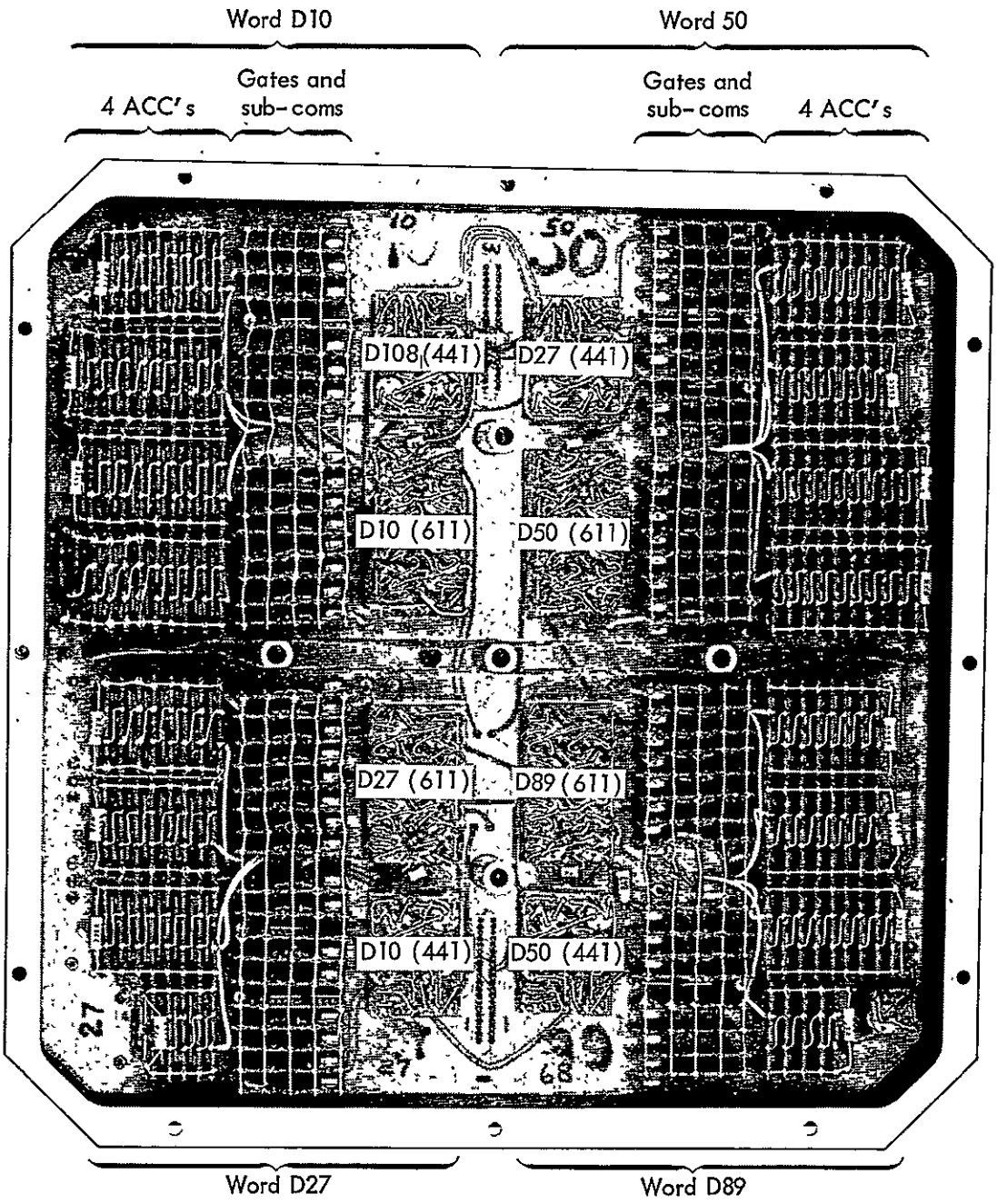

Fig. 7-11. Data accumulators.

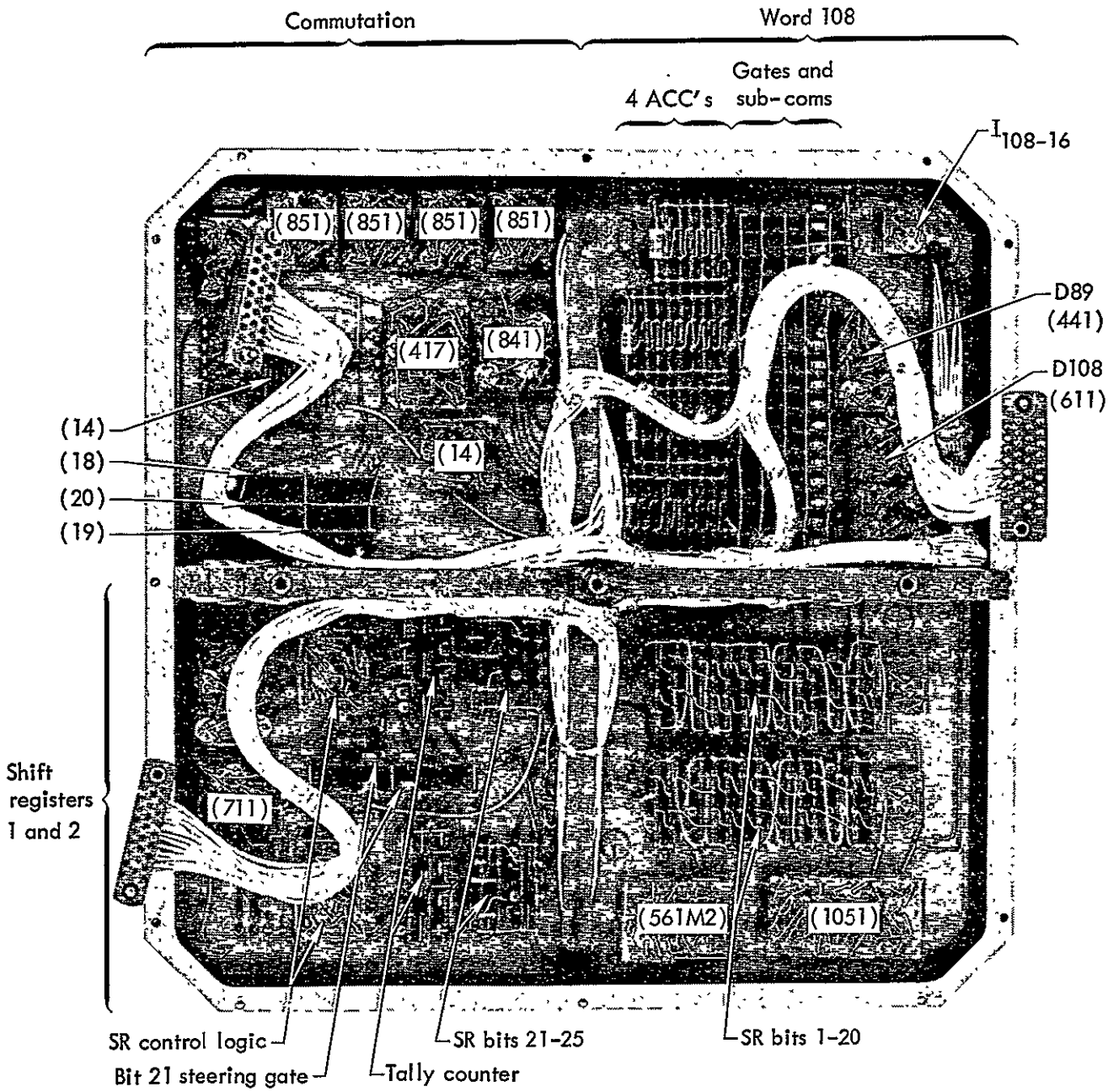

Fig. 7-12. Commutators and work 108 accumulator shift registers.

8. Sensor Orientation

8.1 COORDINATES

Figure 8-1 shows the coordinate system used on the spacecraft. Here we have

$X_b, Y_b, Z_b,$	body coordinate system
$X_p, Y_p, Z_p,$	solar-array coordinate system
X_e, Y_e, Z_e	OPEP coordinate system

The solar array and OPEP rotate relative to the body of the spacecraft. The spacecraft is constrained to orient so that Y_p (the perpendicular direction to the solar array) always looks directly at the sun, and Z_e of the OPEP axis always looks directly at the center of the earth. This is the ideal situation. In practice, the deviations are but a few degrees. The deviations

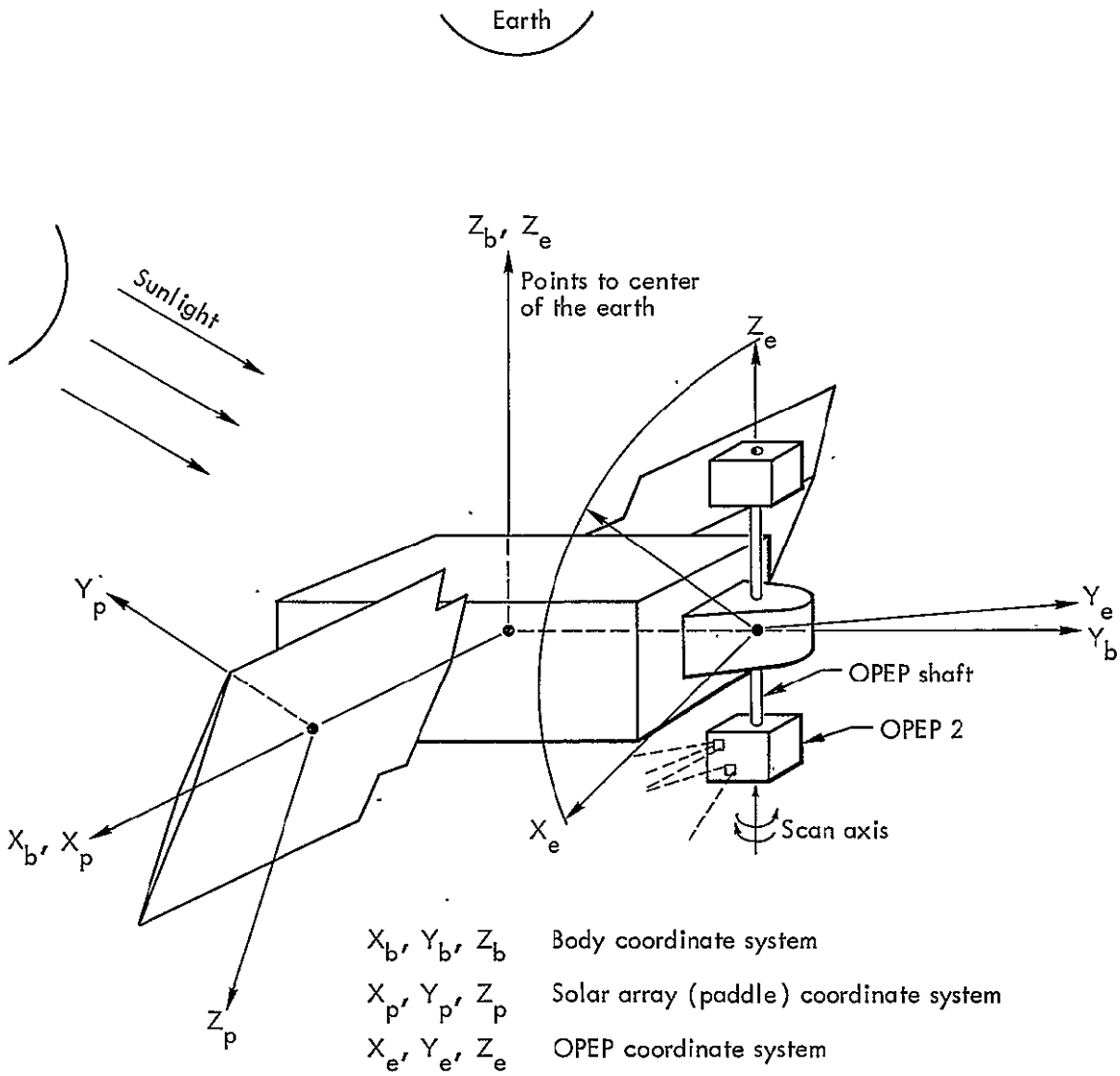

Fig. 8-1. Coordinate system showing ideal orientation of the OGO spacecraft.

are available as part of the spacecraft telemetry output. The array angle ϕ_p is measured counter clockwise from $+ Y_b$. ϕ_p varies between 90° and 270°.

8.2 SHAFT SCAN

The OPEP shaft is oriented along the Z-axis of the spacecraft. The shaft scan is provided as part of the normal spacecraft operation. Both OPEP 1 and 2 move during this operation. The shaft may be commanded to scan at an angular rate ~1.7°/sec. The turn-around of the mechanism occurs at a scan angle of -90° and +140°. Here the + angle is measured counterclockwise in the X_b Y_b plane from $+ X_b$. The angle is zero when X_e and X_b are aligned. There is a second, more usual, mode of shaft operation called the "gyro" mode. Here X_e is controlled to look forward into the plane of the satellite orbit.

8.3 OPEP-2 SCAN

This experiment, E-06, and experiment E-03 (low-energy charged particles) are located on a secondary scan mechanism attached to OPEP-2. This mechanism is indicated as E-25 and was provided through the efforts of R. Browning and H. Burdick of the NASA Goddard Space Flight Center. The mechanism can be commanded to scan back and forth at 3°/sec through an angle of ±115°. Readout is via a potentiometer system through analog word 109 on the main telemetry frame. The angle is decoded as $\theta = -121.96 + 0.9745$ A, in which A is the value of the analog readout (0-255). The difference between clockwise and counterclockwise readings is about 0.2°. The angle increases counterclockwise in OPEP coordinates, e.g. from $+ X_e$ to $+ Y_e$, the angle being 0 at $+ X_e$.

The central look angle of the spectrometer in spacecraft body coordinates is given directly by the sum of the OPEP shaft and OPEP scan angles. There are no fixed offsets. The look angle of the spectrometer must finally be related to physically significant parameters; the most important is the local magnetic field. The field data are being supplied from the UCLA flux gate magnetometer experiment E-14 (P. J. Coleman).

9. Post Launch Operation and Critique

9.1 ELECTRON COUNTING DATA

In general, the experiment has functioned well with few malfunctions since launch. The only electron spectrometer malfunction that has occurred has been associated with E_7, E_{B7}, O_1, and O_2. These channels are all derived from two thick detectors multiplexed together and both operating at 500-V bias. Occasional noise was evident shortly after launch and continued (less than 1% of the time) for the first few months of operation. Data between noise bursts are quite acceptable.

The procedure for determining background has worked well so that we are always confident of the background that needs to be subtracted. The electron-to-background ratio has typically been high, >100/1 for E_1 through E_5 except in the inner belt. Here we have electron-to-background ratios of typically 100, 100, 100, 20, 10, 2-0, 1-0, respectively. Here of course the major source of background is from penetrating protons. The low signal-to-noise ratio in the higher energy channels is a consequence of the low fluxes of these electrons.

The scanning mechanisms have worked effectively and have allowed good determination of directional distributions when the satellite was near the geomagnetic equator. When away from the geomagnetic equator, the physical constrictions of the experiment orientation prevent the sampling of low pitch angles. A good example of counting data is shown in Fig. 9-1. As shown, the counting rate is plotted by computer as a function of time. These data were taken at the 64-kbit rate. Here, eight data points were averaged for each point plotted for the electron data. The central look direction of the spectrometer relative to the direction of the local magnetic field is shown by the dotted sawtooth and the angle scale to the right of the graph. To provide a "road map" we have resorted to plotting $j_\perp$ (or rather the peak counting rates) as a function of time. A typical plot for the inbound and outbound orbits on March 9, 1968 are shown in Figs. 9-2 and 9-3. Here, the counting rates are normalized to the outer belt maxima.

The sensitivity of the electron spectrometer has been quite adequate for observations inside the geomagnetic cavity. At the other extreme, the sensitivity has not been so high that large dead time corrections are necessary or that the scaler capacities have not been adequate. Only the scalar on E_5 has overflowed, and this has been at the 1-kbit rate. It is not felt that extending the upper energy range of the spectrometer would be useful unless a factor of 10 or more in geometrical factor could be effected. Extending the energy range towards lower energies would of course be extremely valuable. Below about 40 keV, channeltrons should probably be used for particle detection. The structure of the spectra obtained near L = 3 and at low altitudes indicates that more energy channels would be valuable to provide the desired detail. In this instrument a great deal of complexity was provided to insure an accurate knowledge of the backgrounds. For most measurements beyond about 4 earth radii, this complexity could be reduced. However, during solar particle

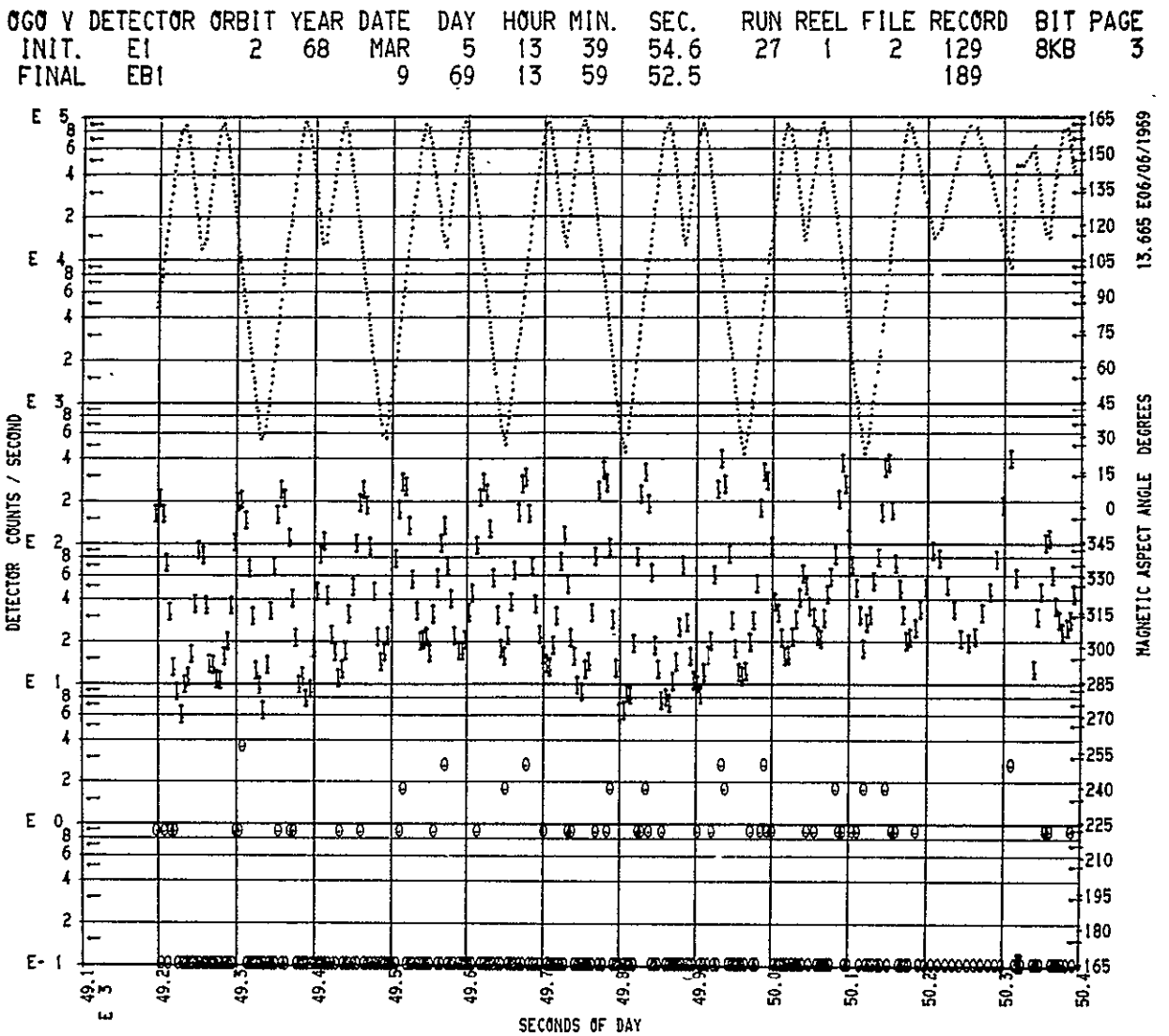

Fig. 9-1. Typical example of counting data, electron channel E_1.

events the ability to accurately measure background has been invaluable.

9.2 PROTON COUNTING DATA

Proton channels P_{1-7} have worked well. However, in August 1968 a problem developed with P_2 (the lowest energy channel in the telescope). Noise bursts appeared in synchronism with the scanning mechanism. Diagnosis of the P_2 channel via the inflight pulse generator indicates that otherwise the counting channel is all right and that the data that appears between noise bursts is acceptable.

The proton spectrometer has provided good data inside the geomagnetic cavity

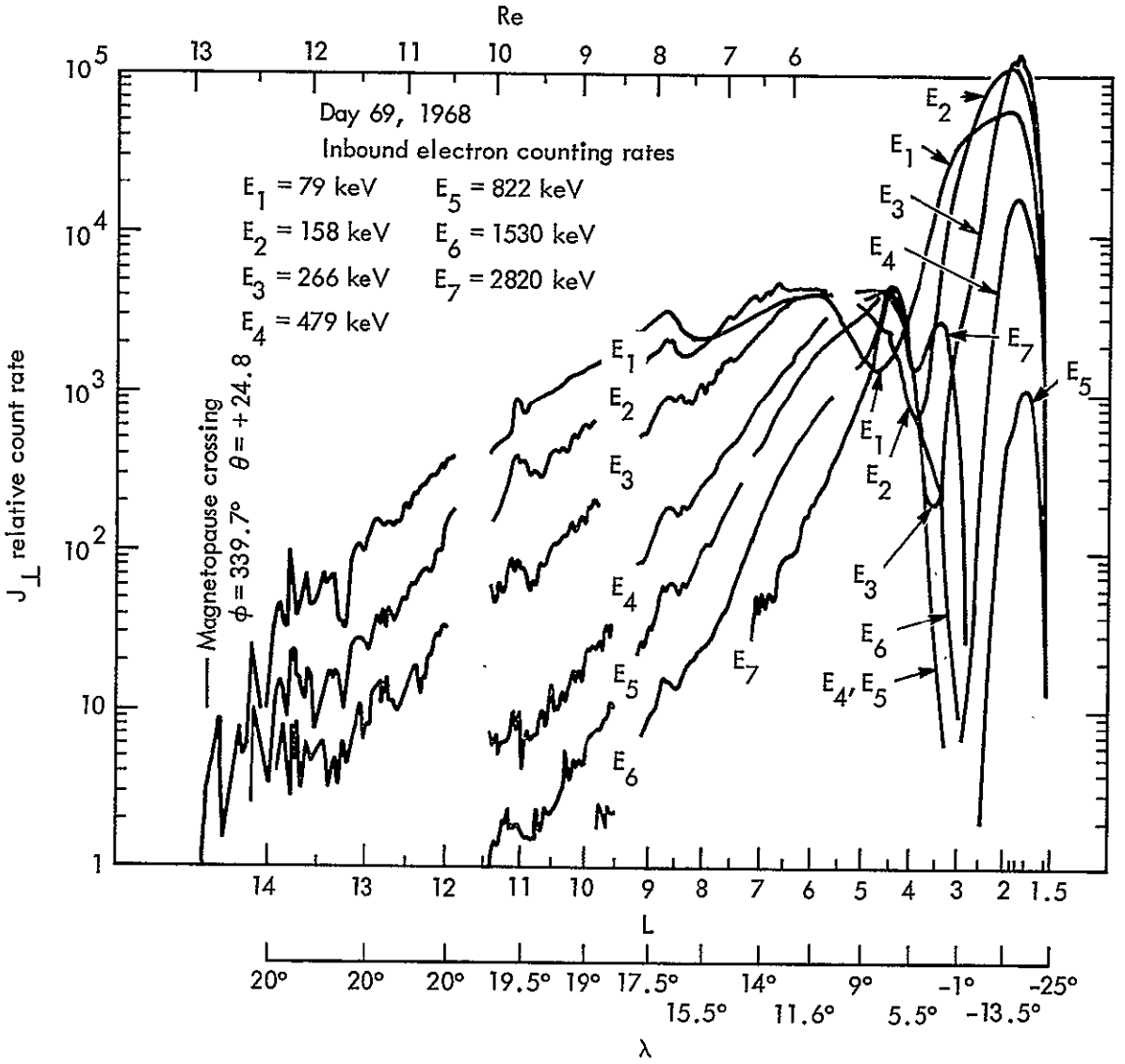

Note: To connect relative count rate to counts/sec, multiply by 1.00, 0.43, 0.33, 0.43, 1.67, 0.91, and 0.40 for E_1, E_2, E_3, E_4, E_5, E_6, and E_7, respectively.

Fig. 9-2. Example of electron counting rates inbound near the earth-sun line on March 9, 1968.

(see Figs. 9-4 and 9-5) and, in addition, has provided extensive data (P_1 and P_2) in the magnetosheath. Excellent observation of solar flare particles, protons, and alpha-particles have been made.

In the radiation belts, greater sensitivity could not be used although in the far earth regions >7 earth radii this would be welcome. In the region of peak fluxes of protons of a few MeV (at ~2 to 3 earth radii), the flux incident on the front detector of the telescope has been in excess of 10^5/sec. This has caused severe dead-time losses which are doubly complicated due to interactions between channels and spectral dependance. In the heart of the

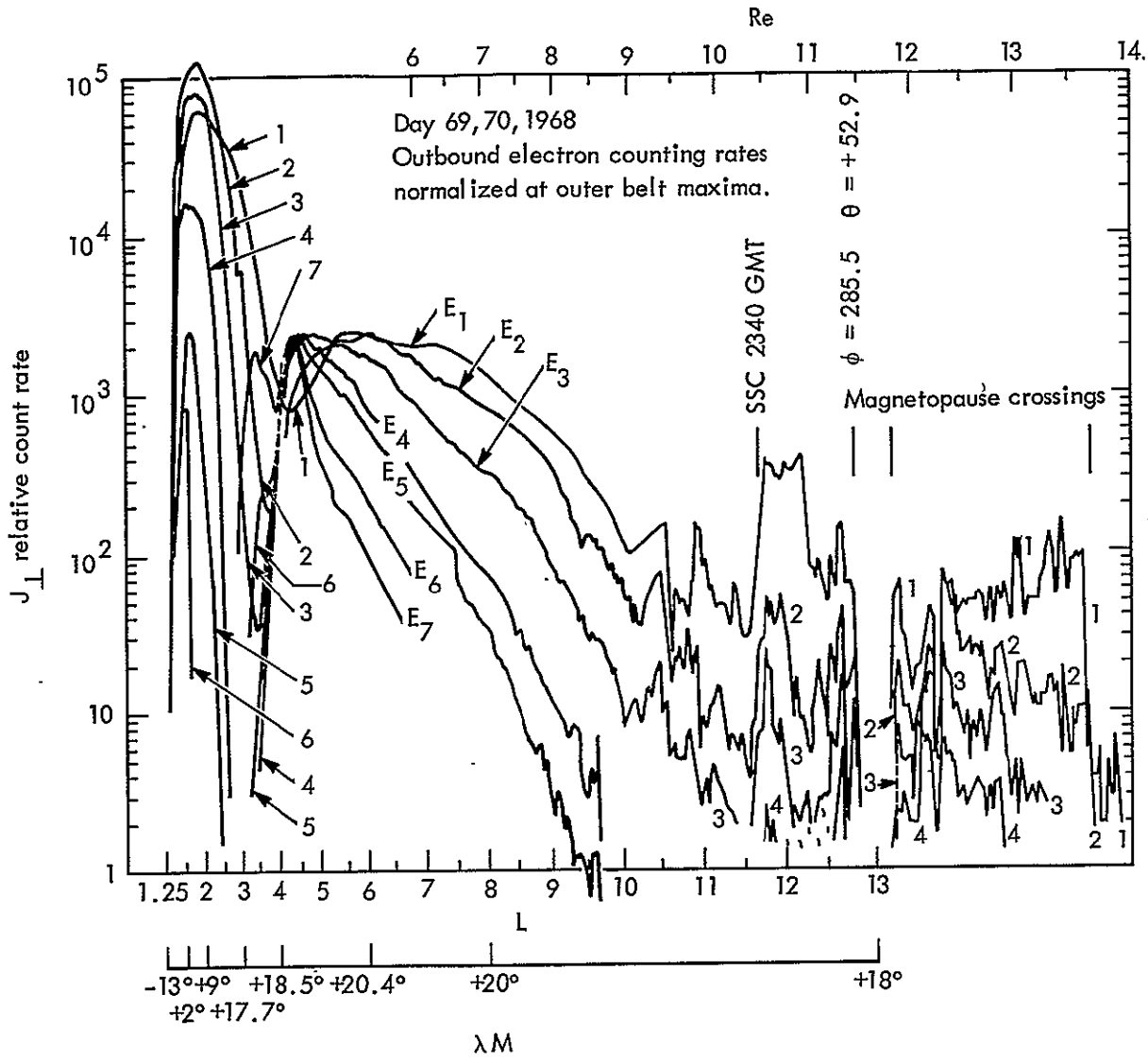

Note: To connect relative count rate to counts/sec, multiply by 1.00, 0.56, 0.52, 0.64, 2.60, 1.28, and 0.48 for E_1, E_2, E_3, E_4, E_5, E_6, and E_7, respectively.

Fig. 9-3. Example of electron counting rates outbound towards the dawn side of the earth on March 9 and 10, 1968.

inner belt (~1.4 earth radii), penetrating protons have caused a background problem. Proton data in this small region are expected to be of limited value. Outside the inner belt, however, background rejection has been extremely good. Proton/background ratios of >100/1 are normal, occasionally reaching 10,000/1. Rejection of electrons has been extremely good.

Channels α_1, α_2, α_3, α_{B_1}, α_{B_2}, α_{B_3}, and E_8 have all provided data. For other than α_1 it is not clear, however, that useful data have been provided. Careful analysis will be required to make use of these data. Alpha channel α_1 appears to have provided useful data. There is, however, the problem of proton pulse-pile-up, since the effective electronic pulse width is of

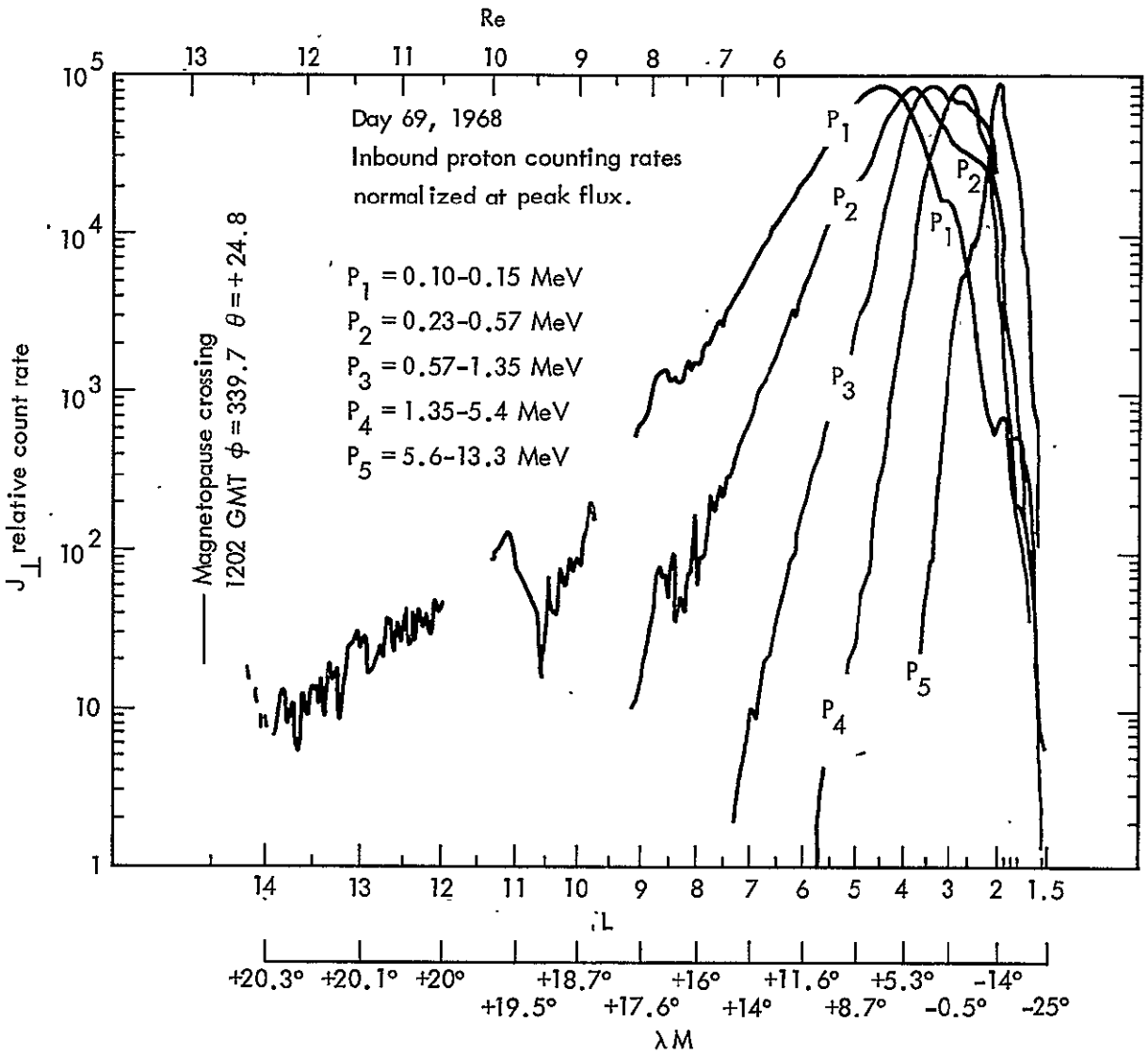

Note: To connect relative counts to counts/sec, multiply by 0.22, 1.00, 0.54, 1.18, and 0.48 for P_1, P_2, P_3, P_4, and P_5, respectively.

Fig. 9-4. Typical proton counting rates inbound near the earth's sun line on March 9, 1968.

the order of 1 μsec. By careful analysis (including spatial dependance) of the inflight proton spectra, we should be able to internally measure the pile-up parameters and hence, provide the necessary corrections for the α_1 data.

By far the most important data have come from channels P_1 through P_4 (0.1 to 5.4 MeV) with the weight towards the lowest channels. A major regret is that we did not provide means for six channel pulse-height analysis on the pulses from detector

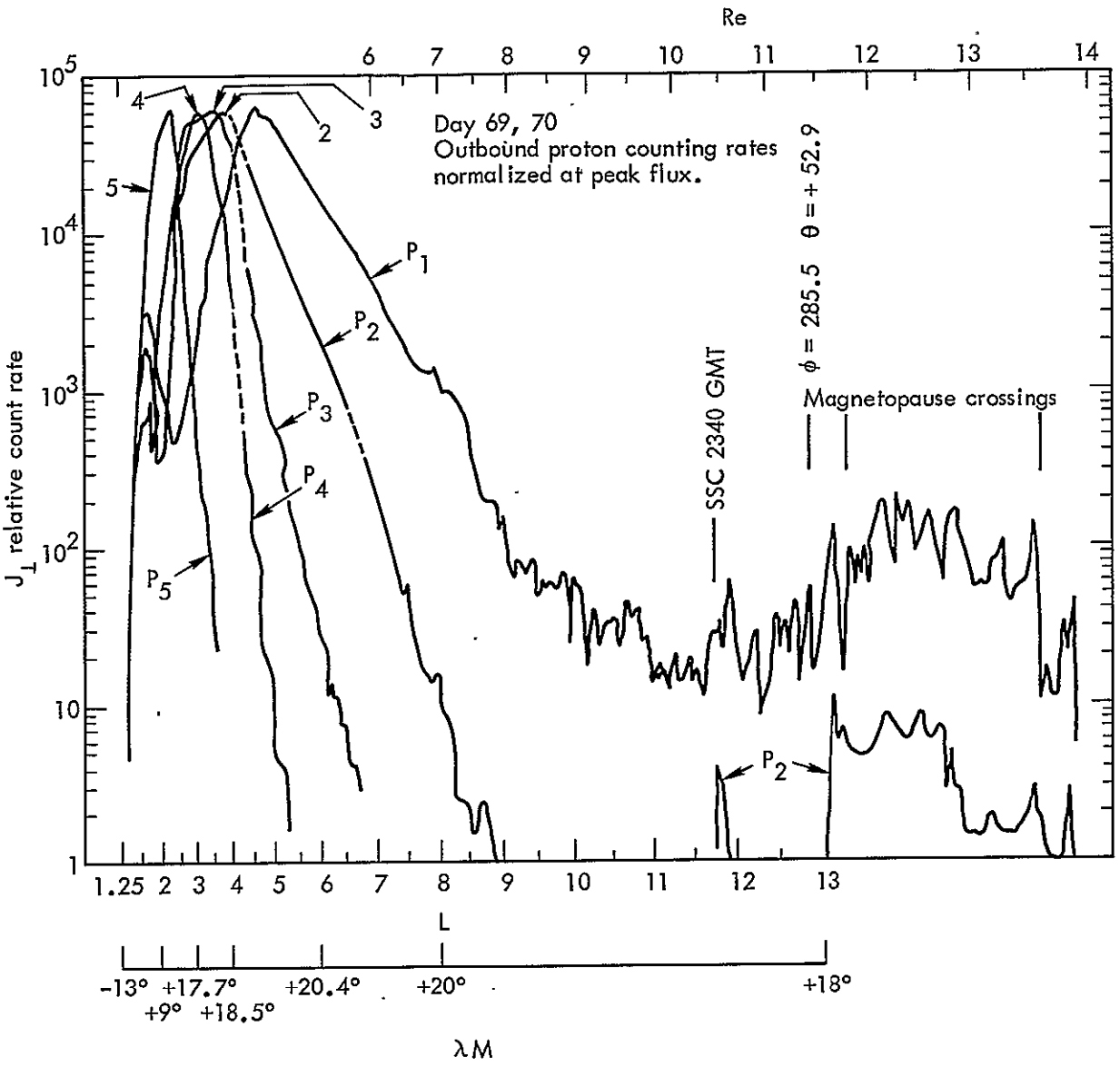

Note: To connect relative count to counts/sec, multiply by 0.178, 1.00, 0.69, 0.64, 0.37, for P_1, P_2, P_3, P_4 and P_5, respectively.

Fig. 9-5. Typical proton counting rates on March 9 and 10, 1968, towards the dawn side of the earth.

D_1, and provide means by ground command to read these data out through the telemetry channels provided for P_2 through P_7. This would have greatly enhanced operations beyond about 4 Re.

9.3 STATUS INDICATORS

The status indicators show that the experiment has functioned normally. The OPEP temperature has been in the range of -10 to +10°C. Temperatures early in the mission were about 0°C. For a month or so they were near -10°C. Recently, the experiment has warmed and is staying near +5°C. The main body package has stayed at 22 ± 3°C for the entire mission. The voltage monitors have shown no indication of change. The fields of the spectrometer magnets are monitored by Hall probes HE-1 and HE-2. The fields have followed the normal temperature dependence measured before flight. Detector leakage current monitors show that the detectors have been well behaved.

9.4 INFLIGHT PULSE GENERATOR

The operating plan requires exercising the pulse generator several times at each apogee. Apogee is chosen simply because the electron and proton counting rates are usually insignificant there, and will not affect the pulse generator results. The pulse generator shows that the discriminator tripping levels are stable, that the preamplifiers are following the normal temperature dependence, and that the digital system is working correctly. The pulse generator has been invaluable in checking the system during flight.

10. Acknowledgments

A number of people have made important contributions to the success of the experiment. At the Lawrence Radiation Laboratory, Livermore, K. Pettipiece and A. MacGregor worked on the proton detection system; J. Weaver, Mary Glover, William March, W. Owings, H. Curry, and H. Dalbol did the electronic fabrication and testing; D. Parmenter, J. Bonner, M. Fernandez, L. Gross and E. Frohwein did mechanical design and fabrication; and R. Thomas and R. Friesen made major contributions in the design of the digital system. Dr. J.R. Walton developed the computer programs for the material presented in Section 9.

We acknowledge the efforts of R. Lothrop of the Lawrence Radiation Laboratory, Berkeley for constructing detectors for the proton telescope. Dr. F. Ziemba, of Solid State Radiations Inc., made a special effort to provide excellent detectors for the electron detection system.

We gratefully acknowledge the efforts of the crew at Thompson Ramo Woolridge under Dr. J. Lindner, K. Bradford and W. Kesler, who integrated the experiment into the spacecraft. We single out the engineer who was responsible for the experiment at TRW, D. Schultz.

At the Goddard Space Flight Center special thanks go to Dr. E. Mercanti, (OGO-Coordinator) and his assistants. We thank J. Krehbiel for seeing the experiment through testing at Goddard; R. Browning, H. Burdick and associates for providing an excellent scanning mechanism for OPEP-2, and; J. Meenen, Operations, and H. Linder, Data Processing, for their efforts during post launch.

Distribution

LRL Internal Distribution

Michael M. May
W. Hill 10
J. Wujek
J. Mc Quaid
N. Jensen
R. Bogdanowicz
F. Seward
J. Carothers
A. Stripeika
C. Curry
H. Brooks
R. Paige
C. Hirch, EEIC
E. Hulse
J. R. Walton
R. Buck
H. Reynolds
H. West 35

G. D. Dorough
W. E. Nervik
TID File 30

External Distribution

E. Mercanti
Office of Director
Office of Assistant Director, Projects 3
Office of Assistant Director, T&DS 3
Office of Assistant Director, SS 3
Office of Technical Services 3
Library 2
Negotiator
Technical Information Division
National Space Science Data Center 5
Technical Director 7
Goddard Space Flight Center
Greenbelt, Maryland

R. G. D'Arcy 25
The Bartol Research Foundation of the Franklin Institute
Swarthmore, Pennsylvania

Division of Technical Information Extension, Oak Ridge 2

RAC/md/lc